

Effects of Anodizing and Post  
Sealing on Corrosion Characteristics  
of Magnesium Alloys

# **Effects of Anodizing and Post Sealing on Corrosion Characteristics of Magnesium Alloys**

Supervisor: Professor Masazumi Okido

by

Yun-Il Choi

Department of Materials Science and Engineering

Nagoya University

A dissertation submitted to the faculty of the Nagoya University in partial fulfillment of the requirements for the degree of Doctor of Philosophy in the Department of Materials Science and Engineering.

Nagoya, Japan

2014. 3. 25

Approved by

---

Professor Masazumi Okido

*To my beloved parents  
& my little darling, Ji-Hye Lim*

## Abstract

The effect of electrolyte temperature on the corrosion characteristics of wrought AZ31B, AZ61, and as-cast AZ91 Mg alloys in 0.1 M NaCl aqueous solution was analyzed. Systematic studies indicate that AZ91 exhibits higher corrosion resistance than AZ61 at nearly room temperatures. However, at high temperatures of around 55 °C, we observed contradictory corrosion behavior, as demonstrated by potentiodynamic tests, electrochemical impedance spectroscopy, potentiostatic tests, and cyclic corrosion tests. Of the three different Mg alloys considered in this study, AZ61 shows the highest corrosion potential, lowest corrosion current density, highest polarization resistance, and slowest pitting propagation kinetics at 55 °C. These results can be attributed to the microstructure of AZ61 which contains nano-scale  $\beta$ -phase particles effectively dispersed within the grains. On the other hand, AZ91 had many grains that did not contain any  $\beta$ -phases, and hence observed lower corrosion behavior than AZ61 at 55 °C. Of them, AZ31B suffered the severest increase in corrosion kinetics with high uniform corrosion as the electrolyte temperature increased.

In order to improve the corrosion resistance of AZ31B Mg alloy, the surface was anodized with a pulse potential between the anodic oxidation (10 V<sub>Ag/AgCl</sub>) and active regions (−1.35 V<sub>Ag/AgCl</sub>) in 2 M NaOH aqueous solution at 30 °C. Optimal conditions for the pulse anodizing were a duty ratio of 91%, a frequency of 0.09 Hz, and an anodizing time of 600 s. Pulse anodizing caused a remarkable decrease in the surface porosity (11-fold) and an increase in the film thickness (1.6-fold) from those obtained under a constant potential of 10 V<sub>Ag/AgCl</sub>. Furthermore, an Al-enriched crystalline oxide layer was formed on the outer surface of MgO, which improves the corrosion resistance of the Mg alloy in neutral solutions. In consequence, the pitting potential for the specimen pulse anodized increased to −1.36

$V_{\text{Ag/AgCl}}$  from 10 V of DC anodizing and the corrosion current density decreased to  $60 \pm 10 \mu\text{A cm}^{-2}$ , resulting in an approximately 3-fold decrease in the corroded area after anodic breakdown and salt spray tests.

For surface sealing, and therefore, achieving further enhancement in the corrosion resistance of as-anodized AZ31B Mg alloy, stannate post-treatment of as-anodized AZ31B Mg alloy was carried out in 0.4 M sodium stannate 3-hydrate ( $\text{Na}_2\text{SnO}_3 \cdot 3\text{H}_2\text{O}$ ) at 77 °C. It effectively leveled the porous anodized coating by depositing a  $\text{SnO}_2$  superficial layer with a thickness of 0.4  $\mu\text{m}$ . After the surface sealing, the mass transport impedance at low frequency was controlled by the ideal capacitance dispersion during the initial immersion; thus, slow corrosion kinetics was achieved. This impedance behavior might account for the ideally polarizable cathodic behavior of the electrode with overpotential. As a consequence, the stannate post-treatment afforded higher polarization resistance, corrosion potential, and pitting potential values throughout the immersion in 0.1 M NaCl.

# Table of Contents

Abstract .....	i
Table of Contents .....	iii
List of Tables .....	vii
List of Figures .....	vii
Symbols and Abbreviations .....	xv
<b>I. Introduction .....</b>	<b>1</b>
<b>II. Literature Survey, Research Background and objectives</b>	
2-1. Literature Survey .....	9
2.1.1. Metallurgy of Magnesium .....	9
2.1.1-1. Alloying Elements .....	9
2.1.1-2. Impurity Elements .....	12
2.1.2. Corrosion of Magnesium .....	13
2.1.3. Anodizing of Magnesium .....	21
2.1.3-1. General Remark .....	21
2.1.3-2. Pulse Anodizing .....	25
2.1.3-3. Thermodynamic Stability of Magnesium Compounds .....	27
2.1.3-4. Anodizing Behavior .....	30
2.1.3-5. Oxygen Evolution during Anodizing .....	34
2.1.4. Structure of Anodic Film .....	35
2.1.5. Corrosion Behavior of Anodic Film .....	39

2.1.5-1. Effect of Substrate .....	39
2.1.5-2. Effect of Porosity .....	40
2.1.6. Dyeing and Impregnation .....	41
2.1.7. Surface Sealing .....	43
2-2. Research Background and objectives .....	46

### **III. Temperature dependence of passivity breakdown on Mg-Al alloys in NaCl solution**

3-1. Introduction .....	56
3-2. Experimental .....	59
3-3. Results and Discussion .....	63
3.3-1. Effect on polarization behavior .....	63
3.3-2. Effect on electrochemical impedance behavior .....	67
3.3-3. Effect on current transient behavior .....	73
3-4. Conclusions .....	81

### **IV. Improvement in Corrosion Characteristics of AZ31 Magnesium Alloy by Square Pulse Anodizing between Anodic Oxidation and Active Regions**

4-1. Introduction .....	85
4-2. Experimental .....	87
4-3. Results and Discussion .....	89
4.3-1. Anodic polarization behavior of AZ31 Magnesium alloy .....	89
4.3-2. Changes in current transient behavior of AZ31 Magnesium alloy during pulse anodizing .....	91
4.3-3. Effect of pulse parameters on the anodic polarization behavior of AZ31 Magnesium alloy .....	94

4.3-4. Effects of pulse anodizing on the EIS response of AZ31 Magnesium alloy	97
4-4. Conclusions	104

**V. Surface Porosity Tuning and Simultaneous Formation of Al-enriched Oxide Layer by Pulse-Anodizing AZ31 Magnesium Alloy**

5-1. Introduction	108
5-2. Experimental	110
5-3. Results and Discussion	112
5.3-1. Effects of pulse anodizing on the surface porosity of the anodic film	112
5.3-2. Simultaneous formation of the Al enriched oxide layer along with MgO	119
5.3-3. Effect of pulse anodization on the corrosion characteristics of the anodic film	121
5-4. Conclusions	126

**VI. Synergistic Corrosion Protection for AZ31 Magnesium alloy by Anodizing and Stannate Post-sealing Treatments**

6-1. Introduction	130
6-2. Experimental	133
6-3. Results and Discussion	136
6.3-1. Effect on surface and cross-sectional structures of as-anodized coating	136
6.3-2. Effect on electrochemical characteristics of anodized coating	142
6-4. Conclusions	152

**VII. Summary and Future Work**

7-1. Summary	158
--------------	-----



7-2. Future Work .....	159
<b>VIII. Acknowledgements</b> .....	<b>161</b>

# List of Tables

Table 2.1. Typical corrosion potential, $E_{\text{corr}}$ , values of Mg and its secondary phases after 2 hrs of immersion in deaerated 5 wt.% NaCl solution saturated with $\text{Mg}(\text{OH})_2$ (pH 10.5). .....	15
Table 2.2. Corrosion resistance of some anodic films during salt spray tests. ....	44
Table 3.1. Chemical compositions (wt.%) of the different Mg alloys, namely, AZ31B, AZ61, and AZ91. ....	59
Table 3.2. Details of the condition adopted during the cyclic corrosion test (T = operating temperature, RH = relative humidity). During salt-spray step, the high concentration of salt (5 wt.%) was used in order to ensure comparability within 24 hrs of the tests. .....	61
Table. 4.1. Chemical composition (wt.%) of AZ31 Mg alloy used in this study. ....	87
Table 5.1. Details of cyclic corrosion test (CCT). T and RH represent the operating temperature and relative humidity, respectively. ....	111
Table 6.1. Details of cyclic corrosion test (CCT). T and RH represent operating temperature and relative humidity, respectively. ....	134

# List of Figures

Fig. 2.1. Effect of Al concentration on the corrosion rate of die-cast magnesium alloys in 5 wt% NaCl solution. ....	11
Fig. 2.2. Effect of various alloying elements on the corrosion rate of magnesium alloys. ....	13
Fig. 2.3. Effect of Ni, Fe, and Cu impurities on the corrosion rate of die-cast AZ91 magnesium alloys during salt spray tests. ....	14
Fig. 2.4. Microstructure of AZ91 alloy (cast into a steel mould). ....	16
Fig. 2.5. Schematic representation for the corrosion protection effect of $\beta$ -phase. (a) $\beta$ -phase is nearly continuous; (b) the corrosion propagation through $\alpha$ -Mg is effectively retarded by the $\beta$ -phase. Corrosion products are not illustrated here. ....	17
Fig. 2.6. Electrochemical reactions occurring on the magnesium during corrosion in neutral water. ....	18
Fig. 2.7. Dimensional effect of anodizing, painting, and plating. ....	21
Fig. 2.8. Objectives of magnesium surface treatments. ....	22
Fig. 2.9. Typical anodizing cells: (a) Batch anodizing, (b) Continuous anodizing. ....	23
Fig. 2.10. Schematic diagram of various wave forms of pulse anodizing; (a) periodic reverse; (b) square; (c) asymmetric sine. ....	25
Fig. 2.11. Schematic diagram of capacitance effect by pulse. ....	26
Fig. 2.12. Pourbaix diagram of pure magnesium. ....	28
Fig. 2.13. Changes in voltage and current responses during anodizing at constant current and constant voltage, respectively. ....	31
Fig. 2.14. Schematic diagram for the voltage dependence of oxide formation on the Magnesium. ....	32

Fig. 2.15. Oxygen evolution and current efficiency during anodization under constant electric charge ( $18 \text{ C cm}^{-2}$ ). The negative efficiency could be attributed to the thermal decomposition of water during anodizing. For more detail discussion, please refer to the [ref. 80](#). ..... 34

Fig. 2.16. Schematic diagram for the formation of porous anodic film on the magnesium surface. .... 35

Fig. 2.17. TEM cross section of the anodic film formed on pure magnesium during Dow 17 process. Arrow shows the barrier layer connected to the metal substrate under the cylindrical layer. .... 36

Fig. 2.18. Schematic diagram of a typical cross section found for the hard ceramic oxide coatings. .... 37

Fig. 2.19. Schematic diagrams of (a) non-through-pores and through-pores formed in an anodic film on magnesium and (b) the simplified microstructure of the anodic film. .... 40

Fig. 2.20. Schematic diagram of an anodic film after dyeing treatment. .... 42

Fig. 2.21. Schematic diagram of an anodic film with dye after impregnation treatment in boiling water. .... 42

Fig. 3.1. Photograph and schematic of the electrochemical cell, employing two identical working electrodes, used for corrosion monitoring during cyclic corrosion tests. The WE1 and WE2 connect the working electrode and counter electrode of potentiostat, respectively. .... 60

Fig. 3.2. Variation in (a) corrosion potential  $E_{\text{corr}}$  and potential at  $1 \text{ mA cm}^{-2}$ , and (b) corrosion current density  $i_{\text{corr}}$  of AZ31B, AZ61, and AZ91 as functions of electrolyte temperature in 0.1 M NaCl, as estimated from potentiodynamic tests. The  $i_{\text{corr}}$  was estimated by the extrapolation of cathodic Tafel slopes back to the  $E_{\text{corr}}$ . The intersection corresponds to the  $i_{\text{corr}}$ . Error bars represent standard deviations. Smaller

deviation than the symbols show no error bar. ....	64
Fig. 3.3. Anodic and cathodic polarization behaviors of electrodes AZ31B, AZ61, and AZ91 with electrolyte temperature in 0.1 M NaCl. ....	65
Fig. 3.4. Nyquist plots of AZ31B, AZ61, and AZ91 measured at applied potential of $-1.38 V_{Ag/AgCl}$ as a function of electrolyte temperature, immediately after immersion in 0.1 M NaCl. The experimental impedance data (●) are Kramers-Kronig relation compliant (—), indicating that these processes fulfill causality, linearity, stability, and finiteness. For detailed explanation for the Kramers-Kronig relation, refer to the <a href="#">ref. 32</a> . ....	68
Fig. 3.5. Nyquist plots of AZ31B, AZ61, and AZ91 measured at open-circuit potential as a function of electrolyte temperature, after immersion for 30 min in 0.1 M NaCl. The experimental impedance data (●) are Kramers-Kronig relation compliant (—), indicating that these processes fulfill causality, linearity, stability, and finiteness. For detailed explanation for the Kramers-Kronig relation, refer to the <a href="#">ref. 32</a> . ....	69
Fig. 3.6. Variation of polarization resistance $R_p$ , i.e. sum of all resistance, at (a) $-1.38 V_{Ag/AgCl}$ , (b) open-circuit potential as a function of electrolyte temperature $T$ , estimated from <a href="#">Fig. 3.3</a> and <a href="#">Fig. 3.4</a> , respectively. The typical equivalent circuit models consisting of $m$ series connected Voigt elements ( $-R-(RC)_m-$ ) without inductance element were used for curve fitting. ....	71
Fig. 3.7. Corrosion current transients $i$ as a function of electrolyte temperature through the alloys AZ31B, AZ61, and AZ91 at $-1.38 V_{Ag/AgCl}$ in 0.1 M NaCl. ....	74
Fig. 3.8. Corrosion current transients of AZ31B, AZ61, and AZ91 during cyclic corrosion test. Details of the spray-dry-wet steps are described in <a href="#">Table. 2</a> . ....	76
Fig. 3.9. SEM images of the alloys (a, b) AZ61 and (c, d) AZ91 (only polished and etched). ....	78

Fig. 4.1. Waveform for applied square pulse potential. ....	88
Fig. 4.2. Anodic polarization behavior of AZ31 Mg alloy in 2 M NaOH solution at 303 K with a scan rate of 1 mV s <sup>-1</sup> . ....	90
Fig. 4.3. Approximate data plots of the anodizing behavior for AZ31 Mg alloy over 1000 s as a function of duty ratio in 2 M NaOH at 303 K. These current are values extracted from point A (see Fig. 4) during the whole anodizing process. ....	92
Fig. 4.4. Further detailed waveform view of square pulse potential and its current density response ( $t_t$ : Duration for applying anodic oxidation potential, $t_a$ : Duration for applying anodic potential). ....	93
Fig. 4.5. Changes in anodic polarization behavior of anodized AZ31 Mg alloy as a function of duty ratio $\alpha$ in deaerated 0.1 M NaCl at 303 K. Anodizing time: (a) 300 s, (b) 600 s, and (c) 900 s. ....	95
Fig. 4.6. Variation in (a) $E_{\text{pit}}$ and (b) $i_{\text{corr}}$ as a function of duty ratio $\alpha$ . ....	96
Fig. 4.7. Electrical equivalent circuit model used in this study. ....	98
Fig. 4.8. Measured Nyquist plots of anodized AZ31 Mg alloys immediately after immersion in deaerated 0.1 M NaCl at 303 K: anodized for (a) 300 s (b) 600 s, (c) 900 s. ....	98
Fig. 4.9. Variation in (a) polarization resistance $R_p$ and (b) double layer capacitance $C_{\text{dl}}$ of anodized AZ31 Mg alloy as a function of duty ratio $\alpha$ in deaerated 0.1 M NaCl at 303 K estimated by fitting the measured impedance spectra. ....	99
Fig. 4.10. The close interrelationship between the results of the anodic polarization test ( $E_{\text{pit}}$ and $i_{\text{corr}}$ ) and the EIS test ( $R_p$ ). ....	100
Fig. 4.11. Change in surface morphology of the anodic films formed in 2 M NaOH for 600 s with duty ratios (a) $\alpha = 83$ , (b) $\alpha = 91$ , (c) $\alpha = 98$ , and (d) $\alpha = 100$ (constant potential). The corresponding thickness of anodic film was about 0.6–1.0 $\mu\text{m}$ . ....	101

Fig. 4.12. Variation in pore size ( $\mu\text{m}$ ) and surface porosity (%) of the anodic films as a function of duty ratio $\alpha$ . .....	102
Fig. 4.13. Typical X-ray diffraction pattern of the anodic films (MgO) formed on AZ31 Mg alloy with the different duty ratios $\alpha$ for 600 s. ....	103
Fig. 5.1. Changes in surface morphologies of the anodic films formed in 2 M NaOH after 600 s of anodization with different conditions: (a) constant potential at 10 $V_{\text{Ag}/\text{AgCl}}$ and (b-d) pulse potential between 10 and -1.35 $V_{\text{Ag}/\text{AgCl}}$ under constant duty ratio $\alpha$ of 91% ( $f = 0.04, 0.09, \text{ and } 0.18$ Hz, respectively). Specimen anodized at an $f$ of 0.06 Hz had a similar surface morphology with that formed at 0.04 Hz. ....	113
Fig. 5.2. Variation in maximum diameter ( $\mu\text{m}$ ) and average density (%) of the pores formed on the anodic films as a function of pulse repetition frequency $f$ . ....	114
Fig. 5.3. Changes in Auger intensity of elements in the anodic films due to the pulse anodization: (a) constant potential (10 $V_{\text{Ag}/\text{AgCl}}$ ) applied for 10 min and (b) pulse potential applied between 10 and -1.35 $V_{\text{Ag}/\text{AgCl}}$ ( $\alpha = 91\%, f = 0.09$ Hz) for 10 min. ....	116
Fig. 5.4. (a) Cross-sectional morphology and (b) X-ray maps of part 'A' for the anodic film formed under constant potential (10 $V_{\text{Ag}/\text{AgCl}}$ ) applied for 10 min; and (c) cross-sectional morphology, (d) X-ray maps of part 'B', and (e) line-scan profile of part 'C-D' for the anodic film formed under pulse potential between 10 and -1.35 $V_{\text{Ag}/\text{AgCl}}$ ( $\alpha = 91\%, f = 0.09$ Hz) for 10 min. ....	120
Fig. 5.5. Potentiodynamic polarization curves of the anodic films as a function of pulse repetition frequency $f$ in 0.1 M NaCl at 303 K. Anodizing time: 600 s. ....	122
Fig. 5.6. Changes in (a) current density responses, (b) average density and total number of breakdown spots, and (c) surface appearances of the anodic films as a function of the pulse repetition frequency $f$ during/after the anodic breakdown tests (carried out at -	

1.4 V vs. Ag/AgCl for 420 s in 0.1 M NaCl). .....	123
Fig. 5.7. Surface appearances of the anodic films after cyclic corrosion tests carried out for 24 h in a 5 wt% NaCl environment. ....	124
Fig. 6.1. Changes in surface morphology of the as-anodized coating after stannate post-treatment: (a) as-anodized (at 10 V <sub>Ag/AgCl</sub> for 10 min), (b) stannate post-treated for 10 min. The white dots, whether stannate post-treated or not, represent protrusions on the surface of the coating. Pore depth of the as-anodized coating was measured to be approximately 0.3–0.5 μm. ....	136
Fig. 6.2. Changes in pH of the stannate post-treatment solution with temperature. ....	138
Fig. 6.3. High-resolution Sn 3d <sub>5/2</sub> XPS spectrum (circles) and decomposed components (solid line) of the stannate post-treated coating. ....	139
Fig. 6.4. (a) Cross-sectional morphology (i, SnO <sub>2</sub> layer; ii, anodized coating; and iii, AZ31 substrate), (b) Changes in Sn/O ratio with depth, and (c) EDS elemental mapping of the coupon stannate post-treated for 10 min. ....	141
Fig. 6.5. Measured Nyquist plots of (a) the as-anodized coating and (b) the coating after stannate post-treatment for 10 min for different immersion times in 0.1 M NaCl solution at 298 K. ....	143
Fig. 6.6. Schematic of the solution/coating/substrate cell system. ....	145
Fig. 6.7. Changes in polarization resistance $R_p$ (i.e. the sum of all resistances) of the as-anodized and stannate post-treated (10 min) coatings with the immersion time in 0.1 M NaCl solution at 298 K. ....	146
Fig. 6.8. Change (a) in anodic and cathodic polarization behaviors of the as-anodized coating with the stannate post-treatment time and (b) in $E_{OCP}$ with the immersion time in 0.1 M NaCl solution at 298 K. There was no repeatability to the behaviors marked by red arrows. ....	147



Fig. 6.9. Change in pitting potential  $E_{\text{pit}}$  and corrosion potential  $E_{\text{corr}}$  with the stannate post-treatment time on the (a) as-anodized coating (at 10 V<sub>Ag/AgCl</sub> for 10 min) and (b) polished surface (0.05- $\mu\text{m}$  Al<sub>2</sub>O<sub>3</sub> powder). Optical microscopy images of the specimens (1  $\times$  1 cm) after cyclic corrosion tests for 24 h are included. .... 149

## Symbols and Abbreviations

AZ-type magnesium alloy	Magnesium alloys with the primary alloying elements of aluminum and zinc
AZ31	Mg-3Al-1Zn (wt.%)
AZ61	Mg-6Al-1Zn (wt.%)
AZ91	Mg-9Al-1Zn (wt.%)
$R_{PB}$	Pilling-Bedworth ratio
$\alpha$ -phase	Mg solid solution ( $\alpha$ -Mg)
$\beta$ -phase	Mg <sub>17</sub> Al <sub>12</sub> intermetallic compound
$E_t$	Anodic oxidation potential
$E_a$	Active potential
$t_t$	Duration of applying $E_t$
$t_a$	Duration of applying $E_a$
$\alpha$	Duty ratio ( $= t_t / (t_t + t_a) \times 100$ )
$f$	Frequency
$E_{corr}$	Corrosion potential
$E_{pit}$	Pitting potential
$E_{OCP}$	Open circuit potential
$i_{corr}$	Corrosion current density
DOP	Degree of polarization
WE	Working electrode
CE	Counter electrode
RE	Reference electrode

EIS	Electrochemical impedance spectroscopy
$R_p$	Polarization resistance
$C_{dl}$	Double layer capacitance
$R_s$	Solution resistance
$W_{max}$	The frequency at which the imaginary component reaches a maximum
CPE	Constant phase element
$W$	Warburg impedance
$Z_{Re}$ (or $Z'$ )	Real part of impedance
$Z_{Imag}$ (or $Z''$ )	Imaginary part of impedance
$J_p$	Ionic flux
$J_n$	Electronic flux
$D$	Pseudo diffusion coefficient
$c$	Concentration of corrosive species at $x$
$\Gamma$	Concentration of corrosive species adjacent to the metal substrate
CCT	Cyclic corrosion test
RH	Relative humidity
T	Temperature
$E_{app}$	Applied potential
$E_c$	Critical breakdown potential
$t_i$	Incubation time
$\tau$	Transient time
$i_{max}$	Maximum current density
ZRA	Zero resistance ammeter

SEM	Scanning electron microscopy
EDS	Energy dispersive X-ray spectroscopy
TEM	Transmission electron microscopy
AES	Auger electron spectroscopy
XPS	X-ray photoelectron spectroscopy
BE	Binding energy

# 1. Introduction

Mg and its alloys are front runners in addressing strong current need for lightweight materials in industries such as automobiles, aerospace, and electronics because of their favorable characteristics: low density, high specific strength-to-weight ratio, electromagnetic interference shielding properties, good formability, and recyclability [1,2]. Especially, major automobile makers have been hastening their plans to use wrought magnesium (Mg) alloys in vehicles [3]. Reducing the weight of automobiles is one implementable strategy for effectively coping with global warming, and its main purpose is to improve vehicle performance and fuel efficiency. A 100 kg reduction in the weight of an automobile can decrease its CO<sub>2</sub> emissions by 8–12 g km<sup>-1</sup>. Moreover, this strategy is useful for improving the cruising distances of electric vehicles.

Despite of these competitive advantages over rival conventional materials, the applications are still restricted due to their extremely negative equilibrium potential and high corrosion susceptibility in chloride-containing environment. Moreover, effective protection against galvanic and general corrosion is difficult to achieve only by continuing alloy development [4].

Mg is a highly reactive (active) element in that it tends to readily lose its two valence electrons and further react with chloride ions (Cl<sup>-</sup>) to obtain stable configurations. Chloride ion intrusion and moisture absorption induce a breakdown of the naturally formed Mg oxide/hydroxide and, eventually, an exposed  $\alpha$ -phase will undergo degradation to form hydromagnesite (Mg<sub>5</sub>(CO<sub>3</sub>)<sub>4</sub>(OH)<sub>2</sub>·4H<sub>2</sub>O) and nesquehonite (MgCO<sub>3</sub>·3H<sub>2</sub>O) [5–7]. Moreover, the Mg dissolves readily in dilute acids to form aquated Mg ions (Mg<sup>2+</sup>) along with H<sub>2</sub> gas. In

this context, many different types of anodizing processes have been developed to produce Mg alloys with anti-corrosion abilities and mitigate the various types of corrosion damage.

Anodization is an electrolytic passivation process that produces a thick, chemically stable protective oxide film on valve metals. Anodization mitigates the general and galvanic corrosion of bare Mg alloys, but the formed anodic films are more water soluble than those formed on Al alloys, which are rival traditional materials for weight reduction. Therefore, anodization is often used to produce an undercoating layer to provide better adhesion for various organic finishes [8,9]. Furthermore, a recent important development in this process has been the use of alkaline solutions with various additives such as  $\text{Na}_3\text{PO}_4$  [10],  $\text{KMnO}_4$  [11],  $\text{Na}_2\text{B}_4\text{O}_7$  [12–14],  $\text{NaAlO}_2$  [15,16] and  $\text{Na}_2\text{SiO}_3$  [10,12,14,15] as electrolytes with lower environmental impact than those containing fluoride ( $\text{F}^-$ ) and chromate ( $\text{CrO}_4^{2-}$ ).

As another development in this process, several studies have explored the idea of using a pulse current or potential (pulse anodizing) instead of a constant value to get a higher mean current density and thereby decrease the processing time [17]. Qian et al. [18] applied a square pulse current of 0–40  $\text{mA cm}^2$  for 10–30 min on AZ91D Mg alloy in a NaOH solution containing meta-silicates, borates and other additives. However, a porous oxide layer still formed and the micro-pores actually seemed to widen with increasing anodizing time. Duan et al. [19] obtained plasma electrolytic oxidation (PEO) films on AZ91D Mg alloy by applying a square pulse potential of 350–400 V for 1–2 h in a KOH solution containing various additives. Though they found that fluoride- and phosphate-containing electrolytes were the most effective in improving the corrosion resistance of AZ91D Mg alloy, micro-pores still remained in the anodic films. Liu et al. [20] obtained a protective passive film on pure Mg by applying pulse potential between passive ( $-0.5 \text{ V}_{\text{SCE}}$ ) and passive/active regions ( $-1.36 \text{ V}_{\text{SCE}}$ ) for 30 min in 0.25 M  $\text{Na}_2\text{SO}_4$  + 0.1 M NaOH solution. To our knowledge, no

other reports on square pulse anodizing exist, especially on conventional anodizing of Mg alloys.

In general, the anodic films formed on Mg alloys can be divided into two sub-layers: a very thin but dense inner layer and thick porous outer layer [4,8]. Of these layers, the porosity of outer layer is strongly influenced by the various anodizing parameters such as the electrolyte, concentration, temperature, electric field applied, and so on. The formation of compact anodic films on Mg alloys is limited, because MgO has a molar volume of  $11.3 \text{ cm}^3 \text{ mol}^{-1}$ , whereas metallic Mg has a molar volume of  $14.0 \text{ cm}^3 \text{ mol}^{-1}$ , and therefore the Pilling-Bedworth ratio is 0.81 [4,21]. In this context, several researchers have elucidated the mechanism for the corrosion of the anodic film through the two types of pores, i.e., the non-through-pores and through-pores [22,23]. In addition, many researchers have examined the causal relationship between the microstructure (such as the sizes and distribution of pores) and electrochemical characteristics of anodized Mg alloys [24–26]. Thus, the pore characteristics of the anodic film are fundamental consideration in the accurate evaluation of the corrosion performance of anodic films. Such a porous film will allow corrosive media to reach the substrate alloy easily; it will not offer any protection and will instead accelerate galvanic and general corrosion. Moreover, spongy nature of this film may reduce its adhesion with the substrate.

Otherwise, post-treatments (e.g., sealing treatments) must be considered as a critical step for achieving corrosion resistance for porous anodized Mg alloys. These sealing treatments are often carried out in boiling water or solutions containing silicate/phosphate to deposit low-solubility salts in the pore structures after reactions between Mg and the anions [4,26]. Song et al. [26] suggested an irreversible electroless E-coating procedure for anodized ZE41 Mg alloy carried out in a solution containing 71–82 mass% water, 16–26 mass% epoxy resin,

and 1.3 mass% titanium dioxide. However, the pH of the electroless E-coating solution was nearly neutral, so the dipping process could only last for 10 s. Hence, the porous structure of the anodized coating was not completely sealed after the dipping process alone. Nevertheless, the post-sealing procedure decreased the corrosion current density and increased polarization resistance by approximately three orders of magnitude compared to the as-anodized coupon. However, it is not clear as to whether this coating will provide long-term corrosion protection. Fujita et al. [27] reported a procedure for liquid-phase deposition (LPD) of a TiO<sub>2</sub> film in which pure Mg is dipped in a base solution containing 0.01 kmol m<sup>-3</sup> (NH<sub>4</sub>)<sub>2</sub>TiF<sub>6</sub> and 0.2 kmol m<sup>-3</sup> H<sub>3</sub>BO<sub>3</sub> at 353 K. However, the LPD process is time consuming, which limits its industrial applications. In particular, it required more than 24 h to deposit a 0.5- $\mu$ m-thick TiO<sub>2</sub> layer, and the film formed was not sufficient to enhance the corrosion resistance of Mg alloy because of the formation of micro-cracks. Organic and sol-gel coatings have also been applied to improve the corrosion protection of anodized or micro-arc oxidized Mg alloys [28,29].

In this paper, the author describe a novel anodizing technique that significantly limits the formation of micro-pores on the anodic films and thereby increases the corrosion resistance. The process involves applying the pulse potential specifically between anodic oxidation and active regions of AZ31 Mg alloy in 2 M NaOH alkaline solution at 303 K. Note that passive metals such as Cr, Ni with transpassive dissolution are not appropriate for corrosion protection by anodization [30]. Similarly, the passivity of Mg breaks down at about 2 V<sub>Ag/AgCl</sub> with high transpassive dissolution rate of various A cm<sup>-2</sup> in 2 M NaOH. However, the transpassive dissolution stops abruptly at the extended transpassive range, i.e. anodic oxidation range, which is higher than 6 V<sub>Ag/AgCl</sub> up to hundreds of volts. This property was used to develop oxide films of Mg alloys for corrosion protection. The main idea of this pulse



anodization is that the active potential may remove the weak spots on the anodic film through the potential edge effect and thereby increase the concentration of reactant species near the electrode/electrolyte interface. Moreover, we investigate the feasibility of sealing the porous structure of an as-anodized AZ31 Mg alloy with a stannate post-treatment and measure the resultant corrosion characteristics.

## REFERENCES

- [1] T. Lei, C. Ouyang, W. Tang, L. Li, and L. Zhou, *Surf. Coat. Technol.* 204 (2010) 3798.
- [2] H.K. Lim, D.H. Kim, J.Y. Lee, W.T. Kim, and D.H. Kim, *J. Alloys Compd.* 468 (2009) 308.
- [3] G. Cole, *Magnesium vision 2020: a north American automotive strategic vision for magnesium*, J. Quinn, E. Hetrick, and S. Bairley, Eds., Southfield, MI: USAMP, 2006.
- [4] C. Blawert, W. Dietzel, E. Ghali, and G. Song, *Adv. Eng. Mater.* 8(6) (2006) 511.
- [5] H.P. Godard, W.B. Jepson, M.R. Bothwell, and R.L. Lane, *The Corrosion of Light Metals*, Wiley and Sons, New York, 1967.
- [6] R. Lindstrom, J.E. Svensson, and L.G. Johansson, *J. Electrochem. Soc.* 149 (2002) B103.
- [7] M. Jönsson, D. Persson, and D. Thierry, *Corros. Sci.* 49 (2007) 1540.
- [8] J. Zhang, C. Wu, *Recent Patents on Corrosion Science* 2 (2010) 55.
- [9] O. Khaselev, D. Weiss, and J. Yahalom, *J. Electrochem. Soc.* 146 (1999) 1757.
- [10] Y.S. Jang, Y.K. Kim, I.S. Park, S.J. Lee, M.H. Lee, J.M. Yoon, and T.S. Bae, *Surf. Interface Anal.* 41 (2009) 524.
- [11] D.Y. Hwang, Y.M. Kim, D.Y. Park, B.Y. Yoo, and D.H. Shin, *Electrochim. Acta* 54 (2009) 5479.
- [12] Z. Shi, G. Song, and A. Atrens, *Corros. Sci.* 48 (2006) 1939.
- [13] H. Duan, C. Yan, and F. Wang, *Electrochim. Acta* 52 (2007) 3785.
- [14] X. Guo, M. An, *Corros. Sci.* 52 (2010) 4017.
- [15] L. Chai, X. Yu, Z. Yang, Y. Wang, and M. Okido, *Corros. Sci.* 50 (2008) 3274.
- [16] S. Verdier, M. Boinst, S. Maximovitch, and F. Dalard, *Corros. Sci.* 47 (2005) 1429.
- [17] A.D. Juhl, Ph.D. thesis, Pulse anodizing of extruded, cast aluminium alloys, Inst. of

- Manufacturing Engineering, The Technical University of Denmark (1999).
- [18] J.G. Qian, C. Wang, D. Li, G.L. Guo, and G.L. Song, *Trans. Nonferrous Met. Soc. China* 18 (2008) 19.
- [19] X. Liu, T. Zhang, Y. Shao, G. Meng, and F. Wang, *Corros. Sci.* 51 (2009) 1772.
- [20] S.A. Salman, R. Ichino, and M. Okido, *Int. J. Corros.* 2010 (2010) 7.
- [21] E.A. Carter, T.F. Barton, and G.A. Wright, *Surface Treatment 99: 4th International Conference on Computer Methods and Experimental Measurements for Surface Treatment Effects*, Assisi, Italy (1999) pp. 169.
- [22] Z. Shi, G. Song, and A. Atrens, *Corros. Sci.* 47 (2005) 2760.
- [23] H. Ardelean, I. Frateur, S. Zanna, A. Atrens, and P. Marcus, *Corros. Sci.* 51 (2009) 3030.
- [24] V. Tchervyakov, G. Gao, J. Bombach, A.P. Pchel'nikov, and G. Cole, *Magnesium Technology 2000*, TMS (2000) pp. 143.
- [25] R.F. Zhang, D.Y. Shan, R.S. Chen, and E.H. Han, *Mater. Chem. Phys.* 107 (2008) 356.
- [26] C. Blawert, V. Heitmann, W. Dietzel, H.M. Nykyforchyn, and M.D. Klakiv, *Surf. Coat. Technol.* 200 (2005) 68.
- [27] R. Fujita, M. Sakairi, T. Kikuchi, and S. Nagata, *Electrochim. Acta* 56 (2011) 7180.
- [28] H. Duan, K. Du, C. Yan, and F. Wang, *Electrochim. Acta* 51 (2006) 2898.
- [29] A.L.K. Tan, A.M. Soutar, I.F. Annergren, and Y.N. Liu, *Surf. Coat. Technol.* 198 (2005) 478.
- [30] "Study of anodic metal passivation by cyclic voltammetry", <http://phys.chem.elte.hu/Sziraki/mscfizkemlab13/passhandout13.pdf>, p. 3, 2013.

## **II. Literature Survey, Research Background and objective**

## **2-1. Literature Survey**

### **2.1.1. Metallurgy of Magnesium**

For almost all alloy systems, a maximum concentration of solute atoms dissolves in matrix to form a solid solution. This limit is called as solubility limit and changes with temperature. If the amount of solute available is more than the solubility limit, different phase, either a solid solution or compound, will form. Therefore, the efficiency of Mg is not only resulted from its physical properties, but various constituents added. In other words, the corrosion behavior of Mg and its alloys strongly depends on the alloying elements and impurity elements. For binary Mg-M system, Al (< 12.7 mass%) [1], Zn (< 6.2 mass%) [2] and Mn (< 2.2 mass% ) [3] are generally acceptable. Only with appropriate metallurgical manipulation, their corrosion protection effect can be improved [4]. Moreover, it can improve the ease of manufacturing. Hence, we want to add alloying elements that are beneficial to the corrosion resistance and remove impurity elements that are detrimental to the corrosion resistance [5].

#### **2.1.1.1. Alloying Elements**

Aluminum has the most favorable effect on Mg, compared to any of the alloying elements. As the content of Al increases, from 0% to 4%, the corrosion resistance of Mg alloys drastically enhanced [6]. However, from 4% to 9%, the improvement in corrosion resistance is less obvious. Nevertheless, the surface corrosion of Mg significantly impeded in

active environments when alloyed from 4% up to 10%, as shown in Fig. 2.1 [6]. Moreover, the Mg alloys become heat treatable when exceeds 6%. The Al partially dissolved into the  $\alpha$ -Mg (solid solution) and partially exists as a precipitates of  $\beta$ -Mg<sub>17</sub>Al<sub>12</sub> [7]. The  $\beta$ -phase normally placed in the grain boundary of  $\alpha$ -matrix, and it has a lamellar (plate-like) structure. Besides the  $\beta$ -phase, some other Mg-Al particles such as Mg<sub>5</sub>Al<sub>8</sub> and Mg<sub>2</sub>Al<sub>3</sub> could co-exist. However, it is believed that only the  $\beta$ -phase plays a beneficial role as a corrosion barrier for Mg alloys [8–10]. This is attributed to a change in the composition of surface corrosion products in a corrosive media. On the other hand, some authors have been reported a negative effect of Al addition on the corrosion resistance of Mg. Hillis et al. reported that the corrosion resistance deteriorated as the content of Al addition increases [11]. Moreover, Emley et al. have demonstrated that Al decreases the tolerance limit of Fe from about 170 ppm to 20 ppm [12]. Hence, the purity of Mg alloy should be improved for higher Al content. Otherwise, the addition of Mn to Mg counteracts this effect.

Manganese also added to almost all the commercialized Mg alloys. The Mn addition does not directly affect the corrosion resistance of Mg alloys. Instead, the detrimental effects of impurities such as Fe, Ni, and Cu, when their concentration exceeds the limits of critical tolerance, can be reduced [13]. The detrimental effect of impurities is that it increases the corrosion rate of Mg. However, the addition of Mn to about 1–2% definitely reduces their corrosion rate. Otherwise, the limits, set for the impurity levels to below recommended tolerance limits, can enhance the usefulness of Mg alloys [14]. In particular, Mg-Al alloy system is susceptible to Fe inclusion. The tolerance limit of Fe impurity reduces from 0.017% to below a few thousandth of one percent in  $\alpha$ -Mg. However, the addition of Mn around 1% increases the tolerance level to around 0.002% for Fe in binary Mg-Al alloys [15]. It seems that the Mn element surrounds the Fe impurities, isolating them from the  $\alpha$ -Mg [16].

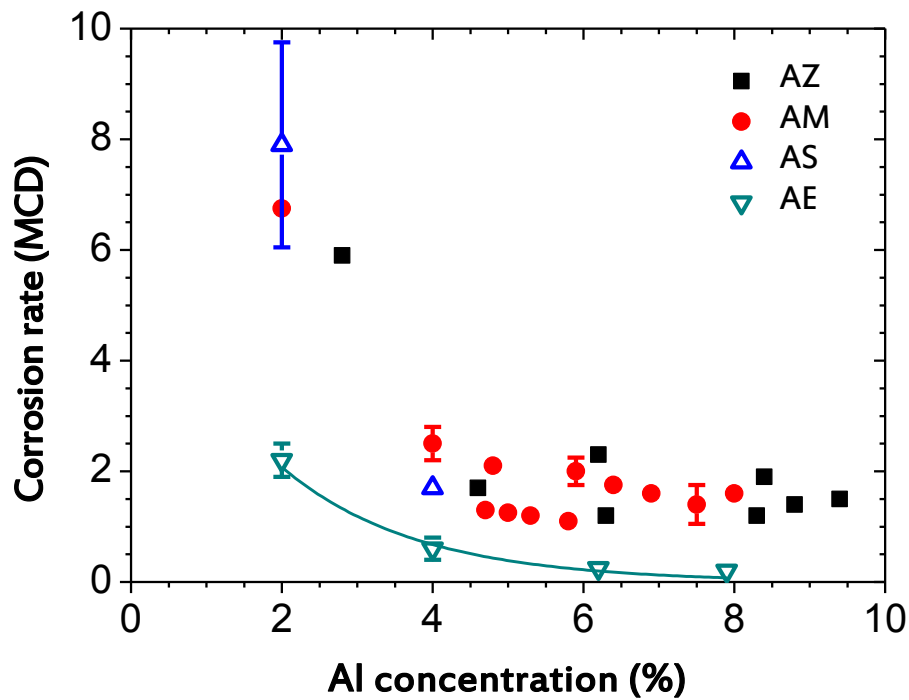


Fig. 2.1. Effect of Al concentration on the corrosion rate of die-cast magnesium alloys in 5 wt% NaCl solution [6].

Zinc is next to Al in effectiveness, as an alloying constituent in Mg. It is frequently used in combination with Al. As a rule, the solubility of Zn in Mg is around 1.1 wt.% (0.5 at.%) at room temperature. Therefore, for typical AZ91, Zn distributes in the same proportion in both the  $\alpha$ -Mg and  $\beta$ -precipitates. Like Mn, Zn also helps overcome the harmful corrosive effect of impurities such as Fe or Ni [13]. However, Mn has better performance to raise the tolerance limit of the impurities than Zn, if the Zn amount is equal to the Mn [15]. When Zn is added above 5 wt.% and manufactured by rapid solidification, the corrosion resistance of Mg alloy can unexpectedly be deteriorated. The lowest corrosion resistance was observed at adding 18.6 wt.% of Zn [18].

Calcium is a special alloying component, adding a very small amount. Ca, as well as Zn, acts as grain refining agents that can improve both corrosion and mechanical properties [19]. Moreover, it reduces oxidation of the alloy in the molten condition and during heat treatment, and improves their rollability [20]. In the Mg-Al alloys system,  $Mg_{17}Al_{12}$  secondary phase exhibits a low thermal stability and their creep properties undergo a rapid degradation at elevated temperature above 120°C, which limits the application to car engine parts [21]. In recent years, rare earth elements such as Y, Nb, La, and Ce were found to enhance the structure and mechanical properties including creep resistance and strength of Mg alloys [22,23]. However, these elements cause a substantial increase of alloy cost. Alternatively, the addition of Al and low-cost Ca to Mg was proven to be an effective way to improve the mechanical properties of Mg alloys by forming C36 Laves  $Al_2Ca$  phase during solidification and homogenization processes [24–28].

#### **2.1.1.2. Impurity Elements**

Makar et al. carried out a test with 14 elements, as an alloying element for Mg, and the corrosion rate was measured in 3 wt.% NaCl [29]. As shown in Fig. 2.2 and Fig. 2.3, the elements of Co, Cu, Fe, and Ni exhibited the greatest effect on accelerating corrosion even at very low concentration, while Ag, Ca, and Zn had lower effect. On the other hand, Al, Cd, Mn, Na, and Si had a little or no negative effect at concentration below 5%. Cu, Fe, or Ni at 0.2% increases the corrosion rate approximately 100-folds, since the solid solubility for these elements is very low [29,30]. The solubility of impurities in Mg matrix determines their tolerance limits. Therefore, when the impurity concentration is higher than the tolerance limit, they easily segregate and become an active catalytic site for severe corrosion attack [31].



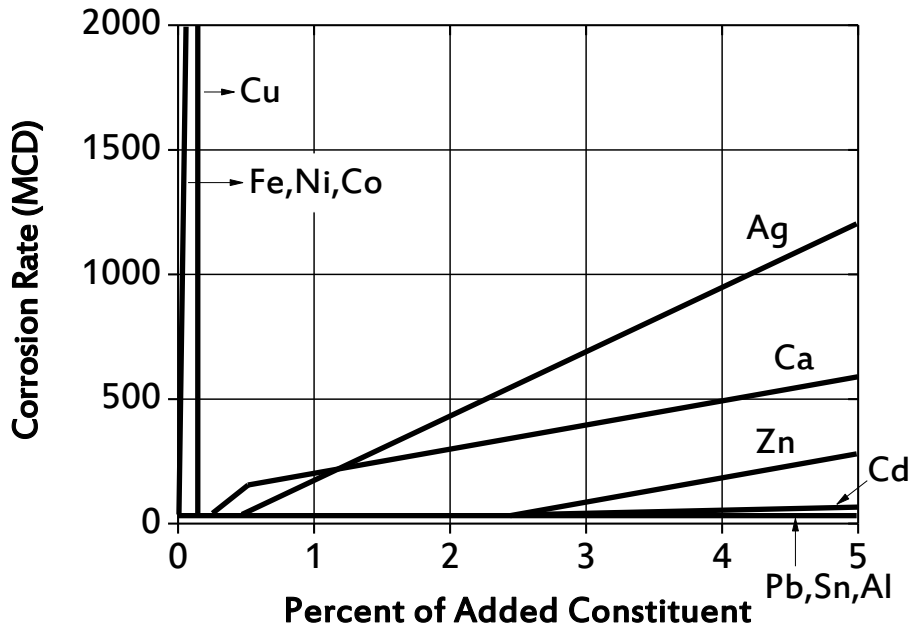


Fig. 2.2. Effect of various alloying elements on the corrosion rate of magnesium alloys [29].

However, below their tolerance limits, there is little or no effect on accelerating corrosion [32]. Hence, it is important to improve the purity of the alloys. The tolerance limit can be changed by different manufacturing processes. Marker et al. have reported that a higher Ni tolerance limit can be achieved with higher solidification rate during casting [29].

### 2.1.2. Corrosion of Magnesium

The corrosion aspects of Mg alloys depend on various factors, mainly on pH values of surrounding medium and near the metal surface and on the nature of surface film being formed. The corrosion resistance of surface film is dependent of the alloy composition. Also, the type and distribution of intermetallics have very important effect. Therefore, a fabrication

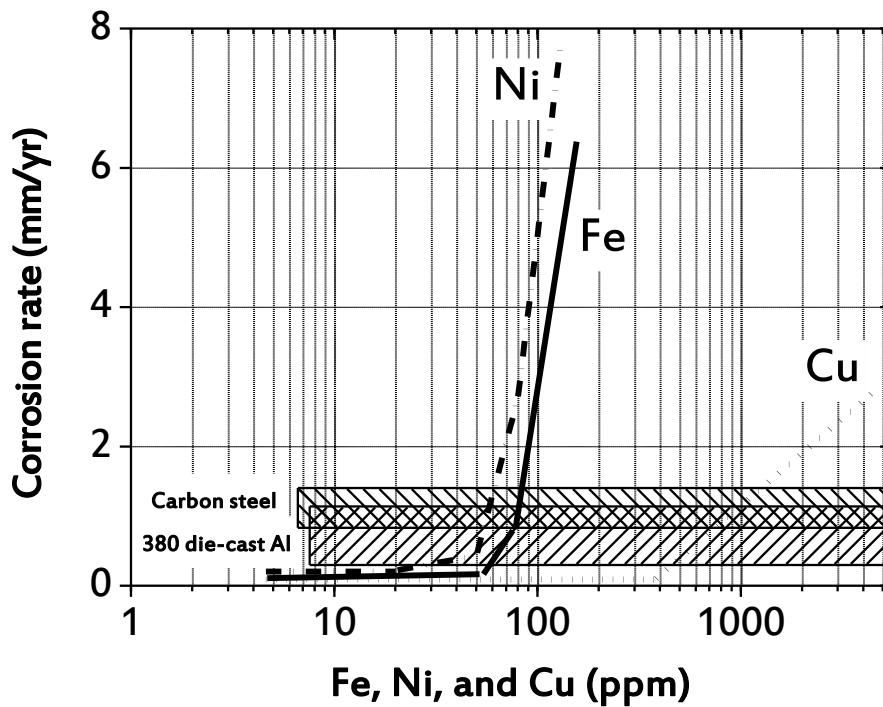


Fig. 2.3. Effect of Ni, Fe, and Cu impurities on the corrosion rate of die-cast AZ91 magnesium alloys during salt spray tests [30].

history, metallographic examination, and accurate composition analysis are necessary for the interpretation of corrosion characteristic. The publications of Makar et al. [33], Kainer [34], Hansen [35], and Song et al. [36] have elucidated the essential aspects of the corrosion behavior of Mg alloys such as the type and mechanism of corrosion and the effect of surrounding medium.

If a pH of solution is above 12, a self-healing stable oxide film, which provides high corrosion resistance, develops on its surface. This oxide film becomes in a conditionally unstable state for a pH range of 10–11 (see Fig. 2.12). With decreasing pH value more, a rate of hydrogen evolution starts to increase because of the active dissolution on the oxide-free

Table 2.1. Typical corrosion potential,  $E_{\text{corr}}$ , values of Mg and its secondary phases after 2 hrs of immersion in deaerated 5 wt.% NaCl solution saturated with  $\text{Mg}(\text{OH})_2$  (pH 10.5).

Type of secondary phases	$E_{\text{corr}}$ (V <sub>SCE</sub> )
Mg	-1.65
Mg <sub>2</sub> Si	-1.65
Al <sub>6</sub> Mn	-1.52
Al <sub>4</sub> Mn	-1.45
Al <sub>8</sub> Mn <sub>5</sub>	-1.25
Mg <sub>17</sub> Al <sub>12</sub> (β-phase)	-1.20
Al <sub>8</sub> Mn <sub>5</sub> (Fe)	-1.20
Beta-Mn	-1.17
Al <sub>4</sub> MM	-1.15
Al <sub>6</sub> Mn(Fe)	-1.10
Al <sub>6</sub> (MnFe)	-1.00
Al <sub>3</sub> Fe(Mn)	-0.95
Al <sub>3</sub> Fe	-0.74

area. Then, a relative thick layer of loosely adhering corrosion products are produced. However, as a result of the active dissolution and the hydrogen evolution reaction, the pH value arises in the area adjacent to the substrate. Hence, the stability of oxide film increases again.

Secondary phases have a significant influence on the corrosion behavior of Mg. Most of the alloying elements only can affect the corrosion resistance of Mg positively by forming secondary phases [37]. Some typical values of the  $E_{\text{corr}}$  of various secondary phases are given in Table 2.1 [38]. Mg is the most active, and therefore, the  $\alpha$ -Mg acts as the anode against all the secondary phases, preferentially corroding in any galvanic couple. For instance, AZ91, which includes 9% Al, has an appreciable amount of  $\beta$ -phase along the grain boundaries, as shown in Fig. 2.4. The  $\beta$ -phase is cathodic with respect to the  $\alpha$ -Mg, but often offers a passive behavior over a wide pH ranges during long immersion times. In other words, the  $\beta$ -phase has

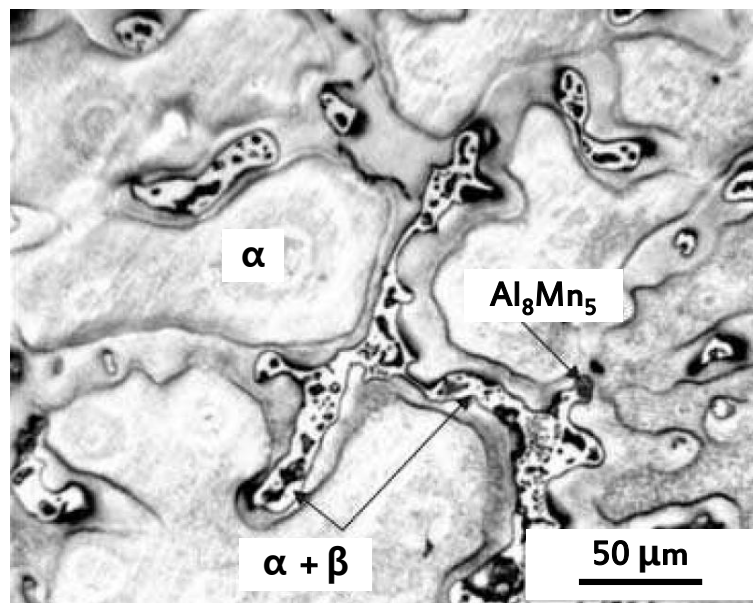


Fig. 2.4. Microstructure of AZ91 alloy (cast into a steel mould) [39].

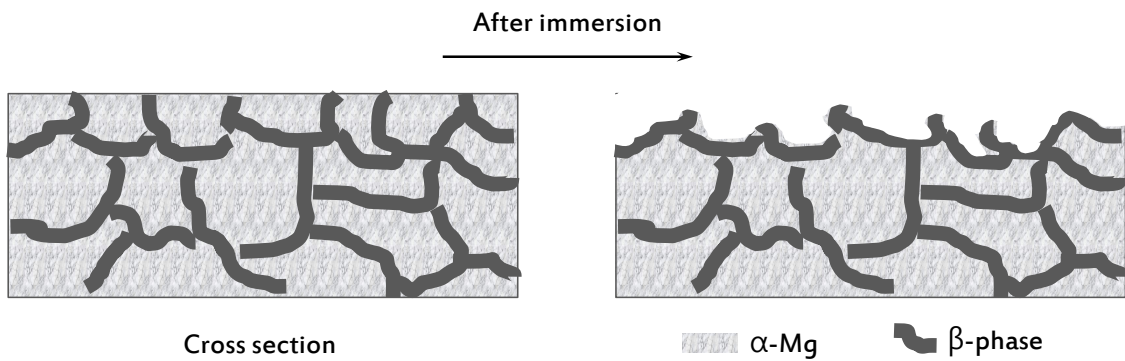


Fig. 2.5. Schematic representation for the corrosion protection effect of  $\beta$ -phase. (a)  $\beta$ -phase is nearly continuous; (b) the corrosion propagation through  $\alpha$ -Mg is effectively retarded by the  $\beta$ -phase. Corrosion products are not illustrated here [37].

two different influences on corrosion, as a galvanic cathode or as a barrier, depending on the area fraction of  $\beta$ -phase per unit area of exposed surface. An inner part of as-cast AZ91 commonly affords better corrosion resistance, as compared to its skin part, because of more continuous and a higher volume fraction of  $\beta$ -phase. If  $\alpha$ -Mg is fine and the volume fraction of  $\beta$ -phase is not too low, the gap between  $\beta$ -phase becomes narrow and nearly continuous [37]. This leads the  $\beta$ -phase not to easily fall out by undermining, obstructing its surface by protective corrosion product [37]. Figure 2.5 schematically illustrates this case. On the other hand, if  $\alpha$ -Mg is large,  $\beta$ -phase tends to agglomerate and not continuous, and therefore, the corrosion of  $\alpha$ -phase cannot be effectively blocked either by the  $\beta$ -phase or corrosion products, accelerating the corrosion of  $\alpha$ -phase [37].

On Mg and all its alloys, an unusual feature, which does not seen on other metals, appears during the corrosion in aqueous solutions, i.e. hydrogen evolution. The potentials at which Mg dissolves are sufficiently low so that hydrogen evolution dominates oxygen

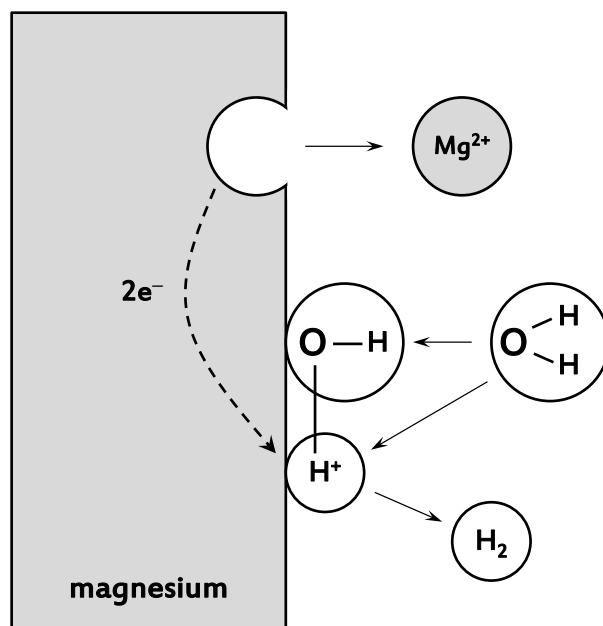


Fig. 2.6. Electrochemical reactions occurring on the magnesium during corrosion in neutral water.

reduction at all pH values [40]. The hydrogen evolution reaction continues at a significant rate even when an Mg surface is anodically polarized above its corrosion potential (around  $-1.5 V_{SCE}$ ) [41–43]. Interestingly, the rate of hydrogen evolution often increases as the anodic polarization increases [41–43]. According to standard electrochemical kinetics, the rate of a cathodic reaction like hydrogen evolution from the reduction of  $H_2O$  or  $H_3O^+$  should decrease exponentially rather than increase, with increasing potential [40].

Assuming that Mg dissolves to form the divalent  $Mg^{2+}$  ions accompanied by the generation of hydrogen gas by the water reduction, the reactions involved are (Fig. 2.6):





The currents from reactions (1) and (2) can be defined as  $i_a$  and  $i_c$ , respectively. Under open circuit condition, the anodic reaction of Mg dissolution is balanced by an equal rate of hydrogen evolution reaction [40]. In this case,  $i_a$  is equal to  $i_c$ . However, under anodic polarization conditions, Mg dissolution will occur at a higher rate than at open circuit condition [40]. Using Faraday's law, the rate of Mg dissolution during the anodic polarization times can be evaluated by measuring sample mass loss [40,44]. However, some of the excess electrons formed by anodic reaction are consumed by copious hydrogen evolution reaction on the electrode surface rather than flowing through the potentiostat. Hence, the average net current density supplied to the Mg electrode by the potentiostat,  $i_{\text{net}}$ , might be less than the anodic current density [40]. Therefore, at applied electricity, the net current density can be defined as the difference between the total anodic and cathodic current densities as follows densities (assuming the area for both the anodic and cathodic reactions is the nominal exposed area) [40]:

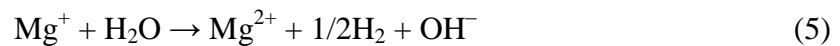
$$i_{\text{net}} = i_a - i_c \quad (3)$$

According to activation-controlled kinetics for the hydrogen evolution reaction,  $i_c$  decreases as the applied anodic potential increases above  $E_{\text{OCP}}$  [40]. However, for Mg, the rate of hydrogen evolution inevitably increases with the applied anodic potential, is often referred to as the "Negative Difference Effect". This effect has been discussed by many previous studies [45–49]. To explain the negative difference effect of Mg during the corrosion,

the existence of an  $\text{Mg}^+$  intermediate was introduced by Petty et al. in 1954, later by Song et al. in 1997 [46,50]:



In this electrochemical reaction, Mg dissolves to form univalent  $\text{Mg}^+$ , not divalent  $\text{Mg}^{2+}$ . Moreover, the following chemical reaction is presumed to explain further oxidation of univalent  $\text{Mg}^+$  to form divalent  $\text{Mg}^{2+}$ , along with hydrogen gas. This explanation involves the assumption that some fraction of univalent  $\text{Mg}^+$  exists long enough to disengage from the Mg surface:



These reactions would account for the observation of increasing rates of hydrogen production with increasing anodic potential in certain corrosive media [40]. Although they are not explicitly stating the mechanism involving univalent  $\text{Mg}^+$  [46], it can be supported by the theory that single-step reactions are rare in electrochemistry, particularly for multi-electron transfer reactions [51]. Therefore, it is predicted that the rate of  $\text{Mg}^+$  formation increases with increasing the rate of Mg dissolution. However, the existence of  $\text{Mg}^+$  has never been proved [40].

Recently, Frankel et al. have found that the total amount of hydrogen collected for a fixed charge decreases with increasing current density [40]. This evidence strongly contradicts any assertions of the existence of univalent  $\text{Mg}^+$  on the basis that the total amount of hydrogen evolution should be identical for the same amount of  $\text{Mg}^+$  produced by the



reaction (4) [40]. Instead, they have proposed the new mechanism that an exchange current density for the hydrogen evolution reaction,  $i_{0,H,M}$ , increases with increasing the rate of Mg dissolution. In other words, the catalytic activity of dissolving Mg surface for the hydrogen evolution reaction can increase with increasing Mg dissolution rate. An analysis suggests that the  $i_{0,H,M}$  may increase by many orders of magnitude with the applied anodic potential.

## 2.1.3. Anodizing of Magnesium

### 2.1.3.1. General Remark

Anodizing is an electrochemical process for producing a stable, thick oxide films on the surface of valve metals (such as Mg, Ti, Al, V, etc.). The stages for anodizing process include [52]; (i) mechanical pre-treatment, (ii) cleaning, degreasing, and pickling, (iii) anodizing (DC or AC or pulse), (iv) post-treatment (dyeing or sealing). This subchapter describes the basics of pre-treatment and anodizing processes. Then, the following subchapters will describe

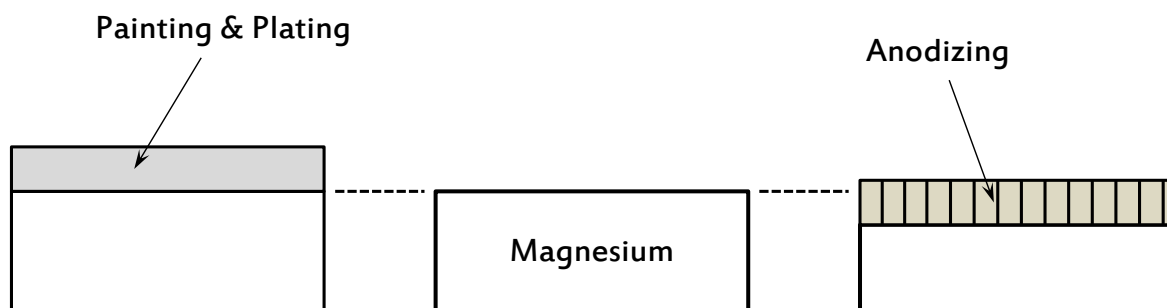


Fig. 2.7. Dimensional effect of anodizing, painting, and plating.

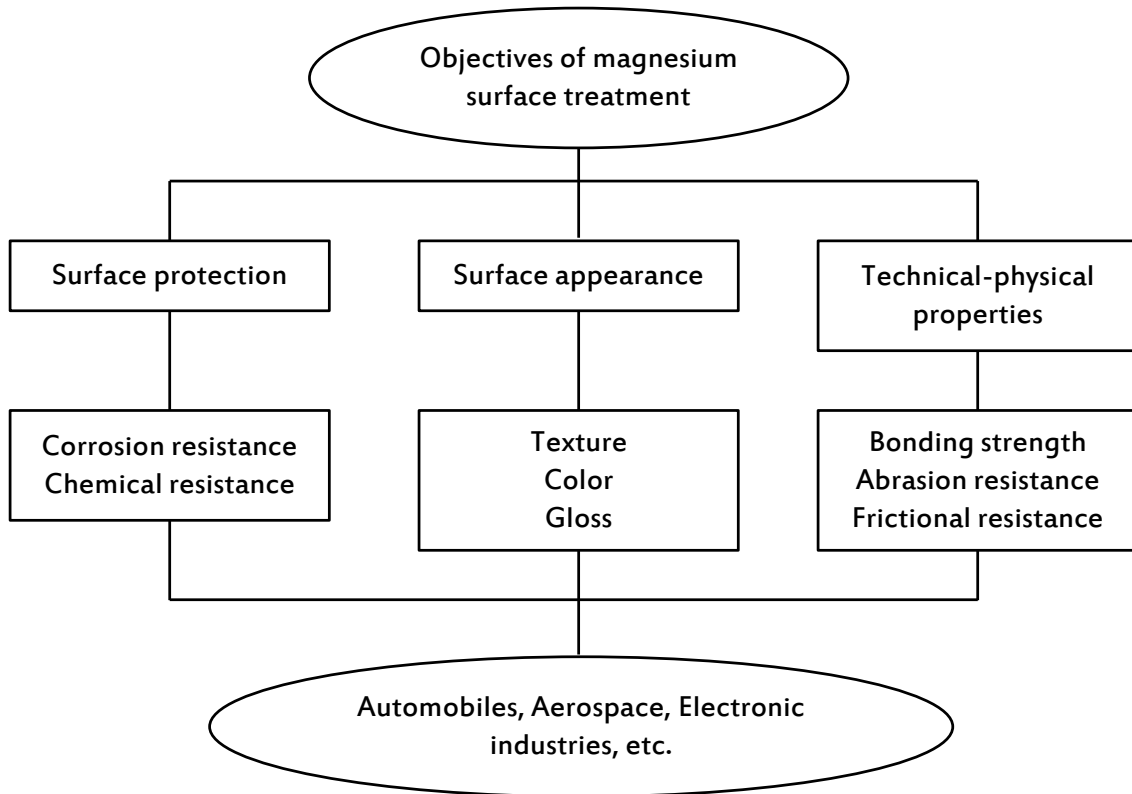


Fig. 2.8. Objectives of magnesium surface treatments.

about the pulse anodizing and subsequent post-treatment processes.

Anodic films are produced by reaction of metal with ions in electrolyte, and after anodizing, there is an overall slight increase in dimension. The major difference in dimension among anodizing, painting, and electroplating is that the anodizing proceeds underneath the substrate while the painting and electroplating are deposited on the substrate, as shown in Fig. 2.7. The valve metals, especially for Mg, have strong affinity for oxygen [53]. Thus, a very thin oxide film covers the surface of a freshly-cut piece of magnesium when exposed to the ambient atmosphere. By providing an anodic potential or current, the natural oxide layer becomes thicker, and therefore, results in a better corrosion and wear resistances. Therefore,

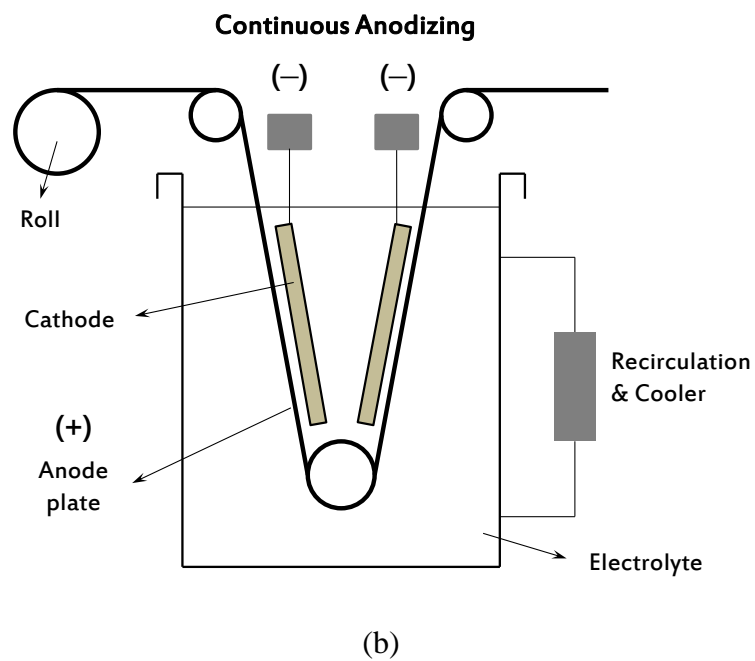
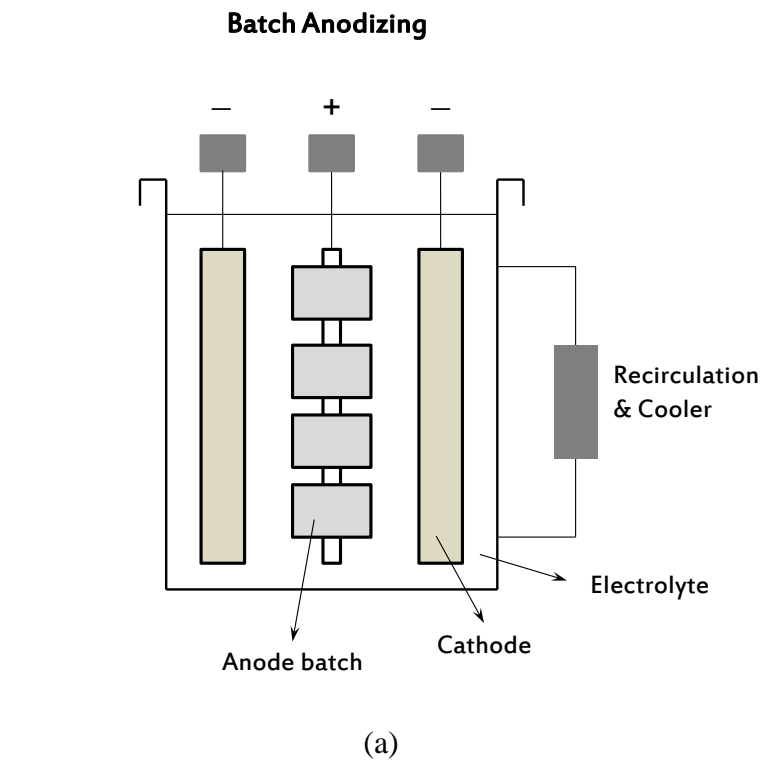


Fig. 2.9. Typical anodizing cells: (a) Batch anodizing, (b) Continuous anodizing [57].

anodizing is the most common surface treatments of magnesium alloys. As shown in Fig. 2.8, for various magnesium alloys, the anodizing is necessary to provide a greater degree of protection against the moisture (improving electrochemical and chemical resistances), to modify the surface appearance (texture, color, gloss, etc.), and to create technical-physical surface properties (increasing bonding strength, abrasion resistance, and frictional resistance, etc.), alike the anodizing of Al alloys [54]. In recent years, the anodizing is primarily used to produce an undercoating layer to provide better adhesion for various organic finishes [55,56]. A thin anodic film of around 5  $\mu\text{m}$  is sufficient for this [57]. A thicker anodic film of around 25  $\mu\text{m}$  and up can provide mild corrosion resistance after sealing with oil, wax, or metal salts [57]. Standards of Mg anodizing process are given in AMS 2466, AMS 2478, AMS 2479, and ASTM B893.

Figure 2.9 shows two types of anodizing cell for Magnesium alloys [57]. In an anodizing cell, the magnesium workpiece is used as anode which is connected to the positive terminal of a power supply. The other suitable metal or alloy is made as cathode by connecting to the negative terminal. The cathode material is usually a rod or plate of carbon, lead, nickel, and stainless steel which is unreactive electronic conductor in the anodizing bath [58]. Then, an anodic film produced on the Mg alloys in a large variety of alkaline solutions with DC, AC or a combination of both. When the circuit is closed, electrons transfer from the magnesium workpiece to the cathode leading ions, at the magnesium surface to react with  $\text{H}_2\text{O}$  and  $\text{OH}^-$  to form an oxide or hydroxide layers on the magnesium alloys. This anodic reaction actually develops enough energy to dissociate water with excess electrons at both the cathode and the magnesium surfaces. The water splitting cathodic reaction disturb the balance between the acidic hydrogen ( $\text{H}^+$ ) ions and the alkaline hydroxyl ( $\text{OH}^-$ ) ions, and therefore, make the solution less acidic or more alkaline [59].

### 2.1.3.2. Pulse Anodizing

Pulse anodizing between two values of direct voltage or current, instead of applying the same value, can give several benefits of individual process conditions over the whole process. Thus far, many researchers have made suggestions regarding the designation of this pulse

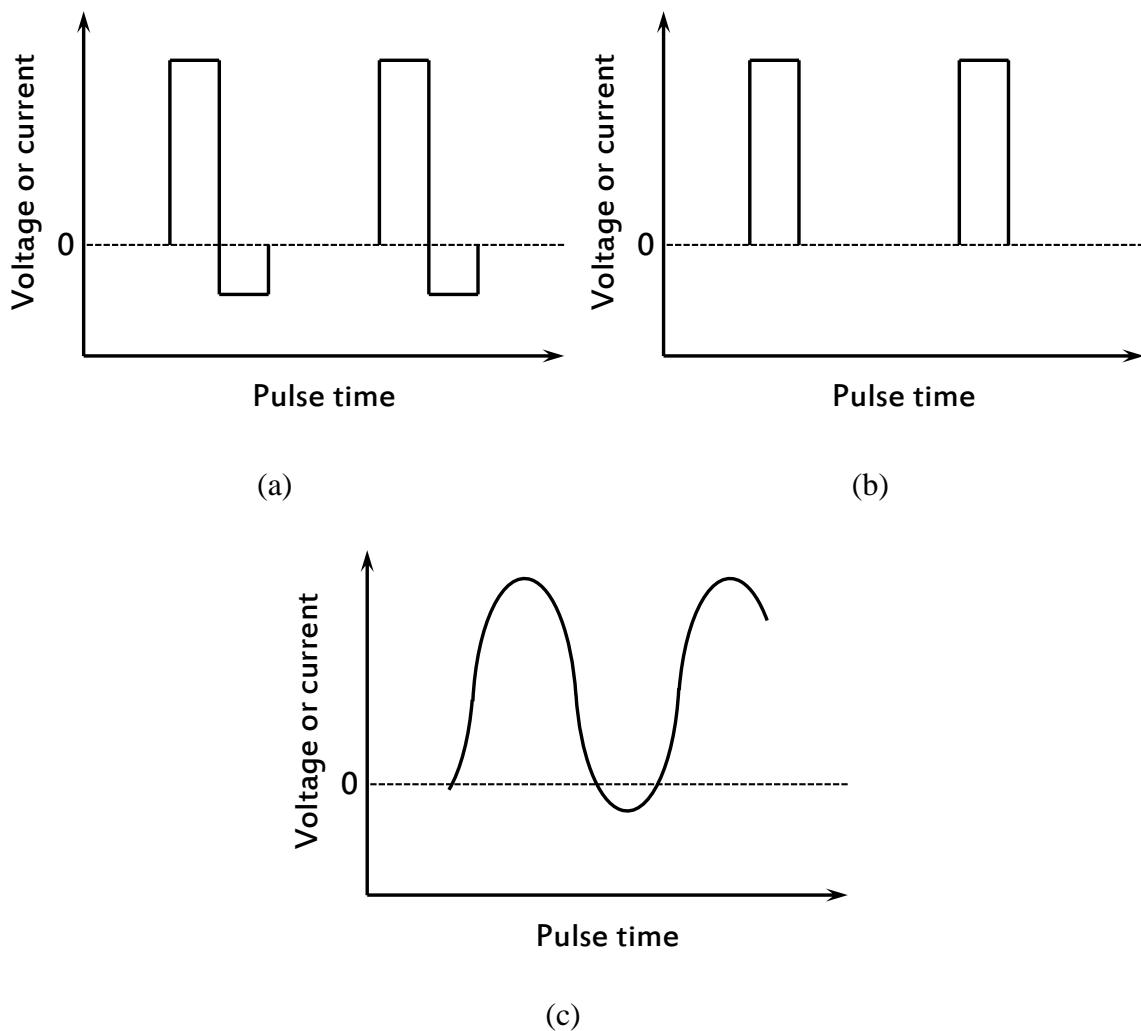


Fig. 2.10. Schematic diagram of various wave forms of pulse anodizing; (a) periodic reverse; (b) square; (c) asymmetric sine.

waveform. Typical schematic diagrams of the various waveforms of pulse are shown in Fig. 2.10. Three different waveforms, i.e. asymmetric sine, and square pulses, and periodic reverse, can be compared with conventional direct anodizing process.

During anodizing process under constant voltage or current, reactant species can become depleted near the interface, namely, the electrode surface–outer Helmholtz layer distance [60]. However, the periodic reverse waveform during the anodizing can replenish the reactant species from the bulk solution when the electric source alters the polarity and allows the working electrode to act as a cathode (Fig. 2.10a). Moreover, the surface protrusions of thickened anodic film can be removed, resulting in the smooth surface [61]. On the other hand, unexpected pits and cavities may form in the anodic film if the rate of anodic dissolution is intensified. AC anodizing process uses the asymmetric sine waveform which alternating voltage or current with various frequencies (Fig. 2.10c). However, AC anodizing

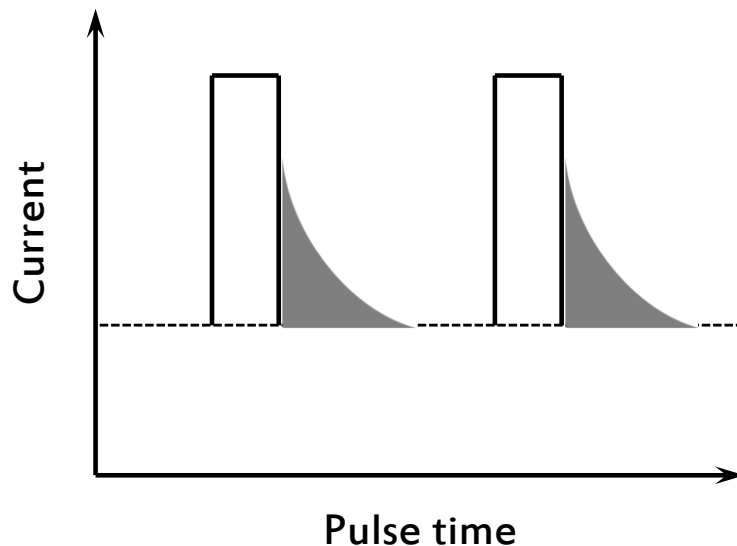


Fig. 2.11. Schematic diagram of capacitance effect by pulse.

is not commonly used. This is because AC anodizing requires the sources of higher voltage and approximately 50% more effective current, when compared to DC anodizing [62]. If the maximum current density is too high, the reactant species can be easily replenished from the metal surface, allowing the capacitance effect, as shown in Fig. 2.11. This can lead to the formation of granular and sponge type of anodic films and weaken the adhesion strength to the substrate.

Several studies have explored the idea of using a pulse current or potential (pulse anodizing) instead of a constant value to get a higher mean current density and thereby decrease the processing time and total energy consumption [63]. Qian et al. [64] applied a square pulse current of 0–40 mA cm<sup>-2</sup> for 10–30 min on AZ91D Mg alloy in a NaOH solution containing meta-silicates, borates and other additives. However, a porous oxide layer still formed and the micro-pores actually seemed to widen with increasing anodizing time. Duan et al. [65] obtained plasma electrolytic oxidation (PEO) films on AZ91D Mg alloy by applying a square pulse potential of 350–400 V for 1–2 h in a KOH solution containing various additives. Though they found that fluoride- and phosphate-containing electrolytes were the most effective in improving the corrosion resistance of AZ91D Mg alloy, micro-pores still remained in the anodic films. Liu et al. [66] obtained a protective passive film on pure Mg by applying pulse potential between passive (-0.5 V<sub>SCE</sub>) and passive/active regions (-1.36 V<sub>SCE</sub>) for 30 min in 0.25 M Na<sub>2</sub>SO<sub>4</sub> + 0.1 M NaOH solution.

### **2.1.3.3. Thermodynamic Stability of Mg Compounds**

Investigations into the growth mechanism of anodic films on Mg have produced basic electrochemical understandings for Mg in aqueous solutions. As shown in Fig. 2.12, the

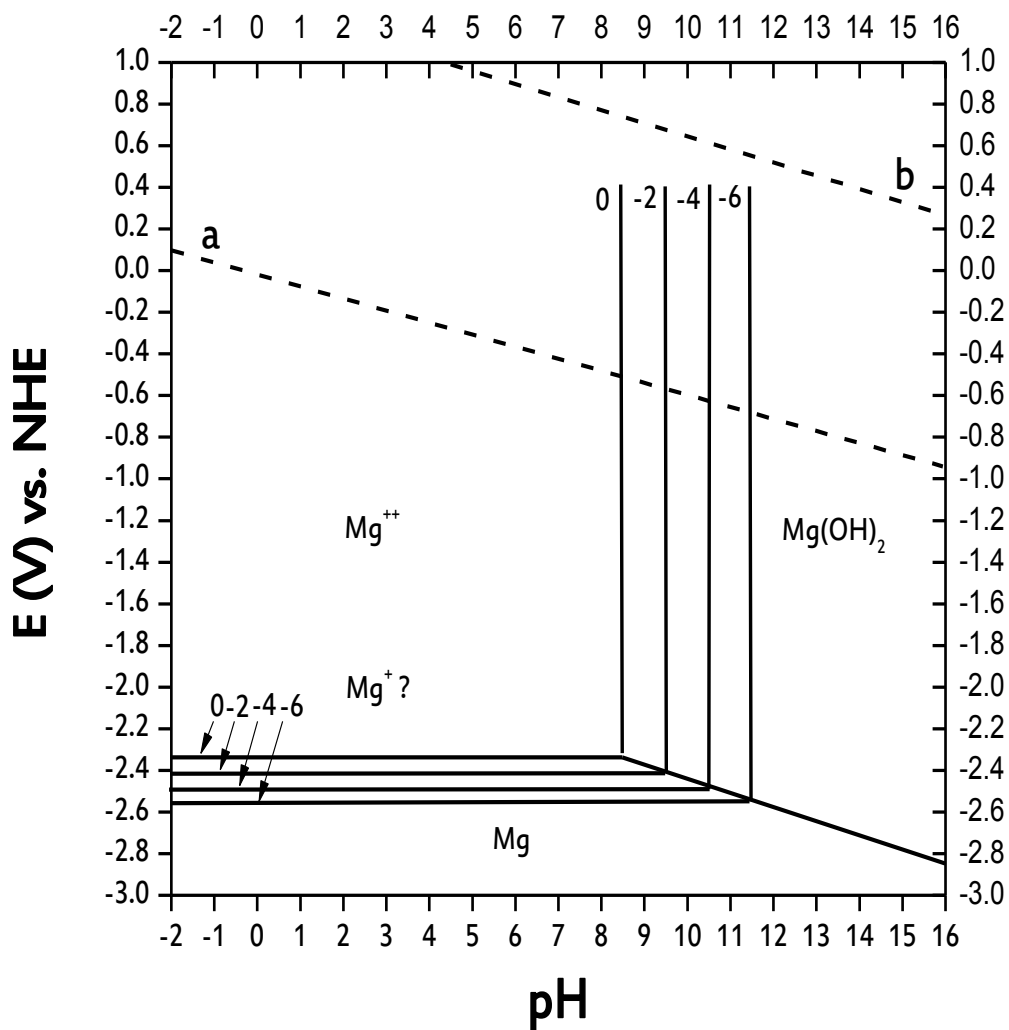
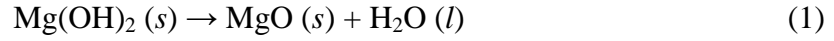


Fig. 2.12. Pourbaix diagram of pure magnesium

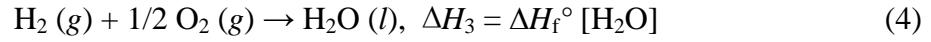
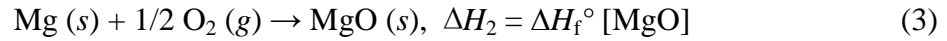
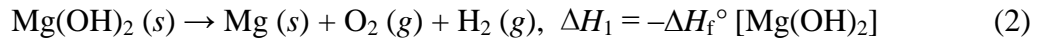
electrochemical phase diagram of Mg, first presented by Pourbaix, shows the thermodynamically stable forms of that compounds, i.e. the state having the lowest free energy, mapped as a function of potential, pH, and hydrogen ion activity at a given temperature and pressure [67]. In acidic or neutral solutions, Mg rapidly dissolves, and spontaneously evolving H<sub>2</sub> gas. On the other hand, in strong alkaline solutions, a reaction with H<sub>2</sub>O produces a thick, passive Mg(OH)<sub>2</sub> film which is thermodynamically favored over



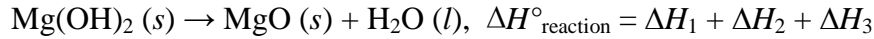
a MgO, according to the following calculations of standard enthalpy change.



Rewrite the equation (1) as the sum of three formation reactions:



Therefore,

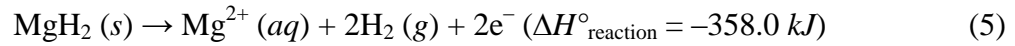


$$\Delta H^\circ_{\text{reaction}} = (924.7 \text{ kJ}) + (-601.8 \text{ kJ}) + (-285.8 \text{ kJ}) = 37.1 \text{ kJ}$$

During anodizing at high electric field, it is assumed that naturally formed Mg(OH)<sub>2</sub> loses its protons to form meta-stable MgO. However, Mg(OH)<sub>2</sub> layer will form again on the surface of MgO layer when immersed in water. The Mg(OH)<sub>2</sub> has lower solubility constant ( $K_{\text{sp}} = 1.8 \times 10^{-11}$ ), when compared to the MgO ( $K_{\text{sp}} = 2.37 \times 10^{-8}$ ) [68].

Perrault et al. have investigated the thermodynamic stability of MgH<sub>2</sub> in aqueous solutions, and concluded that the MgH<sub>2</sub> is stable in neutral and alkaline solutions, leading to a passivity of Mg surface together with Mg(OH)<sub>2</sub> [69]. However, the negative value of standard enthalpy change in reaction (5) shows that MgH<sub>2</sub> is unlikely to form in aqueous solutions, and will spontaneously decompose to Mg<sup>2+</sup> ions. Hence, the primary passivity phenomenon

of Mg is generally believed to be the result of the presence of Mg(OH)<sub>2</sub> which gives protection against corrosion over a range of pH values.



However, unfortunately, the native Mg(OH)<sub>2</sub> and MgO films are loose in neutral and acidic aqueous conditions, and therefore, cannot provide sufficient protection to resist degradation encountered in the physiological environment containing Cl<sup>-</sup> ions. This is because Cl<sup>-</sup> ions can transform the surface of Mg(OH)<sub>2</sub> into more soluble MgCl<sub>2</sub>. The dissolution of Mg(OH)<sub>2</sub> makes the surface more active and reduces the protected area, and hence, promotes further dissolution of Mg. The reactions proceed as follows [70,71]:



#### 2.1.3.4. Anodizing Behavior

Anodizing can be carried out under either voltage or current controlled. During initial period, the Mg piece is protected by a thin oxide film which offers small resistance to current. Under voltage control, a rapid rise of current is produced, followed by a slow drop to a steady-state value with anodizing time, as shown in Fig. 2.13. These current contributions are related to a series of destruction, nucleation, and growth process of anodic film on the electrode surface. An increase in the thickness of anodic film, proportionally to the charge per surface area, and thereby an increase in resistance causes the decrease in current. Finally, the

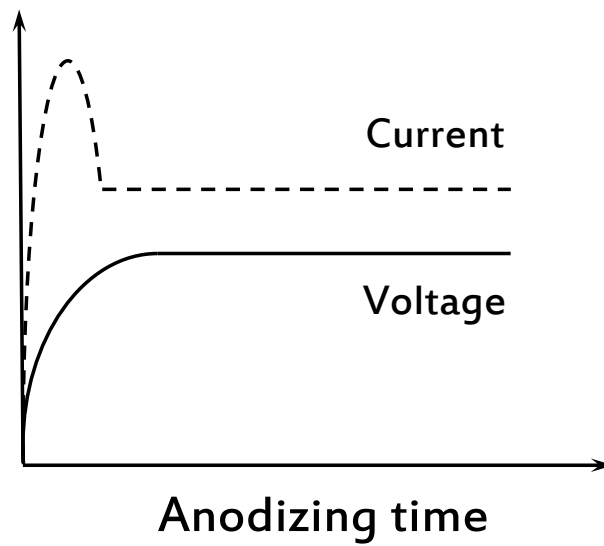


Fig. 2.13. Changes in voltage and current responses during anodizing at constant current and constant voltage, respectively.

current reaches a constant level, where the rate of anodic dissolution and anodic film formation reached a steady state. Under current control, the voltage increases with anodizing time for maintaining the current applied while the isolating anodic film is growing.

In general, various Mg alloys show different active and passive states. Moreover, at different anodizing voltage or current conditions, the formation of anodic films have different patterns. [Figure 2.14](#) schematically illustrates the voltage dependence of oxide formation on the Mg electrode. The anodizing using sparking, micro-arcing, and arcing are usually high-voltage processes. At present, most of the anodizing industries utilize spark discharges to convert the Mg surface into a ceramic oxide [\[72\]](#).

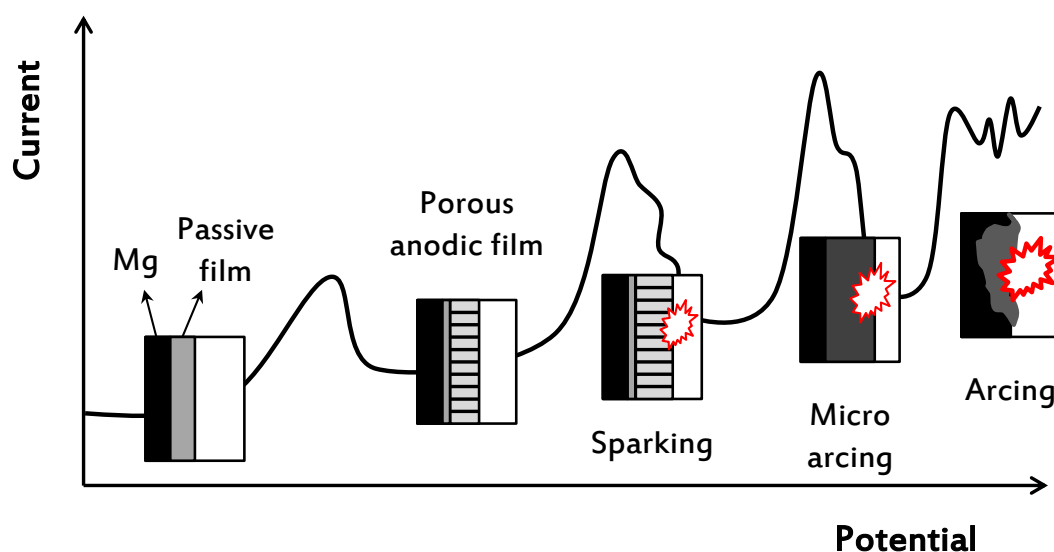


Fig. 2.14. Schematic diagram for the voltage dependence of oxide formation on the magnesium [72].

The first description for the formation of Mg anodic film was given by Huber (1953) [73]. He showed the relationship between the anodizing voltage and the consequential film characteristics of Mg in 1 M NaOH solution. At voltages below 3 V, the current was relatively low, and a light grey film of  $\text{Mg}(\text{OH})_2$  was formed. At 3–20 V, a thick dark film of  $\text{Mg}(\text{OH})_2$ , along with oxygen gas, was formed, and finally, a thin protective coating was again produced at voltages above 20 V. However, above 50 V, the formation of anodic film was locally limited by the breakdown phenomenon accompanied by localized sparking. A similar anodizing behavior was seen by Yaniv et al. (1968), Zengnan et al. (1989), and Takaya (1989) [74]. Moreover, Ono et al. found that the porous film develops above the breakdown potential in alkaline fluoride solution [75,76]. The breakdown potential varies from 50 V to above 110 V with the type of alloy and electrolyte.

Clapp et al. have demonstrated that the growth of anodic film on the Mg involves the initial formation of oxide barrier layer, followed by the film breakdown, and finally the formation of porous oxide layer [77]. Moreover, Carter et al. have given one possible explanation for the film breakdown [78]. At constant applied current, the potential response increases linearly with anodizing time to reach around 70 V as a thin barrier film grew on the Mg surface. When the barrier film reached a critical thickness of around 80 nm, the potential abruptly dropped to a relatively low value of around 10 V. Then, the potential began to rise again linearly, until another sharp drop was encountered. This pattern repeated for a number of cycles, and therefore, the potential showed a saw-tooth pattern with anodizing time. The intermittent, abrupt drop of potential is attributed to the breakdown of barrier film, forming a porous anodic film. This breakdown triggered by the tensile stress in the barrier film, which has a smaller molar volume as compared to the metallic Mg.

Magoxid is a newly developed hard anodizing process in 1998 [79]. In this process, a barrier layer of anodic film locally destroyed at high potentials ( $> 100$  V) by injection of a large number of charged particles. A rapid charge transfer and diffusion of metal ions release extra energy that is high enough to start the plasma chemical reaction (particularly, in electrical discharge) at the Mg surface/gas/electrolyte interface. The discharge channels produced between the gas/electrolyte interface (quasi-cathode) and the Mg surface (anode). This kind of arcing creates plasma like condition by the ionization of oxygen, and oxidizes and melts the surface of Mg. Moreover, areas close to the discharge channels spontaneously activated by heat. Hence, a large number of anodes produced partially on the entire surface. In consequence, the whole Mg surface can be converted into Mg oxide. One major advantage with the use of Magoxid process is that it has high throwing power, so that Mg components can be anodized properly from all sides with only small dimensional changes.

### 2.1.3.5. Oxygen Evolution during Anodizing

Oxygen evolution reaction at the anode (Mg surface) is also an important phenomenon to be considered during the anodizing. This electrochemical reaction proceeds as  $4\text{OH}^- \rightarrow 2\text{H}_2\text{O} + \text{O}_2 + 4\text{e}^-$ . The oxygen evolution, associated with electric current, seems to closely relate to the appearance of spark discharges. When the sparking occurs during anodizing,

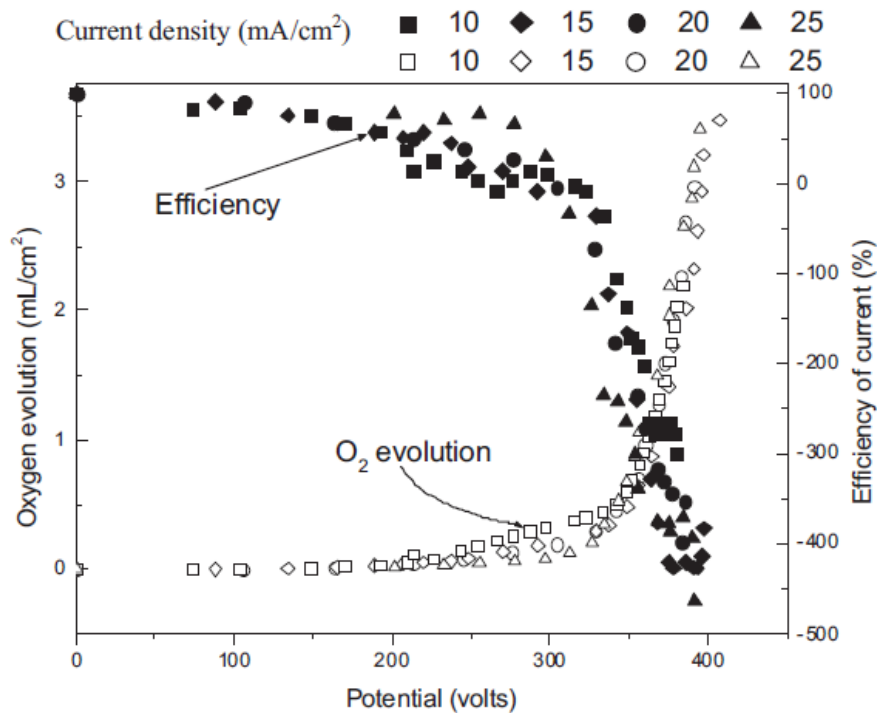


Fig. 2.15. Oxygen evolution and current efficiency during anodization under constant electric charge ( $18 \text{ C cm}^{-2}$ ) [80]. The negative efficiency could be attributed to the thermal decomposition of water during anodizing. For more detail discussion, please refer to the ref. 80.

vigorous oxygen evolution is commonly observed. The trapping of the oxygen bubbles during the growth of anodic film could be responsible for the extensive porosity. On the other hand, without any sparking, relatively insignificant oxygen evolves. Recently, Shi et al. reported the relationship between oxygen evolution and anodizing efficiency for AZ91D during anodizing in a silicate containing solution [80]. They first make an assumption that the anodizing current has contributed to both reactions of film formation and oxygen evolution. As a consequence of this assumption, a drastic decrease in anodizing efficiency up to a negative value (–) was measured after sparking, increasing the rate of oxygen evolution reaction accompanied by sparking, as shown in Fig. 2.15. The oxygen evolution during sparking may result from thermo-decomposition of water at the sparking points. This can explain the unusual negative anodizing efficiency.

#### 2.1.4. Structure of Anodic Film

The anodized coatings of Mg are generally characterized by a multilayer structure.

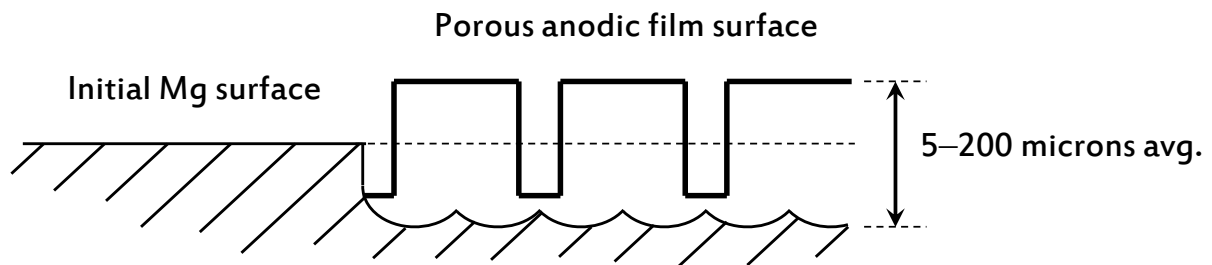


Fig. 2.16. Schematic diagram for the formation of porous anodic film on the magnesium surface.

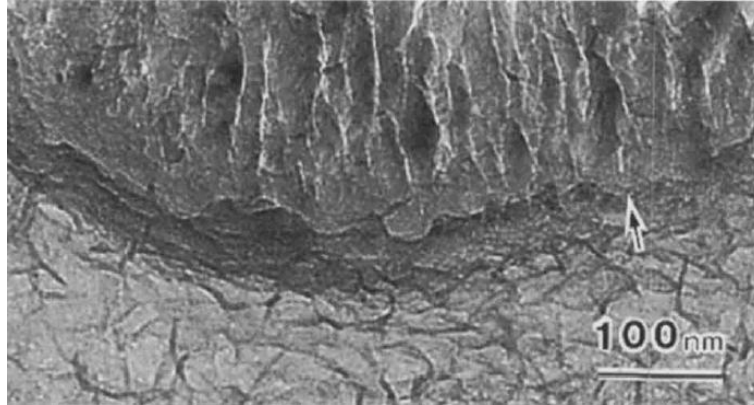


Fig. 2.17. TEM cross section of the anodic film formed on pure magnesium during Dow 17 process. Arrow shows the barrier layer connected to the metal substrate under the cylindrical layer [86].

Adjacent to the substrate is a very thin nonporous anodic barrier layer, followed by an intermediate layer with low to moderate porosity. On the other hand, the outer layer of anodic film is much more porous. In Fig. 2.16, the unanodized Mg surface is shown on the left, and a magnified schematic diagram of the anodized surface on the right. This figure illustrates that how an anodic film grows out of the Mg surface, partially above and partially below the original surface level. In the Magoxid process, the anodic film grows about 50 % into the original surface and 50 % above the original surface level [81]. This anodic oxide layer is usually around one hundredth of a centimeter thick (from 5 to 200 microns). The anodic film is very difficult to make thicker than that because the oxide is non-conductive. Therefore, the formation of anodic film stops when the electrical path through the base Mg from the electrolyte is disconnected.



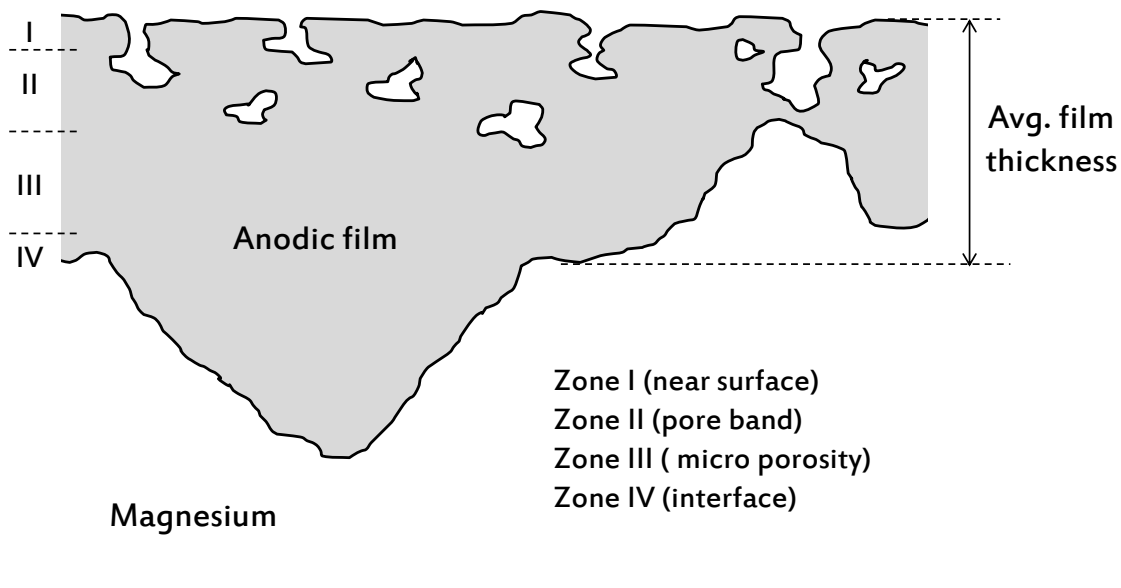


Fig. 2.18. Schematic diagram of a typical cross section found for the hard ceramic oxide coatings [85].

In the Magoxid process, the anodic film consists of three layers, which comprised a thin barrier layer adjacent to the substrate, a middle ceramic non-porous oxide layer, and an outermost layer with highly ordered porous ceramic oxide [82,83]. The middle main coating would provide almost the whole corrosion protection. The similar structure was found for Keronite coating which has about 35  $\mu\text{m}$  thick oxides. [84]. Moreover, Blawert et al. have produced thicker anodic film (around 120  $\mu\text{m}$ ) which exhibits a similar structure [85]. In Dow 17, the barrier layer connected to the Mg substrate under the cylindrical pores was clearly observed, as shown in Fig. 2.17 [86]. As shown in Fig. 2.18, there is porosity throughout the entire anodic film structure. However, four different layers could be identified according to the porosity [85]:

Zone 1 (near surface): This is the uppermost layer comprised of many craters on top. The formation of ceramic oxide is enforced by a large number of discharge channels reaching from the crater surface towards the zone 2.

Zone 2 (pore band): This can be identified by a remarkable band of cavities in 20-40  $\mu\text{m}$  depth from the surface. The visible surface craters, i.e. the surface pores, seem to end in this band of cavities.

Zone 3 (micro porosity): This has an extension from 20  $\mu\text{m}$  to 80  $\mu\text{m}$  with anodizing time. The anodic film formed is denser, and only a small number of cavities or large-diameter-pores are visible.

Zone 4 (interface): This is very rough. It appears as a very thin layer of less than 1  $\mu\text{m}$  thick with a finer and denser structure.

The most striking feature of the anodic films on the Mg is its pore structure. Shi et al. reported irregular and anisotropic distribution of micrometer pores in their anodized coatings [87], and that is in good agreement with other reports. The size and distribution of pore structure strongly affect the mechanical and corrosion characteristic of Mg products. However, during the anodizing process, the creation of the pore structure in the anodized coating cannot be prevented, thus some degree of porosity will be created. Hence, emphasis needs to be placed on reducing the porosity as small as possible and forming the oxide layer uniformly. Otherwise, there are two basic ways to make use of porosity, i.e. the outer porous layer can be impregnated or grinded away to expose the denser underlying coating [88]. In general, it is known that a coating layer comprised of single-phase is better than that of multi-phase because of fitting mismatch, stresses, different chemical potentials etc. [89].

## 2.1.5. Corrosion behavior of Anodic Film

### 2.1.5.1. Effect of Substrate

The same anodic films on different type of Mg alloys show different morphology and subsequent corrosion performance [90,91]. In ref. 92, the effect of Al content and the amount of  $\beta$ -phase in the Mg-Al alloys on the anodizing process was investigated, and found that the Al content is beneficial for the surface passivation of anodized coating. Moreover, Kotler showed that, on different alloys of AZ31B and AZ91, the corrosion resistance of same anodic film is to certain extent depends on the substrate [93]. The  $\beta$ -phase plays an important role in the corrosion performance of Mg alloy substrates. However, an anodic film formed on  $\beta$ -phase contains a lot of tiny pores and large elongated defects, while that formed on  $\alpha$ -phase is more continuous and smoother with fewer pores. Therefore, the anodic films become coarser in the areas around the boundaries of  $\alpha$ -phase and  $\beta$ -phase. Nevertheless, the corrosion resistance of formed anodic films strongly depends on that of Mg alloy substrates. Overall, the poor corrosion performance of an anodic film is responsible partly for its higher porosity and/or partly for lower corrosion resistance of substrate used [87].

Shi et al. have investigated the effect of Zn content on the corrosion resistance of anodic film formed on the Mg-Zn alloys [94]. The corrosion tests in 5 wt.% NaCl for 30 hrs showed that the order of the corrosion rate of alloys and the anodic films was Mg 0.5 Zn > Mg 1 Zn > Mg 2 Zn [94]. For the same type of alloy, the content of impurities, such as Cu, Fe, and Ni, can determine the corrosion resistance of anodic film formed on them. A primary HP AZ91 alloy coated with Magoxid-Coat exhibited a better corrosion resistance than a low purity AZ91 with the same coating [95].

### 2.1.5.2. Effect of porosity

The anodic film of Mg alloys plays two basic roles in preventing corrosion. First, the anodic film separates the Mg substrate surface from the surrounding corrosive environments. In general, it has a higher corrosion resistance than the substrate so that the lifetime can be increased. Second, the anodic film is less or typically more an insulator with high dielectric strength, allowing the current flow with other metals to reduce. This can provide a better protection against contact corrosion.

In order to adequately explain the time-dependent corrosion performance of Mg alloys before and after anodizing, the characteristic of the porous anodic films should be considered. In general, the anodic films formed on Mg alloys can be divided into two sub-layers: a very thin but dense inner layer and thick porous outer layer [72,96]. For the outer layer, defects such as pores always exist as a result of the metallurgical phase separations, geometry of

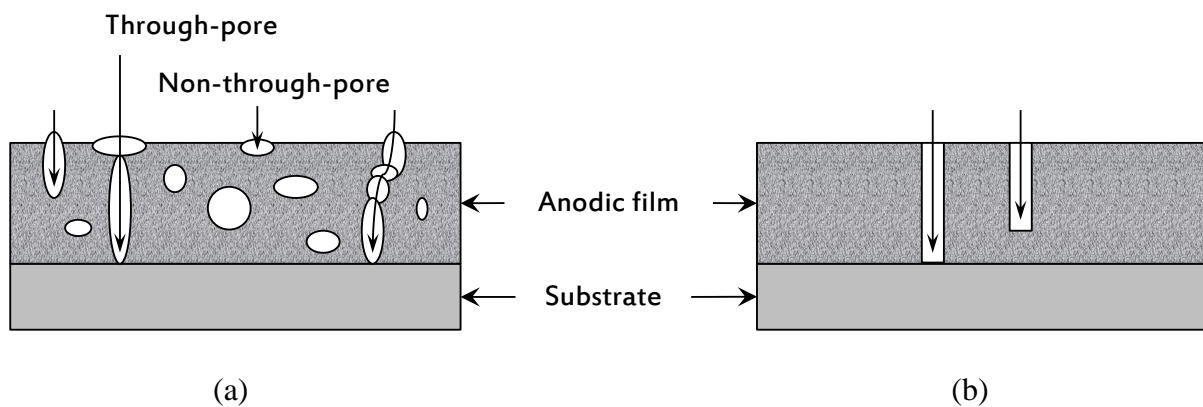


Fig. 2.19. Schematic diagrams of (a) non-through-pores and through-pores formed in an anodic film on magnesium and (b) the simplified microstructure of the anodic film [87].

original surface, sparking process, and various anodizing parameters (electrolyte, concentration, temperature, electric field applied, etc.). The formation of compact anodic films on Mg alloys is limited, because MgO has a molar volume of  $11.3 \text{ cm}^3 \text{ mol}^{-1}$ , whereas metallic Mg has a molar volume of  $14.0 \text{ cm}^3 \text{ mol}^{-1}$ , and therefore the Pilling-Bedworth ratio is 0.81. In this context, several researchers have elucidated the mechanism for the corrosion of the anodic film through the two types of pores, i.e. the non-through-pores and through-pores [72,97]. In addition, many researchers have examined the causal relationship between the microstructure (such as the sizes and distribution of pores) and electrochemical characteristics of anodized Mg alloys [98–100]. As shown in Fig. 2.19, if there are some through-pores in the anodic film which allows the corrosive media to easily reach the substrate, the corrosion of the anodized Mg alloys might be determined by the corrosion resistance of the substrate at the bottoms of the through-pores. In this context, Blawert et al. have argued that the defect density is the dominating influence rather than the film thickness [72]. Thus, the pore characteristics of the anodic film are fundamental consideration in the accurate evaluation of the corrosion performance of anodic films.

Hence, the open-pore structures of anodic films on Mg alloys need to be sealed or be coated with other protective coatings to give adequate corrosion resistance for a longer period in a more corrosive environment. Although the various anodizing methods result in different anodic films, there is a clear agreement on the need for the top layer.

### **2.1.6. Dyeing and Impregnation**

Figure 2.20 shows an anodic film after dyeing treatment. Remember that a film has a hundredth of one centimeter thick. Even if the pigment elements were finely ground, the

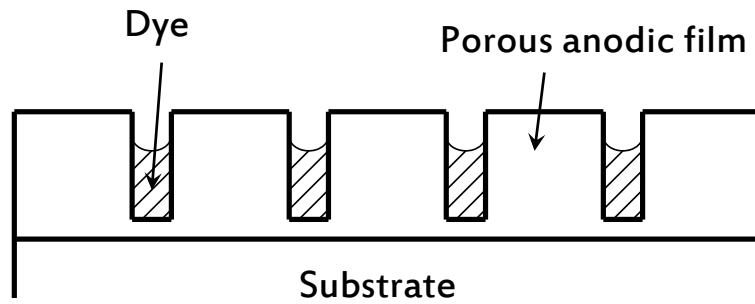


Fig. 2.20. Schematic diagram of an anodic film after dyeing treatment.

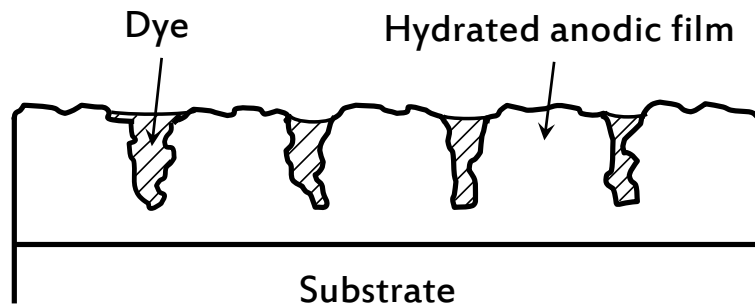


Fig. 2.21. Schematic diagram of an anodic film with dye after impregnation treatment in boiling water.

liquid dye cannot sufficiently fill the surface pores. However, during the impregnating post-treatment in boiling clean water for a few minutes, the anodic film reacts with the boiling water and swells with the formation of small nodular oxide. These nodular oxides can effectively trap the pigment grains of dye in the pores. In Fig. 2.21, we can see the anodic film sealed to grab the pigments. This is very similar with gravels held in a cement slab.

### 2.1.7. Surface Sealing

Surface sealing technique is to develop a thin, extremely water impermeable coating on appropriately treated enough alloy surfaces [105]. It should not be confused with the impregnation technique to seal porosity described in chapter 2.1.6. For suitable surface sealing of anodized Mg alloys, Magnesium Elektron has been developed below formulation [105].

Araldite HZ985 Hardener	100 parts by weight
Araldite PZ985 Resin	300 parts by weight
Ethyl Acetate	240 parts by weight
Toluene	136 parts by weight
Diacetone Alcohol	24 parts by weight

This resin can satisfactorily seal the surface pores and is extremely resistant to most chemicals. The coating procedure is as follows [105]:

1. Pre-heat at 200–220 °C for 30 min or until this temperature has been maintained for at least 10 min (to ensure the surface moisture is completely removed).
2. Cool to 60 °C, then dip in, or spray with, the sealing resin.
3. Air dry for 15–30 min (Ensure uniform drainage and remove any tears with a brush).
4. Bake at 200–220 °C for 10–15 min.
5. Remove drips and tears with a sharp knife or glass paper (Be careful of damaging underlying film)

Table. 2.2. Corrosion resistance of some anodic films during salt spray tests [62–64].

Coating procedure	Corrosion appearing time (h)
AZ HP untreated	0 – 10
AZ91 HP + Magoxid (MC) 25 $\mu\text{m}$	80 – 100
AZ91 HP + MC + sealing water glass	250 – 300
AZ91 HP + MC + sealing silane	430 – 600
AZ91 HP + MC + EP-powder paint 60–80 $\mu\text{m}$	750 – 1000
AZ91 HP + MC + silane + EP-powder paint 60–80 $\mu\text{m}$	1000

6. Repeat steps 2, 3, 4, and 5 twice more to make 3 coats in all.

7. Bake final coat to manufacturer's recommended temperature for 45–60 min (total thickness of resin is approximately 0.025 mm)

For Anomag coating on AZ91 alloy, the porous anodic film, mainly consisted of  $\text{Mg}_3(\text{PO}_4)_2$ , formed with 10–25  $\mu\text{m}$  thick. The presence of this anodic film can reduce the surface general corrosion well. However, the most effective protection against the surface general corrosion is obtained after the sealing or painting treatments. In ref. 101, the corrosion rate was reduced by approximately 97%. They did not affect the composition of the anodic film. Further, only with the sealing and painting procedures, effective protection against the galvanic corrosion was obtained. After 240 hrs of salt-spray test, the steel bolt was



corroded with a form of red rust over the surface, while the galvanic corrosion on the sealed anodic film of AZ91 (20–25  $\mu\text{m}$  in thickness) was completely suppressed [101]. The “only Anomag coating” produced a pore size of around 6  $\mu\text{m}$  and a porosity of around 13%. However, the combination of sealing and painting reduced the pore size 2-folds and the porosity by 3-folds [101].

By several researchers, Magoxid coatings with and without different post-sealing treatments were produced [102–104], and their corrosion resistances are directly compared in Table 2.2 [72]. The result of salt-spray tests shows that a powder painting with 60–80  $\mu\text{m}$  thick was adequate for preventing surface corrosion attacks.

## 2-2. Research Background and objective

The anodic films formed on Mg alloys can be divided into two sub-layers: a very thin but dense inner layer and thick porous outer layer [4,8]. The formation of compact anodic films on Mg alloys is limited, because MgO has a molar volume of  $11.3 \text{ cm}^3 \text{ mol}^{-1}$ , whereas metallic Mg has a molar volume of  $14.0 \text{ cm}^3 \text{ mol}^{-1}$ , and therefore the Pilling-Bedworth ratio is 0.81 [4,21]. In this context, several researchers have elucidated the mechanism for the corrosion of the anodic film through the two types of pores, i.e., the non-through-pores and through-pores [22,23]. In addition, many researchers have examined the causal relationship between the microstructure (such as the sizes and distribution of pores) and electrochemical characteristics of anodized Mg alloys [24–26]. Thus, the pore characteristics of the anodic film are fundamental consideration in the accurate evaluation of the corrosion performance of anodic films. Such a porous film will allow corrosive media to reach the substrate alloy easily; it will not offer any protection and will instead accelerate galvanic and general corrosion. Moreover, spongy nature of this film may reduce its adhesion with the substrate.

In this paper, we describe a novel anodizing technique that significantly limits the formation of micro-pores on the anodic films and thereby increases the corrosion resistance. The process involves applying the pulse potential specifically between anodic oxidation and active regions of AZ31 Mg alloy in 2 M NaOH alkaline solution at 303 K. Note that passive metals such as Fe, Cr, Ni with transpassive dissolution are not appropriate for corrosion protection by anodization. Similarly, the passivity of Mg breaks down at about  $2 V_{\text{Ag}/\text{AgCl}}$  with high transpassive dissolution rate of various  $\text{A cm}^{-2}$  in 2 M NaOH. However, the transpassive dissolution stops abruptly at the extended transpassive range, i.e. anodic oxidation range, which is higher than  $6 V_{\text{Ag}/\text{AgCl}}$  up to hundreds of volts. This property was used to develop

oxide films of Mg alloys for corrosion protection. The main idea of this pulse anodization is that the active potential may remove the weak spots on the anodic film through the potential edge effect and thereby increase the concentration of reactant species near the electrode/electrolyte interface. Moreover, we investigate the feasibility of sealing the porous structure of an as-anodized AZ31 Mg alloy with a stannate post-treatment and measure the resultant corrosion characteristics.

## REFERENCES

- [1] J.L. Murray, In Binary alloy phase diagrams, T.B. Massalski (ed.), 2nd ed., Ohio, ASM International, v.1 (1990) p.169.
- [2] J.B. Clark, L. Zabdry, and Z. Moser, In Binary alloy phase diagrams, T.B. Massalski (ed.), 2nd ed., Ohio, ASM International, v.3 (1990) p.2571.
- [3] A.A. Nayeb-Hashemi, J.B. Clark, In Binary alloy phase diagrams, T.B. Massalski (ed.), 2nd ed., Ohio, ASM International, v.3 (1990) p.2520.
- [4] J.E. Gray, B. Luan, *J. Alloys Compd.* 336 (2002) 88.
- [5] X. Chen, Ph.D. Dissertation, The Ohio State University, Columbus, Ohio, USA, 2010.
- [6] O. Lunder, K. Nisancioglu, and R.S. Hansen, SAE Technical Paper Series #930755, Detroit, 1993.
- [7] C.E. Nelson, *Trans. AIME* 159 (1944) 392.
- [8] G.L. Makar, K. Kruger, *J. Electrochem. Soc.* 137 (1990) 414.
- [9] K. Nisancioglu, O. Lunder, and T.K. Aune, *Proc. of 47th World Magnesium Association*, Mcleen, Virginia (1990) p.43.
- [10] C.B. Baliga, P. Tsakiroopoulos, *Mater. Sci. Technol.* 9 (1993) 513.
- [11] J.E. Hillis, S.O. Shook, SAE Technical Paper Series #890205, Detroit, 1989.
- [12] E.F. Emley, "Principles of Magnesium Technology", Pergamon Press, New York, 1966.
- [13] J.E. Hillis, SAE Technical Paper #830523, Detroit, 1983.
- [14] J.D. Hanawalt, C.E. Nelson, and J.A. Peloubet, *Trans. AIME* 147 (1942) 273.
- [15] W.S. Loose, "Corrosion and Protection of Magnesium" (Eds: L. M. Pidgeon, J. C. Mathes, N. E. Woldmen), ASM Int., Materials Park, OH 1946, pp. 173-260.
- [16] H.A. Robinson, P.F. George, *Corrosion* 10 (1954) 182.

- [17] O. Lunder, T.K. Aune, and K. Nisancioglu, *Corros. Sci.* 43 (1987) 291.
- [18] G.L. Makar, J. Kruger, *J. Electrochem. Soc.* 137 (1990) 414.
- [19] A. Srinivasan, S. Ningshen, U. KamachiMudali, U.T.S. Pillai, and B.C. Pai, *Intermetallics* 15 (2007) 1511.
- [20] J. Polmear, "Magnesium and magnesium alloys," in *ASM Specialty Handbook*, M. M. Avedesian and H. Baker, Eds., p. 14, ASM International, Materials Park, Ohio, USA, 1999.
- [21] I.P. Moreno, T.K. Nandy, J.W. Jones, J.E. Allison, and T.M. Pollock, *Scr. Mater.* 48 (2003) 1029.
- [22] F. Khomamizadeh, B. Nami, and S. Khoshkhouei, *Metall. Mater. Trans. A* 36 (2005) 3489.
- [23] C.F. Chang, S.K. Das, and D. Raybould, "Rapidly Solidified Mg-Al-Zn-rare Earth Alloys", ASM, Metals Park, OH, 1985, p.129.
- [24] B.S. You, W.W. Park, and I.S. Chung, *Scripta Mater.* 42 (2000) 1089.
- [25] A. Suzuki, N.D. Saddock, J.W. Jones, and T.M. Pollock, *Acta Mater.* 53 (2005) 2823.
- [26] R. Ninomira, T. Ojiro, and K. Kubota, *Acta Metall. Mater.* 43 (1995) 669.
- [27] Y. Terada, N. Ishimatsu, Y. Mori, and T. Sato, *Mater. Trans.* 46 (2005) 145.
- [28] M. Hakamada, A. Watazu, N. Saito, and H. Iwasaki, *Mater. Sci. Eng., A* 527 (2010) 7143.
- [29] G.L. Makar, J. Kruger, *Int. Mater. Rev.* 38 (1993) 38.
- [30] K.N. Reichek, K.J. Clark, and J.E. Hillis, SAE Technical Paper Number 850417, 1985.
- [31] William. E. II. Mercer, James. E. Hillis, SAE Technical Paper Series #920073, Detroit 1992.
- [32] E.F. Emley, "Principles of Magnesium Technology", Pergamon Press, Oxford, 1966.
- [33] G.L. Makar, J. Kruger, *Int. Mater. Rev.* 38 (1993) 138.

- [34] K.U. Kainer, Magnesium-Eigenschaften, Anwendungen, Potentiale, Wiley-VCH Verlag GmbH, Weinheim, 2000.
- [35] R.S. Hanson, Review of corrosion behavior of Mg alloys, In: BL Mordike, F. Hehmann, ed. Magnesium alloys and their applications, Oberursel: Informationgesellschaft-Verlag, (1992) p.327.
- [36] G.L. Song, A. Atrens, Adv. Eng. Mater. 1 (1999) 11.
- [37] G. Song, A. Atrens, Adv. Eng. Mater. 5 (2003) 837.
- [38] O. Kunder, K. Nisancioglu, and R.S. Hanses, SAE Technical Paper Series, No. 930755, 1993.
- [39] Katarzyna N. Braszczynska-Malik, Precipitates of  $\gamma$ -Mg<sub>17</sub>Al<sub>12</sub> phase in AZ91 alloy, (ed. F. Czerwinski), InTech, 2011.
- [40] G.S. Frankel, A. Samaniego, N Birbilis, Corros. Sci. 70 (2013) 104.
- [41] A. Atrens, W. Dietzel, Adv. Eng. Mater. 9 (2007) 292.
- [42] G. Song, A. Atrens, D. St John, X. Wu, and J. Nairn, Corros. Sci. 39 (1997) 1981.
- [43] Z.M. Shi, J.X. Jia, and A. Atrens, Corros. Sci. 60 (2012) 296.
- [44] G.S. Frankel, "Techniques for corrosion quantification", in: E.N. Kaufmann (Ed.), Characterization of Materials, second ed., Wiley VCH, NY, 2012.
- [45] A. Atrens, W. Dietzel, Adv. Eng. Mater. 9 (2007) 292.
- [46] G. Song, A. Atrens, D. St John, X. Wu, and J. Nairn, Corros. Sci. 39 (1997) 1981.
- [47] G. Song, A. Atrens, D. Stjohn, J. Nairn, and Y. Li, Corros. Sci. 39 (1997) 855.
- [48] S. Bender, J. Goellner, and A. Atrens, Adv. Eng. Mater. 10 (2008) 583.
- [49] S. Bender, J. Goellner, A. Heyn, and S. Schmigalla, Mater. Corros. – Werkstoffe Korros. 63 (2012) 707.
- [50] R.L. Petty, A.W. Davidson, and J. Kleinberg, J. Am. Chem. Soc. 76 (1954) 363.

- [51] J.O.M. Bockris, A.K.N. Reddy, "Modern Electrochemistry", second ed., Kluwer Academic/Plenum Publishing, New York, 2000.
- [52] J. E. Gray, B. Luan, *J. Alloys Compd.* 336 (2002) 88.
- [53] F. Czerwinski, *Acta Mater.* 50 (2002) 2639.
- [54] Jose L. Gazapo, J. Gea, "Anodizing of Aluminium", European Aluminium Association, 1994.
- [55] J. Zhang, C. Wu, *Recent Patents on Corros. Sci.* 2 (2010) 55.
- [56] O. Khaselev, D. Weiss, and J. Yahalom, *J. Electrochem. Soc.* 146 (1999) 1757.
- [57] J. Edwards, "Coating and Surface Treatment Systems for Metals: a comprehensive guide to selection", ASM International, 1997, pp.39-40.
- [58] Z. Su, "porous anodic metal oxides", Ph.D. Dissertation, University of St Andrews, Scotland, United Kingdom, 2010.
- [59] <http://corrosion-doctors.org/Electrochemistry-of-Corrosion/Cathodic-processes.htm>
- [60] Y.I. Choi, S. Salman, K. Kuroda, M. Okido, *Corros. Sci.* 63 (2012) 5.
- [61] J.S. Kim, R.H. Song, and S.I. Pyun, *J. Met. Finish. Soc. Kor.* 21 (1988) 19.
- [62] Anne Deacon Juhl, "Theoretical introduction to pulse anodizing", <http://www.aluconsult.dk/artikler/Paper%20-%20AAC%20september.pdf>, online at January 21, 2008.
- [63] A.D. Juhl, Ph.D. thesis, Pulse anodizing of extruded, cast aluminium alloys, Inst. of Manufacturing Engineering, The Technical University of Denmark (1999).
- [64] J.G. Qian, C. Wang, D. Li, G.L. Guo, and G.L. Song, *Trans. Nonferrous Met. Soc. China* 18 (2008) 19.
- [65] H. Duan, C. Yan, and F. Wang, *Electrochim. Acta* 52 (2007) 3785.
- [66] X. Liu, T. Zhang, Y. Shao, G. Meng, and F. Wang, *Corros. Sci.* 51 (2009) 1772.

- [67] M. Pourbaix, Atlas D'Equilibres Electrochimiques, Gauthier-Villars Cie (1963)
- [68] <http://www.saltlakemetals.com/SolubilityProducts.htm>
- [69] G.G. Perrault, J. Electroanal. Chem. Interfacial Electrochem. 51 (1974) 107.
- [70] G. Song, A. Atrens, Adv. Eng. Mater. 5 (2003) 837.
- [71] M.P. Staiger, A.M. Pietak, J. Huadmai, and G. Dias, Biomaterials 27 (2006) 1728.
- [72] C. Blawert, W. Dietzel, E. Ghali, and G. Song, Adv. Eng. Mater. 8 (2006) 511.
- [73] K. Huber, J. Electrochem. Soc. 100 (1953) 376.
- [74] M. Takaya, Aluminium 65 (1989) 1244.
- [75] S. Ono, N. Masuko, Mater. Sci. Forum 419–422 (2003) 897.
- [76] S. Ono, H. Kijima, and N. Masuko, Mater. Trans. 44 (2003) 539.
- [77] C. Clapp, P.A. Kilmartin, and G.A. Wright, Corrosion & Prevention-2000; Australasian Corrosion Association (2001) 5.
- [78] E.A. Carter, T.F. Barton, and G.A. Wright, Surface treatment 99: 4<sup>th</sup> International Conference on Computer Methods and Experimental Measurements for Surface Treatment Effects, Assisi, Italy, 20–22, Sept. (1999) p.169.
- [79] P. Kurze, Mat.–Wiss. Werkstofftech. 29 (1998) 85.
- [80] Z. Shi, G. Song, and A. Atrens, Corros. Sci. 48 (2006) 1939.
- [81] P. Kurze, D. Banerjee, Gießerei-Praxis No. 11/12 (1996) 211.
- [82] P. Kurze, D. Banerye, and H. J. Kletze, (1995) US 5385662.
- [83] P. Kurze, H. J. Kletze, (1996) US 5487825.
- [84] S. Shrestha, A. Sturgeon, P. Shashkov, and A. Shatrov, Magnesium Technology 2002, Seattle, WA, 17-21 February 2002, TMS (2002) 283.
- [85] C. Blawert, V. Heitmann, W. Dietzel, H. M. Nykyforchyn, and M. D. Klapkiv, Surf. Coat. Technol. 200 (2005) 68.



- [86] S. Ono, K. Asami, T. Osaka, and N. Masuko, *J. Electrochem. Soc.* 143 (1996) L62.
- [87] Z. Shi, G. Song, and A. Atrens, *Corros. Sci.* 47 (2005) 2760.
- [88] A. Von Kuhn, *Galvanotechnik* 5 (2003) 1114.
- [89] Homepage: Technol. Appl. Group, Inc. at <http://www.tagnite.com/>.
- [90] O. Khaselev, J. Yahalom, *J. Electrochem. Soc.* 145 (1998) 190.
- [91] A.J. Zozulin, D.E. Bartak, *Met. Finish.* 92 (1994) 39.
- [92] O. Khaselev, J. Yahalom, *Corros. Sci.* 40 (1998) 1149.
- [93] G.R. Kotler, D.L. Hawke, E.N. Aqua, SDEC-77: 9<sup>th</sup> SDEC Int. Die Cast. Exposition and Congress 9 (1977) G-T77-022.
- [94] Z. Shi, G. Song, A. Atrens, *Proc. of the 1st Int. Light Met. Technol. Conf. 2003*, 18-20 September, 2003, Brisbane, Australia, A. Dahle, ed., 408 pages, CAST Publisher, 2003, 393.
- [95] B. Olbertz, *Jahrbuch Oberflächentechnik* 45 (1989) 262.
- [96] J. Zhang, C. Wu, *Corros. Sci.* 5 (2010) 55.
- [97] H. Ardelean, I. Frateur, S. Zanna, A. Atrens, and P. Marcus, *Corros. Sci.* 51 (2009) 3030.
- [98] V. Tchervyakov, G. Gao, J. Bomback, A.P. Pchel'nikov and G. Cole, *Magnesium Technology 2000*, p.143, TMS (2000).
- [99] R.F. Zhang, D.Y. Shan, R.S. Chen, and E.H. Han, *Mater. Chem. Phys.* 107 (2008) 356.
- [100] C. Blawert, V. Heitmann, W. Dietzel, H.M. Nykyforchyn, and M.D. Klakiv, *Surf. Coat. Technol.* 200 (2005) 68.
- [101] V. Tchervyakov, G. Gao, J. Bomback, A.P. Pchel'nikov, and G. Cole, *Magn. Technol. 2000*, TMS (2000) 143.
- [102] P. Kurze, *Berichtsband, 23. Ulmer Gespräch*, 2001, 82.
- [103] F. Hayduk, P. Kurze, *Magn. 2000, Proc. of the Second Isr. Int. Conf. on Magn. Sci. &*

Technol., 22-24.2. 2000, Dead Sea, Israel 2000, 431.

[104] F. Leyendecker, Conf., Dt. Forschungsges. f. Oberflächenbehandlung, Dt. Ges. f. Galvano- u. Oberflächentech. DGO, Münster, D, 13.–14. Mar, 2001, Berichtsband DFO, Band 46 (2001) Seite 132–142, Düsseldorf: Deutsche Forschungsges. f. Oberflächenbehandlung (DFO).

[105] “Surface Treatments for Magnesium Alloys in Aerospace & Defence”, Magnesium Elektron UK, P.O. Box 23, Rake Lane, Swinton, Manchester, M27 8DD, England.000

**III. Temperature dependence of passivity  
breakdown on Mg-Al alloys in NaCl solution**

### 3-1. Introduction

Magnesium and its alloys have been favored as lightweight solutions in automobile and aerospace industries during past few decades. They are the lightest of all useful structured metal alloys, and therefore, are an excellent choice for engineering applications that demand critical weight design considerations. However, Mg is a very active metal, and tends to form a surface layer of corrosion products such as hydroxides and oxides, when in direct contact with water or air. The corrosion susceptibility of Mg alloys depends on the stability of such corrosion products. In particular, the presence of  $\text{Cl}^-$  degrades their stability in aqueous solutions compared to Al alloys and steels. Only under ideal theoretical condition is the corrosion of Mg alloy limited, especially in places that are not exposed to environments containing  $\text{H}_2\text{O}$  and  $\text{Cl}^-$ . Therefore, under real time conditions, Mg alloys are used as chassis, interiors, and power train, e.g. brake/clutch bracket assemblies, seat bases/risers, ABS housing, steering wheels, and almost all sorts of brackets and housings, wherein corrosion of Mg alloys is avoidable [1].

Consequently, recent research efforts on the development and applications of new Mg alloys have focused on possible ways to decrease their surface corrosion. Al is the principal alloying element for various Mg alloys, when alloyed from 4% up to 10%, significantly impedes the surface corrosion of Mg in active environments. Therefore, the corrosion of Mg alloys is typically affected by the amount and distribution of intermetallic phases, e.g.  $\text{Mg}_{17}\text{Al}_{12}$  ( $\beta$ -phase). In this context, several studies have analyzed the effects of Al content and the corresponding microstructure on the corrosion behavior of Mg alloys [2–9]. In general, increasing the Al content normally decreases the corrosion susceptibility of Mg alloys. However, some studies have recently reported a contradictory corrosion behavior in

Mg-Al type Mg alloys [6–9]. These results act as direct experimental evidences for the theoretical prediction that the  $\beta$ -phase either behave as a barrier for the corrosion or act as a micro-galvanic cathode. This indicates that the corrosion of Mg alloys has a strong dependence on their morphology and microstructure. An increase in the area fraction of  $\beta$ -phase, or in other terms, a decrease in  $\alpha/\beta$ -phase ratio, gradually leads this phase to act as a micro-galvanic cathode to  $\alpha$ -matrix [9]. On the other hand, the  $\beta$ -phase, which is in a finely and continuously-dispersed state, acts as a barrier layer for surface degradation [5]. Meanwhile, some authors have claimed that the formation of small and intergranular precipitates of  $\beta$ -phase results in a rapid galvanic corrosion between  $\alpha$ -matrix and  $\beta$ -phase [10]. This implies that, even for the same alloy composition, different processing methods can result in Mg alloys with different microstructures, leading to the contradictory corrosion behaviors [8,11]. Nevertheless, the effect of Al content and the corresponding specific corrosion mechanism of Mg alloy still remain ambiguous.

Thus far, several mechanisms, including competitive ion adsorption (between  $\text{Cl}^-$  and passivating agent) or surface complex ion formation theories [12–14], ion penetration theory [15,16], mechano-chemical theory [17], and point defect model [18], have been proposed to elucidate the breakdown action of passive films in an aqueous solution containing  $\text{Cl}^-$ . Although the abovementioned film breakdown models utilize slightly different sets of resources, it is commonly recognized that the film breakdown occurs above a critical breakdown potential, known as pitting potential, at highly localized sites, depending on the temperature, chloride concentration, and applied anodic overpotential.

In this study, we have investigated the effect of electrolyte temperature on the electrochemical properties of three different Mg alloys, namely, AZ31B, AZ61, and AZ91. In addition, we have also demonstrated the contradicting corrosion behavior between AZ61 and

AZ91 at high electrolyte temperature. We believe that the results obtained in this study will provide guidelines for the manufacturing methods adopted for processing Mg alloys.

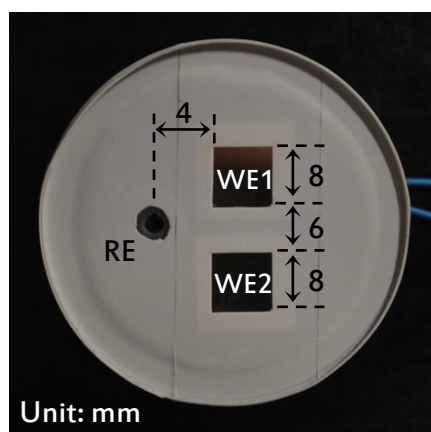
## 3-2. Experimental

Table 3.1 summarizes the chemical compositions of the different AZ-type Mg alloys (wrought AZ31B, AZ61, and as-cast AZ91) used as test coupons in this study. The Mg alloy sheets were ground up to 2000 grit by using a fine-grained emery paper, ultrasonically cleaned for 3 min in ethanol, and then quickly dried in cool air. The working area of each coupon ( $1 \times 1 \text{ cm}^2$ ) was limited with hydrophobic adhesive masking tape.

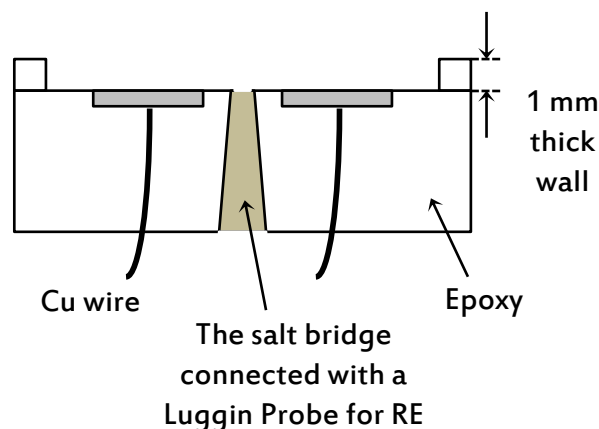
The corrosion characteristics of the Mg alloys were assessed by means of potentiodynamic tests, electrochemical impedance spectroscopy (EIS), and potentiostatic tests in 0.1 M NaCl aqueous solution in the temperature range of 298–328 K (25–55 °C). The potentiodynamic tests were carried out in a potential ranging from  $-1$  to  $+1$  V vs. open circuit potential  $E_{\text{OCP}}$  after stabilizing  $E_{\text{OCP}}$  for 30 min. The corresponding currents were recorded at

Table 3.1. Chemical compositions (wt.%) of the different Mg alloys, namely, AZ31B, AZ61, and AZ91.

	Al	Zn	Mn	Fe	Si	Cu	Ni	Mg
AZ31B	3.29	0.75	0.30	0.03	< 0.01	< 0.01	< 0.01	Bal.
AZ61	5.91	1.16	0.21	< 0.01	0.04	0.04	< 0.01	Bal.
AZ91	9.00	0.70	0.24	< 0.01	0.04	< 0.01	< 0.001	Bal.



Cell photograph



Cross-sectional configuration

Fig. 3.1. Photograph and schematic of the electrochemical cell, employing two identical working electrodes, used for corrosion monitoring during cyclic corrosion tests. The WE1 and WE2 connect the working electrode and counter electrode of potentiostat, respectively.

scan rate set to  $1 \text{ mV s}^{-1}$ .

For the EIS measurements, the real and imaginary components of the electrochemical cell was evaluated over a frequency range of  $10^5$  to  $10^{-2}$  Hz with a amplitude of 10 mV, where the applied potential was  $-1.38 \text{ V}_{\text{Ag}/\text{AgCl}}$  and  $E_{\text{OCP}}$ , respectively. The EIS measurements at the  $E_{\text{OCP}}$  were carried out after an initial open circuit delay of 30 min, and those at  $-1.38 \text{ V}_{\text{Ag}/\text{AgCl}}$  (anodic domain) were carried out immediately after immersion, for all temperatures. We could expect that, from these experiments, the comparison between the corrosion behavior under natural and accelerated conditions. The electrochemical cells were fabricated by using Mg alloy sheets as the working electrode (WE), a platinum wire as the counter electrode (CE), and Ag/AgCl reference electrode (with saturated KCl) as the reference electrode (RE).



Table 3.2. Details of the condition adopted during the cyclic corrosion test (T = operating temperature, RH = relative humidity). During salt-spray step, the high concentration of salt (5 wt.%) was used in order to ensure comparability within 24 hrs of the tests.

Operating cycles	Conditions of each step
Salt spray (2 h)	5 wt.% NaCl, T: 35 °C, RH: 100%
Dry (4 h)	T: 60 °C, RH: 25%
Wet (2 h)	T: 50 °C, RH: 100%

Figure 3.1 shows the photograph and schematic of the 3-electrode electrochemical cell designed for monitoring the corrosion behavior of Mg alloys in a chamber during the cyclic corrosion tests (CCT). This cell is essentially a modification of the setup reported in previous studies in refs. 19, 20. Although the cyclic corrosion testing conditions are very severe for Mg corrosion, it was carried out to simulate adequately complex service conditions usually found in the field.

The cell was constructed by embedding two identical Mg alloys (WEs) in parallel in epoxy at a distance of 6 mm apart, with the RE placed at the center, in between the WEs. Note that it is highly important to maintain electrical contact between these WEs and RE during the entire CCT measurements, especially for the dry stage. When a localized corrosion occurs on one WE at a given test environment, excess electrons flow toward the other WE to cathodically protect its surface [20]. At this moment, the current difference between the two

WEs and their mixed potential can be measured by connecting a zero resistance ammeter (ZRA) and a potentiostat. The details of operating cycles and the conditions for each setup of the CCT are described in [Table 3.2](#).

Furthermore, the microstructure of the test specimens was examined by using scanning electron microscopy (SEM). For this, AZ61 and AZ91 were etched for approximately 5 s with 5% Nital (5 mL HNO<sub>3</sub> + 95 mL ethanol) to observe the general constituents [\[6\]](#).

### 3-3. Results and discussion

#### 3.3.1. Effect on polarization behavior

Potentiodynamic tests were carried out to predict the temperature-dependent probability of corrosion of AZ31B, AZ61, and AZ91 in 0.1 M NaCl solution, in the temperature range of 25–55 °C. The hydrogen evolution during polarization times under both anodic and cathodic conditions has a complicated effect on the corrosion behavior of Mg alloys. The hydrogen evolution proceeds as  $2\text{H}_2\text{O} + 2\text{e}^- \rightarrow \text{H}_2 + 2\text{OH}^-$ . The hydroxyl ions ( $\text{OH}^-$ ) during this reaction increase the pH of the electrolyte, which leads to unexpected decrease in the corrosion susceptibility of Mg alloys during anodic polarization time. Moreover, an interesting observation associated with this reaction is that a rate of hydrogen evolution increases with the anodic polarization [21,22]. Therefore, the potentiodynamic tests are performed with two identical surfaces of the same sample, separately in potential ranges of  $E_{\text{OCP}}$  to +1 V (anodically) and then from  $E_{\text{OCP}}$  to –1 V (cathodically).

As evidenced from the results of potentiodynamic tests shown in Fig. 3.2a and 3.2b, both the corrosion potential ( $E_{\text{corr}}$ ) and the corrosion current density ( $i_{\text{corr}}$ ) decrease with increase in Al content increased, at nearly room temperatures. Considering the mixed potential theory and the experimental results obtained, this could be attributed not only to the initial rapid corrosion resulting from the formation of a micro-galvanic cell between  $\alpha/\beta$ -phases, but also to the decrease in cathodic reduction reaction rates, with the increase in Al content. An increase in the Al content decreases the cathodic reaction rate, leading to lower values of  $i_{\text{corr}}$  at nearly room temperatures. This in turn implies a lower corrosion rate. During long term immersion times, the  $\text{Al}_2\text{O}_3/\text{Al}(\text{OH})_3$  compounds originating from the  $\beta$ -phase also

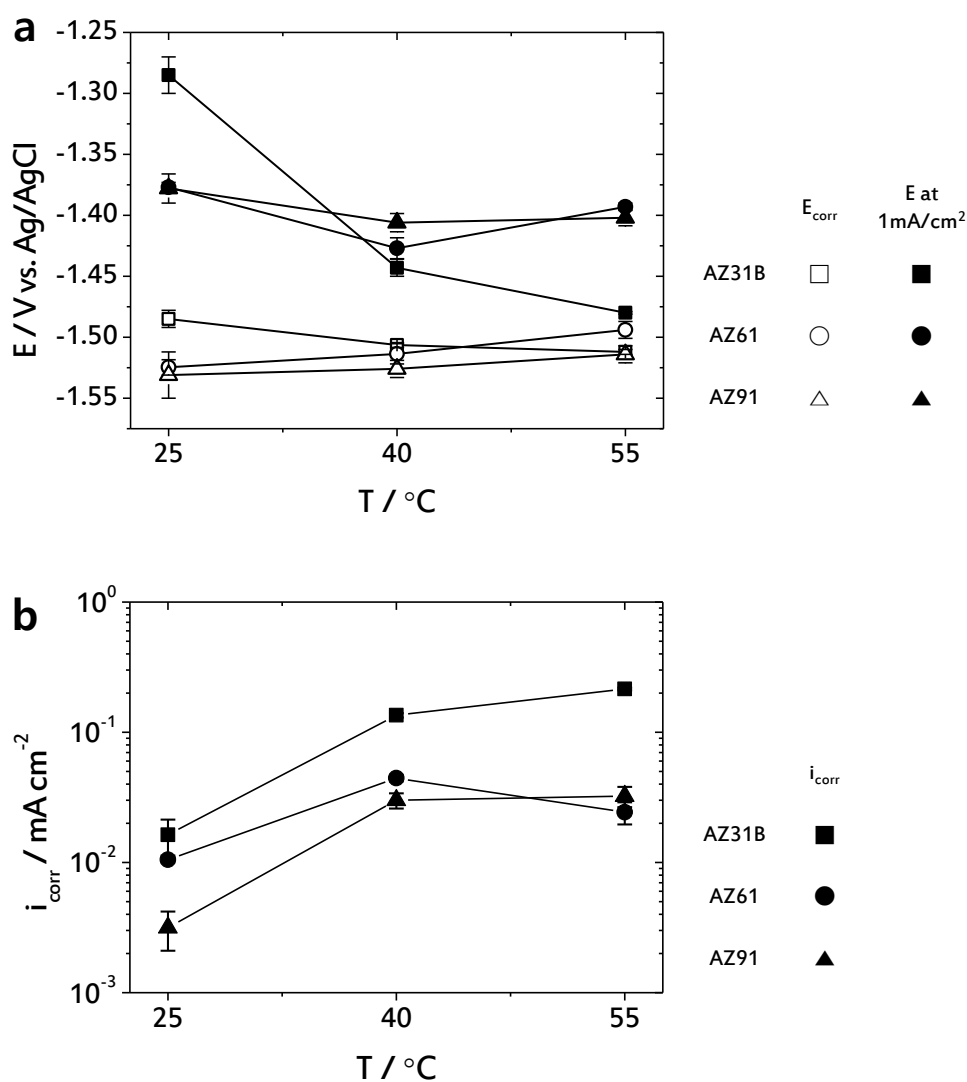
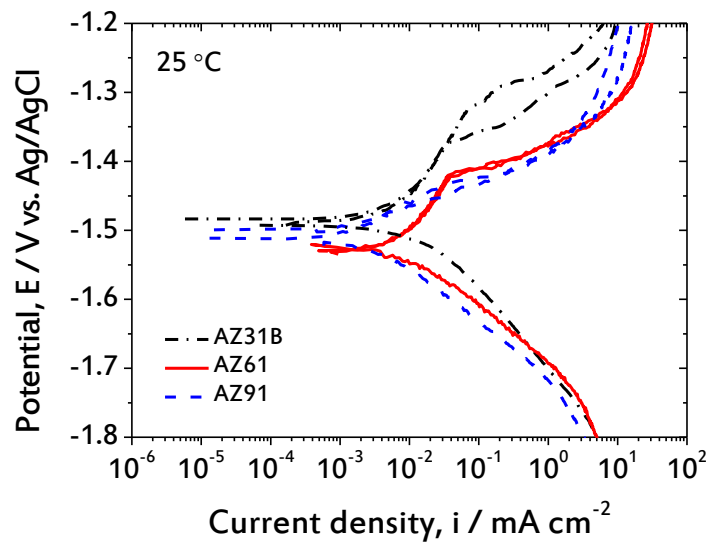
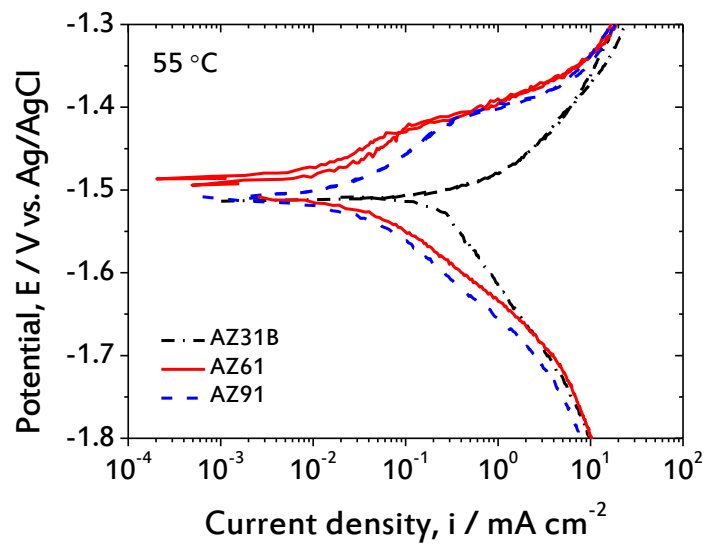


Fig. 3.2. Variation in (a) corrosion potential  $E_{\text{corr}}$  and potential at  $1 \text{ mA cm}^{-2}$ , and (b) corrosion current density  $i_{\text{corr}}$  of AZ31B, AZ61, and AZ91 as functions of electrolyte temperature in 0.1 M NaCl, as estimated from potentiodynamic tests. The  $i_{\text{corr}}$  was estimated by the extrapolation of cathodic Tafel slopes back to the  $E_{\text{corr}}$ . The potential values at  $1 \text{ mA cm}^{-2}$  are presented in Fig. 3.2a to explain polarization phenomenon. The intersection corresponds to the  $i_{\text{corr}}$ . Error bars represent standard deviations. Smaller deviation than the symbols show no error bar.



(a)



(b)

Fig. 3.3. Anodic and cathodic polarization behaviors of electrodes AZ31B, AZ61, and AZ91 with electrolyte temperature in 0.1 M NaCl.

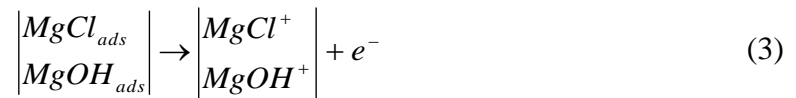
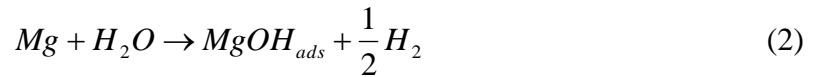
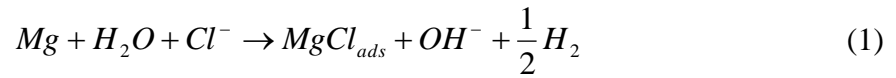
effectively impede the surface corrosion of AZ61 and AZ91. The lack of reproducibility of  $E_{\text{corr}}$  measurement for AZ91 might be attributed to the variation of the amount and distribution of  $\beta$ -phase depending on the location of plates.

The  $E_{\text{corr}}$  of AZ61 and AZ91 gradually increase with the electrolyte temperature due to the increase in charge transfer. On the other hand,  $E_{\text{corr}}$  of AZ31B rapidly decreases with electrolyte temperature, although the charge transfer increases at high temperatures. This could have resulted from the severe increase in corrosion kinetics with a high uniform corrosion, as shown in Fig. 3.3. No passivation phenomena could be observed in AZ31B at 55 °C. Considering that all the experiments were performed after the initial open circuit delay of 30 min, the  $\beta$ -phase seems to act as a barrier for preventing further corrosion, after the superficial active  $\alpha$ -matrix is all corroded. Between the alloys AZ61 and AZ91, no significant difference in the charge transfer kinetics could be observed, at all temperature ranges considered in this study. However, in case of AZ61, the rate of increase in the  $E_{\text{corr}}$  with electrolyte temperature is remarkable, when compared to that of AZ91. This could be explained based on the strengthening of surface passivation associated with the  $\beta$ -phase. The alloy AZ61 has a lower passivation current density than AZ91, while their pitting potentials  $E_{\text{pit}}$  exhibit similar values (Fig. 3.3). Moreover, for AZ61, 1 mA cm<sup>-2</sup> reached without serious anodic polarization, when compared to AZ91 (Fig. 3.2a). In consequence, the  $i_{\text{corr}}$  value of the AZ61 rather decreases at 55 °C, resulting in the lowest corrosion rate. Our results show that the reproducibility of anodic polarization behavior is quite good, contrary to those performing both anodic and cathodic polarizations sequentially.

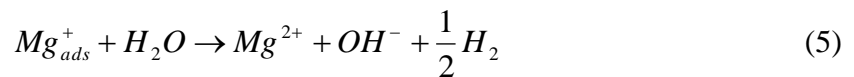
### 3.3.2. Effect on electrochemical impedance behavior

As shown in Fig. 3.4, the impedance diagrams of the Mg alloys polarized at  $-1.38$   $V_{Ag/AgCl}$  (anodic domain) afford only one well-defined capacitive loop over the high frequency domain, corresponding to a maximum value of imaginary part. Moreover, we could also observe the onset of two or three inductive loops, extended by the capacitive loop over low frequencies. The origin of the inductive loops in this electrolyte is actually related to both the absorption of  $Cl^-$  and  $H_2O$ , and the process of direct anodic dissolution on oxide-free surfaces of the Mg alloys, as follows:

(i) adsorption of  $Cl^-$  and  $H_2O$



(ii) direct anodic dissolution [23]



The adsorbed species of  $MgCl_{ads}$ ,  $MgOH_{ads}$  and  $Mg_{ads}^+$  shown in the reactions (1–3) are thermodynamically unstable. Consequently, they easily undergo dissolution to form

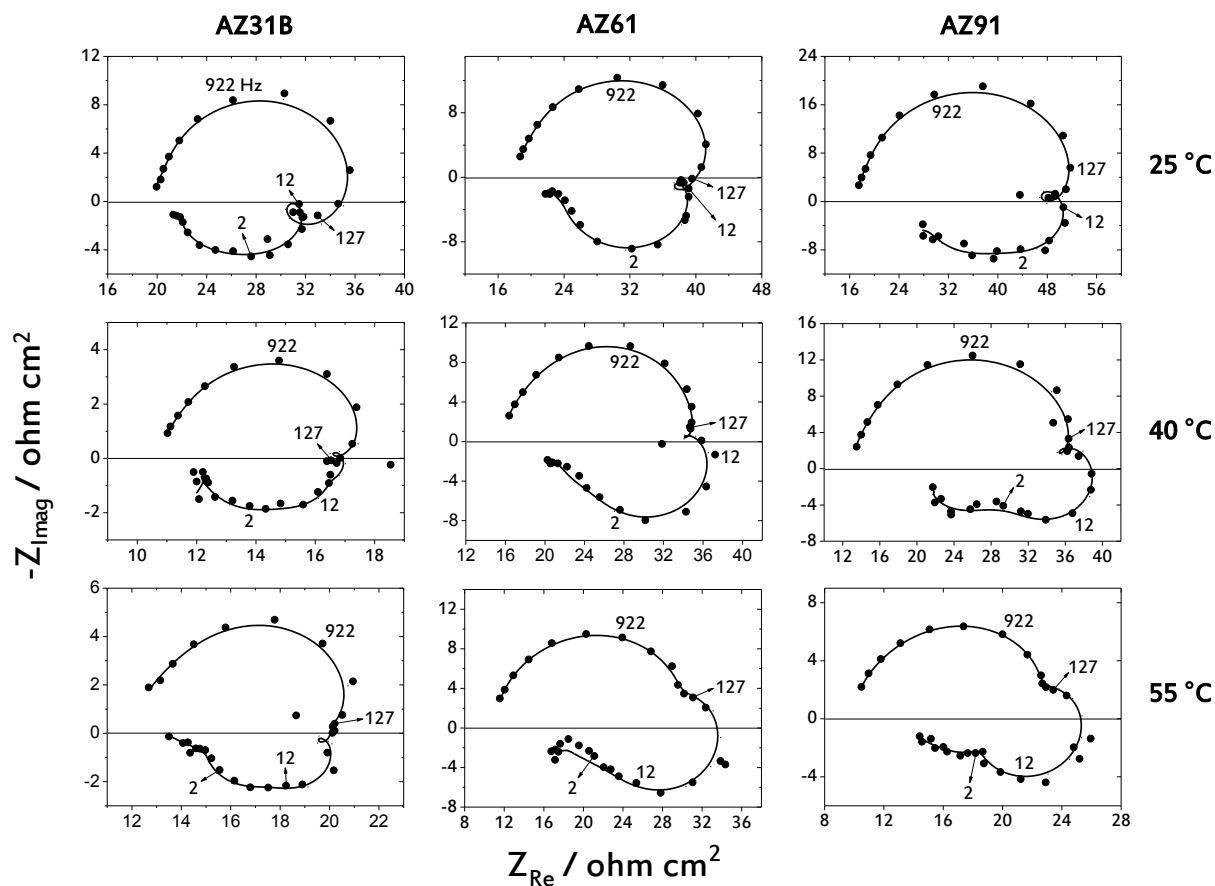


Fig. 3.4. Nyquist plots of AZ31B, AZ61, and AZ91 measured at applied potential of  $-1.38 V_{Ag/AgCl}$  as a function of electrolyte temperature, immediately after immersion in 0.1 M NaCl. The experimental impedance data ( $\bullet$ ) are Kramers-Kronig relation compliant ( $—$ ), indicating that these processes fulfill causality, linearity, stability, and finiteness. For detailed explanation for the Kramers-Kronig relation, refer to the [ref. 32](#).

$MgCl^+$ ,  $MgOH^+$  and  $Mg^{2+}$ , according to the reactions (3) and (5), respectively. The electrochemical reactions (1), (2), and (5) are introduced to explain the severe hydrogen generation reaction that occurs during the impedance measurement, i.e. negative difference effect. The oxide-free areas, at which the reactions (1–5) may take place, are considered to be



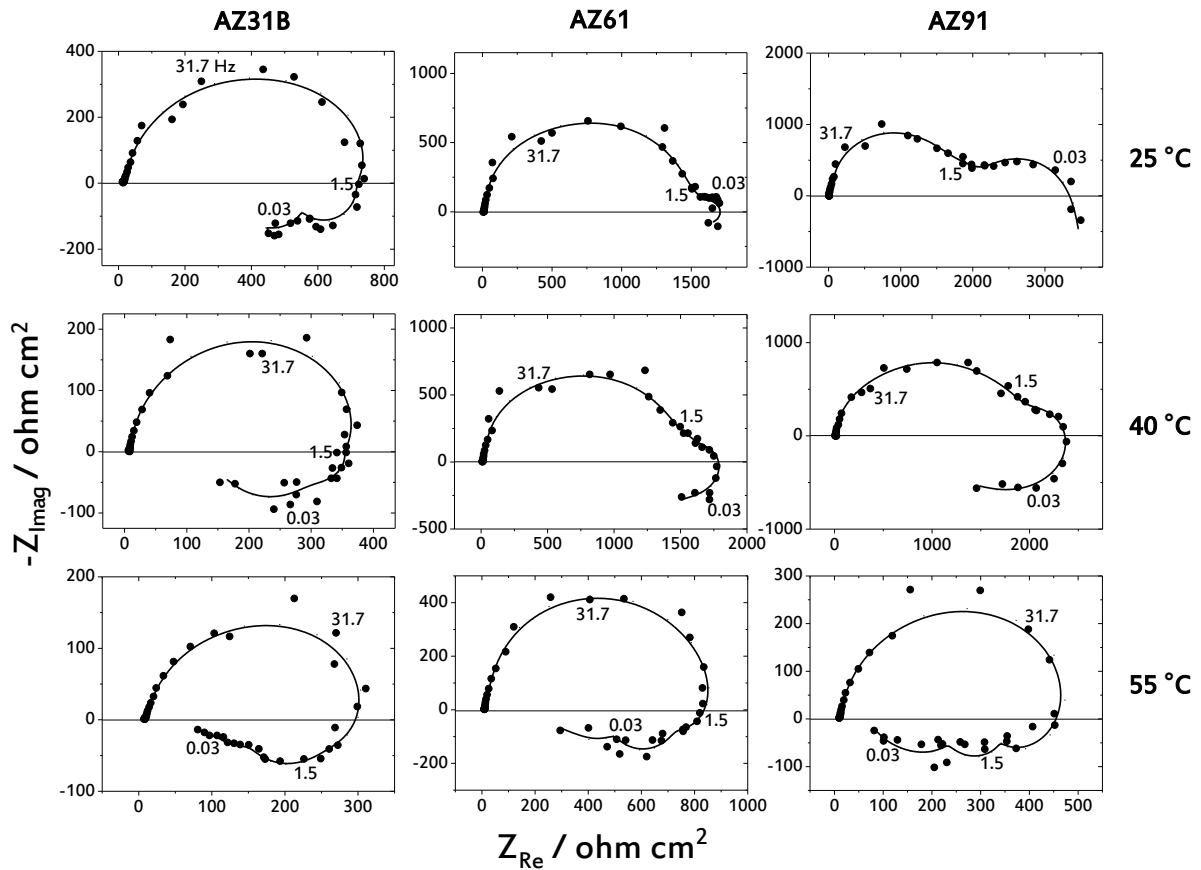


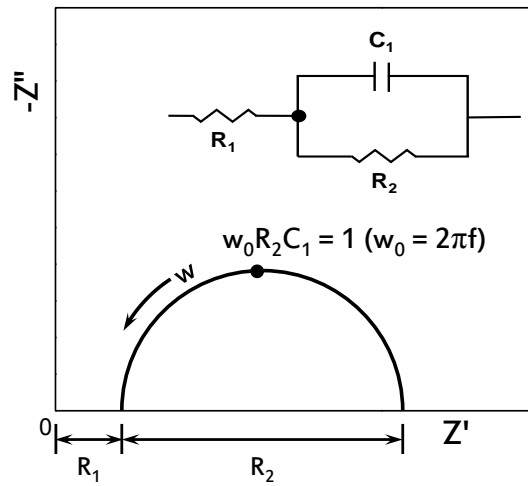
Fig. 3.5. Nyquist plots of AZ31B, AZ61, and AZ91 measured at open-circuit potential as a function of electrolyte temperature, after immersion for 30 min in 0.1 M NaCl. The experimental impedance data ( $\bullet$ ) are Kramers-Kronig relation compliant ( $—$ ), indicating that these processes fulfill causality, linearity, stability, and finiteness. For detailed explanation for the Kramers-Kronig relation, refer to the [ref. 32](#).

different for each specimen, depending on the area fraction difference of  $\beta$ -phase. In other words, the presence of  $\alpha$  and  $\beta$  phases and their interactions may dynamically enlarge the oxide-free area of Mg surface, accelerating the corrosion rate. In this context, the corrosion kinetics of each specimen corresponding to the oxide-free area can be defined with the

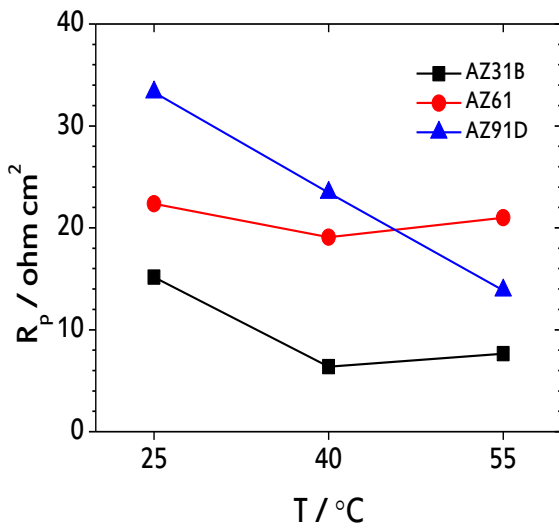
polarization resistance  $R_p$ .

The Nyquist plot for the alloy AZ31B at 55 °C shows inductive loops. The presence of 3 time-constants has been reported by other researchers at high anodic overpotentials and even in a strongly corrosive media [23,24], which represents the high dissolution reaction rate of Mg electrode. For the same reason, the severest relaxation of coverage is seen on the entire surface of AZ31B, along with the evolution of a large amount of hydrogen at 55 °C. Finally, after the impedance measurements, the alloy AZ31B gets damaged by the rapid corrosion and loses its bright appearance. On the other hand, the alloys AZ61 and AZ91 show only two inductive loops, even at 55 °C, Also, the surfaces are mildly damaged with few pits, without much lose in their brightness. Interestingly, at temperatures higher than 40 °C, some part of the inductive loop transforms into a capacitive loop, corresponding to the pre-passivation process [23]. This results in an increase in  $R_p$ . Considering that the passivation phenomenon appears only as the capacitive loop in the impedance diagram, this transformation seems to indicate that the oxide-free area (mainly  $\alpha$ -Mg) that prompts continuous dissolution gradually vanishes, thereby increasing the surface coverage at the high temperatures. In other words, the partial transformation of inductive loop into capacitive loop might imply a manifestation of the corrosion barrier effect of  $\beta$ -phase.

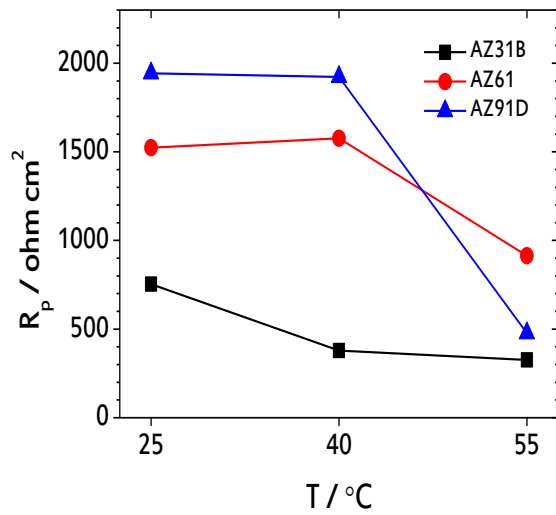
Remarkably, the  $R_p$ , i.e. sum of all resistances, of AZ61 maintained at almost a constant value with increase in electrolyte temperature up to 55 °C, as shown in Fig. 3.6(b). On the other hand, the  $R_p$  of AZ91 gradually decreases with increase in electrolyte temperature. Finally, AZ61 affords rather higher  $R_p$  (21.0  $\Omega$  cm<sup>2</sup>) than AZ91 (13.9  $\Omega$  cm<sup>2</sup>) at 55 °C, indicating that the degradation of AZ61 under such a state with high kinetic energy is relatively impeded. In case of AZ91, the observed gradual decrease in  $R_p$  with electrolyte temperature might have resulted from the film breakdown and subsequent corrosion over the



(a)



(b)



(c)

Fig. 3.6. Variation of polarization resistance  $R_p$ , i.e. sum of all resistance, at (b)  $-1.38 \text{ V}_{\text{Ag}/\text{AgCl}}$ , (c) open-circuit potential as a function of electrolyte temperature  $T$ , estimated from Fig. 3.4 and Fig. 3.5, respectively. The typical equivalent circuit models consisting of  $m$  series connected Voigt elements ( $-R-(RC)_m-$ ) without inductance element were used for curve fitting (Fig. 3.6a).

entire surface of the electrode during the anodic polarization.

These experimental results are definitely consistent with those of impedance measurements at  $E_{\text{OCP}}$  after prior immersion for 30 min. As shown in Fig. 3.5, for all the electrodes, the frequency value, at which the imaginary component reaches a maximum  $W_{\text{max}}$ , moved to a high frequency domain, with increase in electrolyte temperature. It could be due to the increased degradation rates. This is similar to the impedance results at  $-1.38 \text{ V}_{\text{Ag/AgCl}}$ . Of the 3 different alloys considered in this study, AZ61 exhibits the slowest increasing rate of  $W_{\text{max}}$ , and resulting in the lowest value of  $W_{\text{max}}$  at 55 °C. This represents the lowest double layer capacitance ( $C_{\text{dl}}$ ) per unit area, which is parallel with  $R_p$  [25]. Therefore, as shown in Fig. 3.6(c), AZ61 exhibits rather higher  $R_p$  ( $914 \Omega \text{ cm}^2$ ) when compared to AZ91 ( $477 \Omega \text{ cm}^2$ ) at 55 °C. For both AZ61 and AZ91 at 25–40 °C, the inflection point that follows the high frequency capacitive loop has a characteristic frequency of approximately 1.5 Hz, which is not affected by the electrolyte temperature. These low frequency capacitive loops are attributed to the formation of oxide aggregates during the immersion, according to the ref. 26.

However, an increase in electrolyte temperature leads to decrease in both the high and low frequency capacitive loops. Some part of the low frequency capacitive loop is transformed to inductive loops, which is accompanied by a decrease in  $R_p$ . The expansion of the inductive loop can be explained based on the relaxation of surface coverage due to the adsorption of  $\text{MgCl}_{\text{ads}}$  and  $\text{MgOH}_{\text{ads}}$  species [23]. In case of AZ61 at 55 °C, the first inductive loop occurs at a relatively lower frequency when compared to AZ91, and exhibits higher value of  $R_p$ . In addition, the rapid emergence of inductive loop also leads to an increase in the number of inductive loops in AZ91, representing a high degradation rate of the electrode surface.

### 3.3.3. Effect on current transient behavior

Potentiostatic tests were carried out to analyze quantitatively the kinetics of pitting corrosion in Mg alloys with electrolyte temperature. A strict control of the formation of passive film took precedence over the tests. After the tests, many pits were observed for all Mg alloy surfaces considered in this study, excluding AZ31B at 55 °C, which indicates that the current transients are mainly responsible for the pitting process. A rapid arrival to critical current values (within 200 s) may explain why the pitting corrosion of Mg propagates through only a few corrosion sites per unit area of exposed surface.

As shown in Fig. 3.7, we could observe a continuous increase of pitting current with no incubation time  $t_i$  when the coupons were polarized at an applied constant potential  $E_{app}$  of  $-1.38 \text{ V}_{Ag/AgCl}$ , the value of which is higher than their critical breakdown potential  $E_c$ . Instead, the  $t_i$  was dominated by the transient time  $\tau$ . In most cases, the passive film breakdown occurs more easily above  $E_c$  in the presence of  $\text{Cl}^-$  anions and results in a local exposure of oxide-free area to the corrosive environment. Therefore, a large value of  $\Delta E$  ( $= E_{app} - E_c$ ) leads to the convergence of  $t_i$  to zero, according to the following equation [27]:

$$t_i = \zeta \left\{ \exp\left(-\frac{xF\alpha\Delta E}{2RT}\right) \right\} \quad (6)$$

where  $\zeta$  is  $J^0 u^{-\frac{x}{2}} (a_{\text{Cl}^-})^{\frac{x}{2}} \exp\left(\frac{xF\alpha V_c}{2RT}\right)$ ,  $F$  is Faraday's constant,  $RT$  is the thermal energy.

This equation well describes that  $t_i$  is a function of  $\Delta E$  in an electrolyte, where the  $\text{Cl}^-$  concentration is fixed (constant  $a_{\text{Cl}^-}$ ). The results imply that  $\Delta E$  is quite large for Mg alloys, so that the experimental condition might be considerably aggressive to corrosion. Hence, the

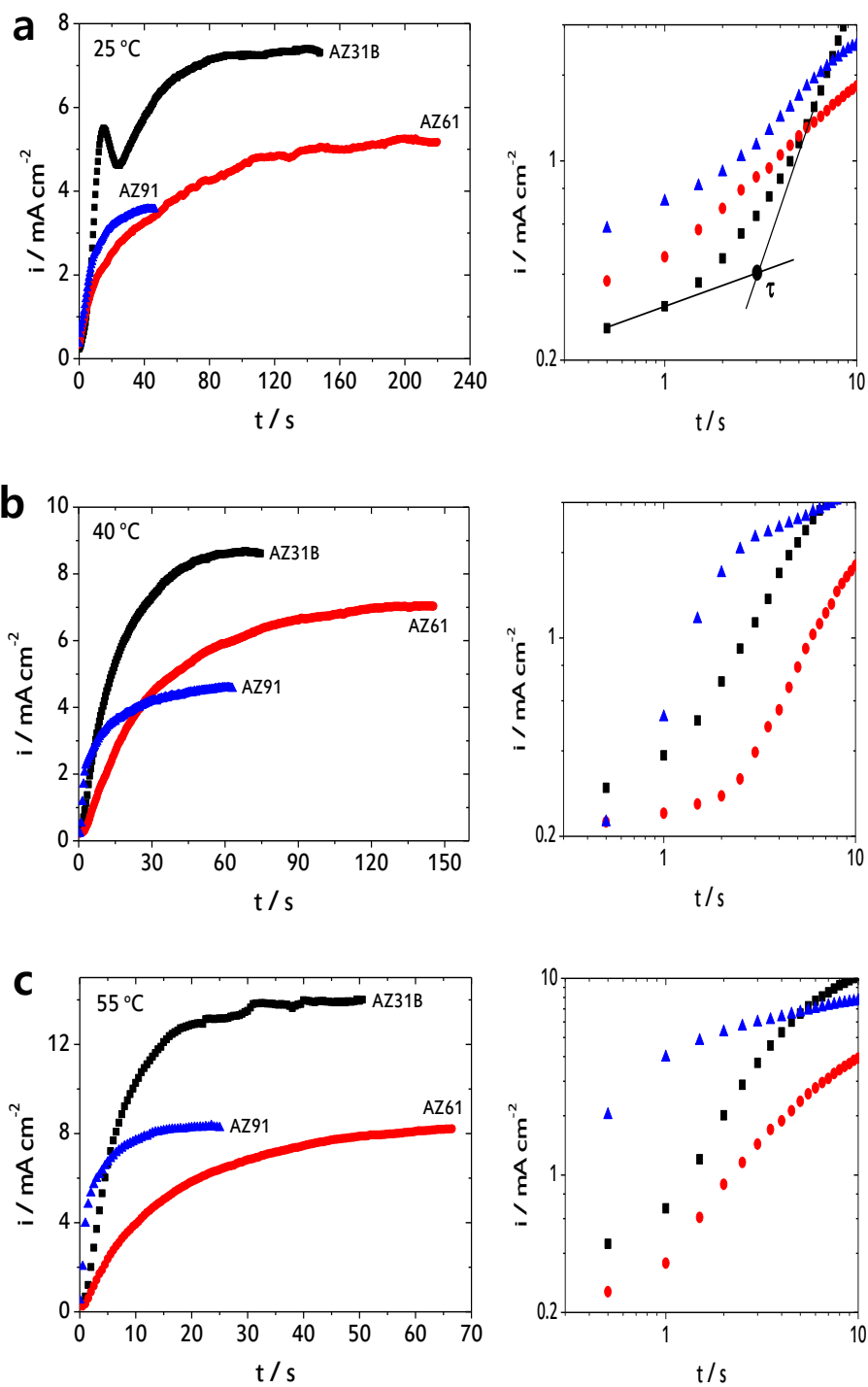


Fig. 3.7. Corrosion current transients  $i$  as a function of electrolyte temperature through the alloys AZ31B, AZ61, and AZ91 at  $-1.38 \text{ V}_{\text{Ag}/\text{AgCl}}$  in  $0.1 \text{ M NaCl}$ .

pitting current began to rise sharply with time, reaching the maximum value of current density  $i_{\max}$  within few minutes, with the onset of visible pits. Obviously, the lowest value of  $i_{\max}$  was observed in case of AZ91 at nearly room temperatures (25, 40 °C). However, at 55°C, an inverse relationship emerged between AZ61 and AZ91. Moreover, AZ61 shows rather lower (or very similar)  $i_{\max}$  compared to AZ91. Noticeably, the pitting current of AZ61 increased at the slowest pace with time (i.e. lowest slope) for all the temperature ranges considered in this study. This indicates that the interaction between Mg and  $\text{Cl}^-$  is the slowest among them. This slow change in current was predominant, especially at higher temperature (55 °C). Only for AZ31B, there was always a transition with a slow fall in current density during initial period (around 20 s) at 25 °C.

In the  $\log i$  vs.  $t$  curves inserted, the parameter  $\tau$  represents an inflection point between the two straight lines with different slopes. The corresponding time is  $\tau$ . The first approximation can be expressed as  $i = kt$ , immediately followed by an exponential increase of  $i$  with time according to the relation  $i = kt^b$ , where  $k$  and  $b$  are constants that depend on  $E_{\text{app}}$  and  $\Delta E$ . Here,  $\tau$  is regarded as an important parameter for the interpretation of passive film breakdown kinetics, accounting for the transient diffusion flux during anodic polarization at  $E_{\text{app}}$ , which is remarkable than that of steady-state diffusion. In this context, the convergence of  $\tau$  to almost zero with electrolyte temperature indicates that the rate of passive film breakdown is more severe in AZ91 than in AZ61 at high temperatures ( $1/\tau \propto$  an approximate estimate of film breakdown rate). Moreover, AZ61 mostly exhibits lower transient currents than AZ91, although the parameter  $b$  seems to be very similar. This implies that the interaction between AZ61 and  $\text{Cl}^-$  is a slow process, which might be due to the presence of strongly bonded adsorbed species on the electrode surface. The distinctly growing difference in transient currents with electrolyte temperature between the two alloys further demonstrates

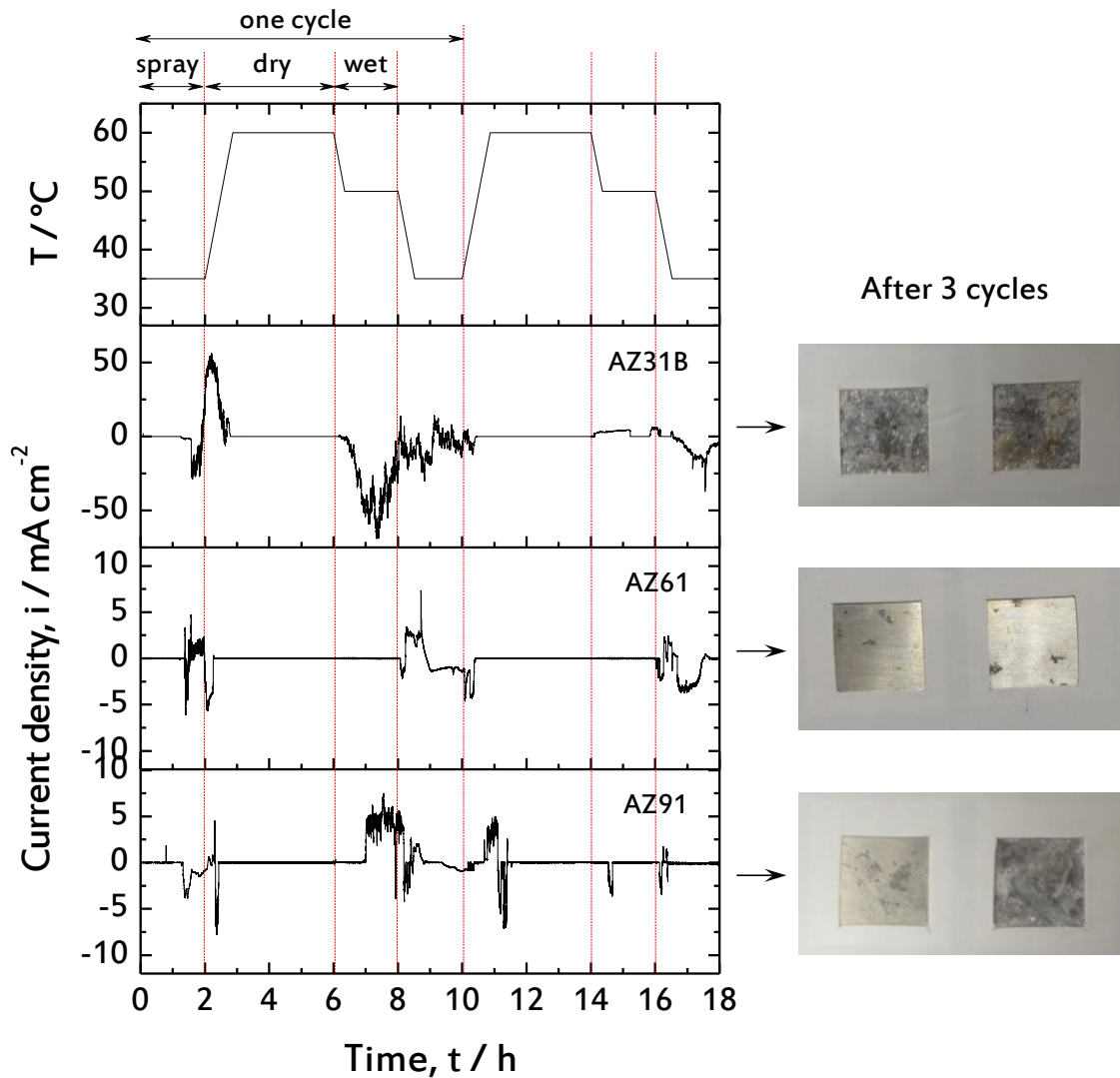


Fig. 3.8. Corrosion current transients of AZ31B, AZ61, and AZ91 during cyclic corrosion test.

Details of the spray-dry-wet steps are described in [Table 3.2](#).

that the rate of pitting propagation is more severe for AZ91, i.e., no blocking nature of adsorbed species.

Furthermore, the corrosion behavior of the AZ-type Mg alloys during CCT, which is composed of salt spray, drying, and wet steps, was analyzed by measuring the current



transients by means of a zero resistance ammeter (Fig. 3.8). Instead of continuous salt-spray testing, cyclic corrosion testing was performed to replace adequately the real time exposure conditions. During salt-spray step, a high concentration of salt (5 wt.%) was used in order to ensure comparability within 24 hrs of the tests. The positive and negative current values reflect the corrosion mainly on the WE1 (connected to working electrode) and WE2 (connected to counter electrode) during the tests, respectively. See Fig. 3.1 for the description of WE1 and WE2.

During first 1 h of salt spray, currents were nearly zero due to passivation or inadequacy of electrolyte levels on the electrode surfaces. However, after 1 h of salt spray, the current abruptly increased for all electrodes, as a result of pit initiation and propagation. Of them, AZ31B exhibits the highest rate of pit initiation and propagation, which became far higher in the initial staged of drying due to an increase in temperature and  $[Cl^-]$  concentration. The increase in  $[Cl^-]$  concentration is attributed to the evaporation of water. However, the effect of temperature was more noticeable than that of  $[Cl^-]$  concentration during the salt spray [6]. During the initial drying period of both AZ61 and AZ91, the current values were almost similar (or just slightly increased), as compared to those under salt spray period. This signifies that the increase in temperature does not greatly affect the rate of pit initiation and propagation in these alloys.

After the water molecules were dried up completely, the current values abruptly decreased to a nearly zero value again, thereby repassivating the surfaces. This indicates that the electrochemical corrosion stops for all electrodes. However, the wet stage provides water and promotes the progress of cathodic reaction, which further leads to corrosion. The main cathodic reaction in neutral aqueous solution is water reduction reaction. The dissolved salts facilitate the initiation of pits (or re-initiates) and propagate continuously with higher levels,

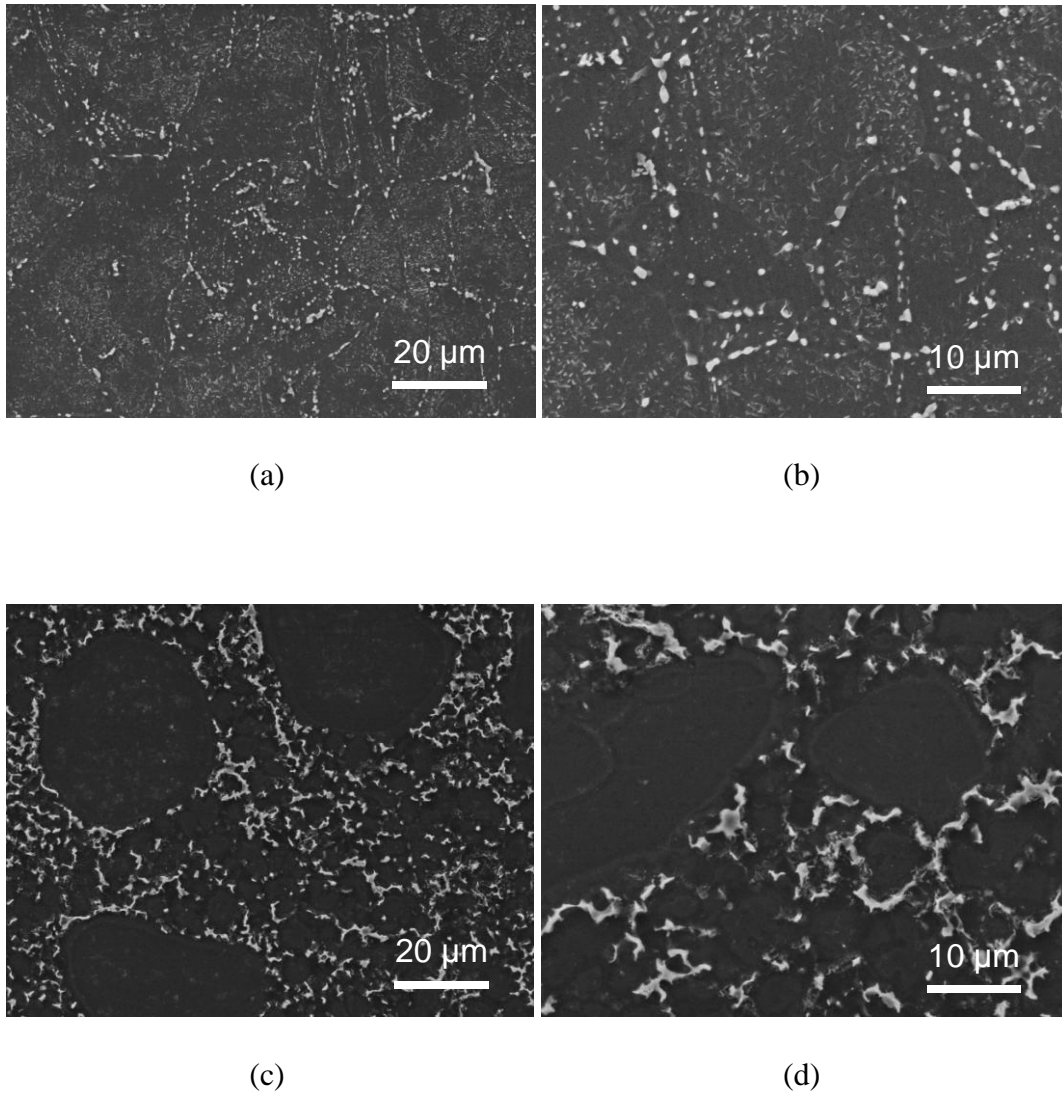


Fig. 3.9. SEM images of the alloys (a, b) AZ61 and (c, d) AZ91 (only polished and etched).

compared to the salt spray stage. The high corrosivity of the wet stage might be attributed to the high electrolyte temperature (50 °C) and the presence of concentrated  $\text{Cl}^-$  ions within the pits. However, only a small current flows through the AZ61 electrodes during the wet period, which indicates that this environmental condition is not corrosive enough for the pits to be initiated and propagated. This experimental result is consistent with that of another cyclic

corrosion test, except for minor variations. In any case, the results obtained for AZ61 during the wet period were always lower than those of AZ91. After the first cycle, the currents gradually decreased throughout the entire step, especially for AZ61 and AZ91 electrodes, probably due to the build-up of corrosion by-products.

In general, the higher the content of Al as an alloying element, the lower the corrosion susceptibility of the Mg alloys. Intriguingly, at temperatures higher than 40 °C, AZ91 with the highest Al content revealed lower corrosion resistance when compared to that of AZ61. On the other hand, at near room temperature, the corrosion resistance of AZ91 was superior to that of AZ61. Meanwhile, several authors have demonstrated that AZ91 suffers from a similar or higher corrosion attack compared to AZ61 and AZ80 under prolonged exposure conditions, typically for more than 24 d [6–8]. These suggest that the corrosion behavior of AZ-type Mg alloys has a strong dependence on their morphology and microstructure [8,28,29].

Furthermore, the distribution of  $\beta$ -phase, as a primary secondary phase of the Mg alloys, was examined by using SEM analysis, as shown in Fig. 3.9. In case of AZ91, SEM image indicates the segregation of a thick layer of  $\beta$ -phase at the grain boundaries of  $\alpha$ -Mg. Even if the  $\beta$ -phase exists within the  $\alpha$ -Mg, it is still thicker when compared to that existing at the grain boundaries. Besides, we could also observe many grains without any  $\beta$ -phase. On the other hand, in case of AZ61, the thickness of the segregation layer of  $\beta$ -phase at the grain boundaries was approximately half of that of AZ91. However, it could be noticed that nano-scale particles of  $\beta$ -phase were being effectively dispersed within the grains, as shown in Fig. 3.9(d). For the propagation of pit, it is mandatory to have a critical pit size or depth (a threshold value) at a given corrosive environment, for the occurrence of metastable-stable pit transition [30,31]. Moreover, on Mg alloys, the pitting corrosion is demonstrated to happen

mainly on the  $\alpha$ -matrix with a segregation of salt particles [2]. These imply that the chances for the growth of active pits beyond the critical size may be more remarkable in case of AZ91, when compared to AZ61. It further implies that in many Mg alloy corrosion behaviors depend strongly on the manufacturing processes, *e.g.* thermal and mechanical history, and thereby the distribution of the gradient  $\alpha$ - and  $\beta$ -phases. We do not have any proprietary technology embedded in these products. Instead, [ref. 33](#) might help predicting the manufacturing process of the wrought AZ61 and as-cast AZ91 alloys.

### 3-4. Conclusions

This chapter examined the effect of electrolyte temperature on the corrosion characteristics of AZ31B, AZ61, and AZ91 Mg alloys in 0.1 M NaCl. The  $E_{\text{corr}}$  of both AZ61 and AZ91 gradually increased with the electrolyte temperature due to the increase in charge transfer kinetics. In contrast, the  $E_{\text{corr}}$  of AZ31B decreased, although the charge transfer increased. This could be attributed to the severe increase in corrosion kinetics with high uniform corrosion. Although both AZ61 and AZ91 showed almost same charge transfer kinetics at all temperature ranges, the rate at which  $E_{\text{corr}}$  increased was more remarkable for AZ61 than that for AZ91. This could be attributed to the strengthening of surface passivation. Of the three different Mg alloys considered in this study, AZ61 exhibited the highest  $E_{\text{corr}}$  and lowest  $i_{\text{corr}}$  at 55 °C. Moreover, its first capacitive and inductive loops occurred at lower frequency domains compared to AZ91, at both  $E_{\text{OCP}}$  and  $-1.38 \text{ V}_{\text{Ag}/\text{AgCl}}$ . Therefore, AZ61 showed rather higher  $R_p$  than AZ91 at 55 °C. In addition, when anodically polarized at  $-1.38 \text{ V}_{\text{Ag}/\text{AgCl}}$ , the pitting current of AZ61 slowly increased with time, especially at 55 °C. Consequently, only a small current flowed through AZ61 during the wet period of cyclic corrosion test (50 °C). Therefore, the current transients during the wet period were always lower than those from AZ91. For pit initiation and propagation to continue further, there should be a critical pitting size for the metastable-stable pit transition. In case of AZ61, the thickness of the  $\beta$ -phase segregates at the grain boundary was approximately half of that of AZ91. However, the nano-scale  $\beta$ -phase particles were effectively dispersed within the grains of AZ61, whereas AZ91 has many grains that do not contain any  $\beta$ -phase. This implies that the possibilities for the grown of active pits beyond the critical size may be limited for AZ61 compared to AZ91.

## REFERENCES

- [1] G. Cole, Magnesium vision 2020: a north American automotive strategic vision for magnesium, Eds. J. Quinn, E. Hetrick, and S. Bairley, Southfield, MI: USAMP, (2006).
- [2] J. Chen, J. Wang, E.H. Han, and W. Ke, *Corros. Sci.* 51 (2009) 477.
- [3] L. Wang, T. Shinohara, and B.P. Zhang, *Mater. Des.* 33 (2012) 345.
- [4] C.A. Walton, H.J. Martin, M.F. Horstemeyer, and P.T. Wang, *Corros. Sci.* 56 (2012) 194.
- [5] G. Song, S. Atrens, *Adv. Eng. Mater.* 5 (1999) 11.
- [6] M.C. Merino, A. Pardo, R. Arrabal, S. Merino, P. Sasajus, and M. Mohedano, *Corros. Sci.* 52 (2010) 1696.
- [7] Z. Wen, C. Wu, C. Dai, and F. Yang, *J. Alloys Compd.* 488 (2009) 392.
- [8] A. Pardo, M.C. Merino, A.E. Coy, F. Viejo, R. Arrabal, and S. Feliú Jr., *Electrochim. Acta* 53 (2008) 7890.
- [9] R.K.S. Raman, *Metal. Mater. Trans. A* 35 (2004) 2527.
- [10] G. Song, A. Atrens, Z. Wu, and B. Zhang, *Corros. Sci.* 41 (1998) 1769.
- [11] A.F. Froats, T.K. Aune, and D. Hawke, W. Unsworth, J. Hillis, *Metals handbook*, vol.13, 9<sup>th</sup> ed., Corrosion ASM International, Materials Park, OH, (1987) 740.
- [12] R. Winston Revie, Herbert H. Uhlig, *Corrosion and corrosion control*, 4<sup>th</sup> edition, Wiley, (2008).
- [13]. T.P. Hoar, W.R. Jacob, *Nature* 216 (1967) 1299.
- [14] T. Shibata, T. Takeyama, *Nature* 260 (1976) 315.
- [15] Ulick R. Evans, *J. Chem. Soc.* (1929) 92.
- [16] C.L. McBee, J. Kruger, *Localized corrosion*, R.W. Staehle et al., Editors, NACE, Houston (1974) 252.
- [17] N. Sato, *Electrochim. Acta* 16 (1971) 1683.

- [18] Digby D. Macdonald, *J. Electrochem. Soc.* 139 (1992) 3434.
- [19] R.P. Vera Cruz, A. Nishikata, and T. Tsuru, *Corros. Sci.* 40 (1998) 125.
- [20] W.J. Beom, K.S. Yun, C.J. Park, H.J. Ryu, and Y.H. Kim, *Corros. Sci.* 52 (2010) 734.
- [21] A. Atrens, W. Dietzel, *Adv. Eng. Mater.* 9 (2007) 292.
- [22] G.S. Frankel, A. Samaniego, and N. Birbilis, *Corros. Sci.* 70 (2013) 104.
- [23] M. Keddad, O.R. Mottos, and H. Takenouti, *J. Electrochem. Soc.* 128 (1981) 257.
- [24] H. Schweikert, W.J. Lorenz, and H. Friedburg, *J. Electrochem. Soc.* 127 (1980) 1693.
- [25] C.S. Hsu, F. Mansfeld, *Corros.* 57 (2001) 747.
- [26] N. Pebere, C. Riera, and F. Dabosi, *Electrochim. Acta* 35 (1990) 555.
- [27] L.F. Lin, C.Y. Chao, and D.D. Macdonald, *J. Electrochem. Soc.* 128 (1981) 1194.
- [28] T. Zhang, Y. Li, and F. Wang, *Corros. Sci.* 48 (2006) 1249.
- [29] G. Song, A. Atrens, *Adv. Eng. Mater.* 5 (2003) 837.
- [30] G.S. Frankel, *J. Electrochem. Soc.* 145 (1998) 2186.
- [31] D.W. Buzza, R.C. Alkire, *J. Electrochem. Soc.* 142 (1995) 1104.
- [32] M.E. Orazem, J.M. Esteban, O.C. Moghissi, *Corros.* 47 (1991) 248.
- [33] K.N. Braszczynska-Malik, *Magnesium Alloys - Design, Processing and Properties* (F. Czerwinski ed.), InTech, 2011, pp. 95-112.

**IV. Improvement in Corrosion Characteristics of  
AZ31 Mg Alloy by Square Pulse Anodizing between  
Anodic Oxidation and Active Regions**



## 4-1. Introduction

One well-known industrial technology for surface protection of valve metals is anodizing. For Mg alloys, anodic films have thus far been primarily utilized to improve corrosion characteristics or further enhance adhesion with organic top layers [1,2]. Furthermore, a recent important development in this process has been the use of alkaline solutions with various additives such as  $\text{Na}_3\text{PO}_4$  [3],  $\text{KMnO}_4$  [4],  $\text{Na}_2\text{B}_4\text{O}_7$  [5–7],  $\text{NaAlO}_2$  [8,9] and  $\text{Na}_2\text{SiO}_3$  [3,5,7,8] as electrolytes with lower environmental impact than those containing fluoride and chromate.

However, film growth during anodizing involves the formation of a  $\text{Mg}(\text{OH})_2$  barrier layer, followed by the formation of pores in it [5–7,9,10]. Such a porous film will allow corrosive media to reach the substrate alloy easily; it will not offer any protection and will instead accelerate galvanic and general corrosion. Moreover, spongy nature of this film may reduce its adhesion with the substrate.

As another development in this process, several studies have explored the idea using a pulse current or potential (pulse anodizing) instead of a constant value to get a higher mean current density and thereby decrease the processing time and total energy consumption [11]. Qian et al. [12] applied a square pulse current of 0–40  $\text{mA cm}^2$  for 10–30 min on AZ91D Mg alloy in a NaOH solution containing meta-silicates, borates and other additives. However, a porous oxide layer still formed and the micro-pores actually seemed to widen with increasing anodizing time. Duan et al. [13] obtained plasma electrolytic oxidation (PEO) films on AZ91D Mg alloy by applying a square pulse potential of 350–400 V for 1–2 h in a KOH solution containing various additives. Though they found that fluoride- and phosphate-containing electrolytes were the most effective in improving the corrosion resistance of

AZ91D Mg alloy, micro-pores still remained in the anodic films. Liu et al. [14] obtained a protective passive film on pure Mg by applying pulse potential between passive ( $-0.5 V_{SCE}$ ) and passive/active regions ( $-1.36 V_{SCE}$ ) for 30 min in 0.25 M  $Na_2SO_4$  + 0.1 M NaOH solution. To our knowledge, no other reports on square pulse anodizing exist, especially on conventional anodizing of Mg alloys.

In this chapter, we describe a novel anodizing technique that significantly limits the formation of micro-pores on the anodic films and thereby increases the corrosion resistance. The process involves applying the pulse potential specifically between anodic oxidation and active regions of AZ31 Mg alloy in 2 M NaOH alkaline solution at 303 K.

## 4-2. Experimental

Specimens were AZ31 Mg alloys with the chemical composition as shown in Table 4.1. Prior to anodizing, all surfaces were ground with fine-grained emery paper of up to 2000 grit, polished with 0.05- $\mu\text{m}$  alumina powder, cleaned by ultrasonication in ethanol for 5 min, and finally rinsed with distilled water and quickly dried. The working area of each specimen was bounded with hydrophobic adhesive masking tape to leave an exposed area of  $1\text{ cm}^2$  ( $1\text{ cm} \times 1\text{ cm}$ ). Samples were kept in a vacuum desiccator to avoid any contact with oxygen molecules and moistures before use.

After storing in the vacuum desiccator for 1 day, the specimens were anodized in 2 M NaOH aqueous solution with a square pulse potential (Fig. 4.1) between the anodic oxidation ( $E_t$ ) and active regions ( $E_a$ ). The specimens were also anodized at a constant potential of  $E_t$ . The volume of the solution used in each experiment was  $200\text{ cm}^3$  and it was stirred by a magnetic stirrer. The pulse potential was well distributed across the electrode surface by controlling the duty ratio  $\alpha$ . The following process parameters were used: temperature =  $303 \pm 1\text{ K}$ ;  $E_t = 10\text{ V}_{\text{Ag}/\text{AgCl}}$  applied for duration  $t_t = 5, 10, \text{ and } 50\text{ s}$ ;  $E_a = -1.35\text{ V}_{\text{Ag}/\text{AgCl}}$  applied for duration  $t_a = 1\text{ s}$ ; therefore  $\alpha (\%) = t_t / (t_t + t_a) \times 100 = 83, 91, \text{ and } 98$ , respectively.

Table. 4.1. Chemical composition (wt.%) of AZ31 Mg alloy used in this study.

Mg	Al	Zn	Mn	Si	Cu	Ni	Fe
Bal.	3.0	1.0	0.43	0.01	< 0.01	< 0.001	0.003

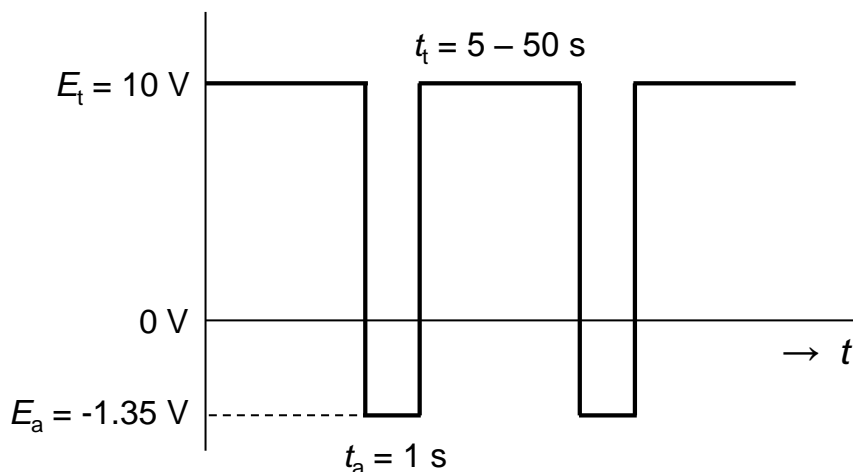


Fig. 4.1. Waveform for applied square pulse potential

After anodizing, the corrosion characteristics of the specimens were assessed by linear potential sweep voltammetry and electrochemical impedance spectroscopy (EIS) in deaerated 0.1 M NaCl aqueous solution at  $303 \text{ K} \pm 1$ . The former was carried out in a potential range from  $-0.2$  to  $+0.3 \text{ V}_{\text{Ag}/\text{AgCl}}$  vs. open circuit potential ( $E_{\text{OCP}}$ ) with a scan rate set to  $1 \text{ mV s}^{-1}$  in order to minimize the degradation and further destruction of the anodic film by hydrogen evolution during the cathodic process. In the EIS measurement, the real and imaginary part of the electrochemical cell were evaluated over a nominal frequency range of  $10^4 \text{ Hz}$  to  $1 \text{ Hz}$  with a  $10 \text{ mV}$  amplitude, where the applied potential was  $E_{\text{OCP}}$ . All the electrochemical measurements were performed in a three-electrode system after the stabilization of  $E_{\text{OCP}}$ . The Mg alloy of interest was used as the working electrode (WE); platinum wire, as the counter electrode (CE); and Ag/AgCl electrode containing saturated KCl, as the reference electrode (RE).

## 4-3. Results and discussion

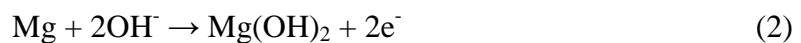
### 4.3.1. Anodic polarization behavior of AZ31 Mg alloy

Prior to pulse anodizing, linear potential sweep voltammetry was carried out to determine  $E_t$  and  $E_a$ . As shown in Fig. 4.2, the obtained anodic polarization curve can be largely divided into two parts, namely, the active region and the transpassive region. The active region can be again divided into the primary passive region and the secondary passive region.

Anodic dissolution of Mg alloy began at  $E_{OCP}$  of  $-1.55 \text{ V}_{Ag/AgCl}$  and the current density increased with the anodic overpotential. This region mainly corresponds to the anodic process, that is, the formation of the anodic oxidation product ( $\text{Mg}^{2+}$ ). The formation of  $\text{Mg}^{2+}$  in alkaline solution follows the kinetics of two-electron transfer [15].



The rate of increase in current density of this active-passive metal was significantly limited by shifting the anodic overpotential toward the more positive direction due to the initial formation of a passive film on the electrode surface. Film formation progressively reduced the oxidation current to finally lead to passivation at  $-1.2$  to  $-0.8 \text{ V}_{Ag/AgCl}$  (primary passivity). The electrochemical reaction for anodic oxidation in this primary passive state corresponds to the direct oxidation process of  $\text{Mg}(\text{OH})_2$  [16].



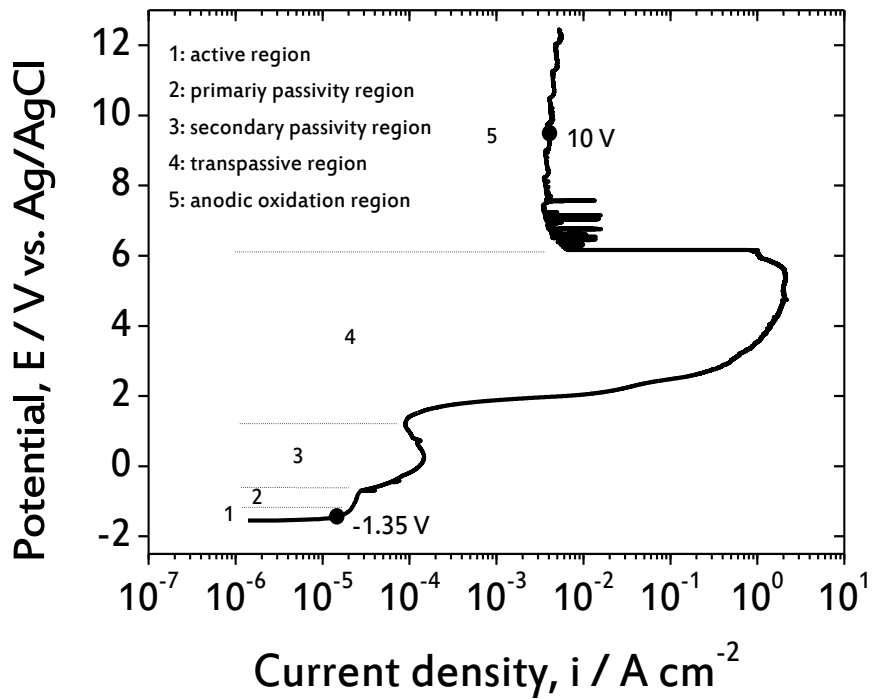
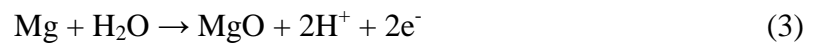


Fig. 4.2. Anodic polarization behavior of AZ31 Mg alloy in 2 M NaOH solution at 303 K with a scan rate of 1 mV s<sup>-1</sup>.

However, the current density subsequently increased with anodic overpotential at an applied potential at -0.8 V<sub>Ag/AgCl</sub> due to the breakdown of the primary passivation film. Subsequently, the alloy becomes passive once again (secondary passivity) at 0.2–1.5 V<sub>Ag/AgCl</sub>. This secondary passive state occurs by direct oxidation of MgO on the electrode surface [16].



Beyond  $1.5 V_{\text{Ag/AgCl}}$ , the current density increased again due to the oxygen evolution reaction which could be clearly observed with the naked eye on the electrode surface. The alloy finally developed a porous anodic film at an applied potential of  $6.2 V_{\text{Ag/AgCl}}$ .

Thus, as mentioned,  $E_t$  and  $E_a$  were set to 10 and  $-1.35 V_{\text{Ag/AgCl}}$ , respectively.  $E_a$  values greater than  $-1.35 V_{\text{Ag/AgCl}}$  had no positive effect on corrosion resistance in our study.

### ***4.3.2. Changes in current transient behavior of AZ31 Mg alloy during pulse anodizing***

After the linear potential sweep measurements, current transients under a constant potential step and square pulse potential step with the various  $\alpha$  were obtained in a 2 M NaOH solution at 303 K in order to investigate the effect of the square pulse potential on the anodizing behavior of Mg alloy.

As shown in Fig. 4.3, the  $\alpha$  value had significant influence on the anodizing behavior over 1000 s. Note that all the intricate details of the current values are not necessary for this discussion; thus, only the current values extracted from point A (see Fig. 4.4) are represented in Fig. 4.3. At the initial stages of anodizing, the current density was somewhat high, but decreased gradually with anodizing time over the first 10 s. The higher current density at the starting point of anodizing is due to the fact that the electrical field simply flows through the metallic Mg. The current density decreased due to the formation of the anodic film, which surely exhibits higher corrosion resistance than plain metallic Mg. The current density then turned upward to a maximum value  $i_{\text{max}}$  at  $t_{\text{max}}$ . It subsequently decreased gradually with anodizing time and reached a constant level. These current contributions are presumably related to a series of destruction, nucleation, and growth process of MgO on the electrode

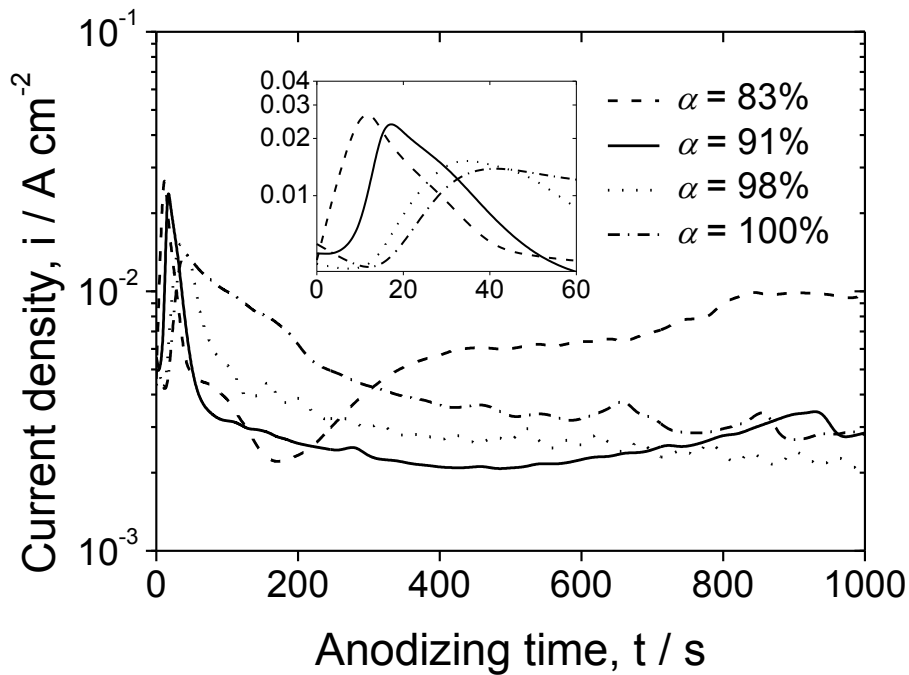


Fig. 4.3. Approximate data plots of the anodizing behavior for AZ31 Mg alloy over 1000 s as a function of duty ratio in 2 M NaOH at 303 K. These current are values extracted from point A (see Fig. 4) during the whole anodizing process.

surface. Juhl et al. [11] reported that small imperfections occur in the film due to the concentration gradient of the current between the areas with a relatively thinner oxide layer and the rest of the surface. They also suggested that these small imperfections occur on the subgrain boundaries of the electrode where the initial formation of an electrochemical cell starts. This area exhibits less resistance to current and leads to the decrease in current density. The pulse potential induced a steep decrease in current density from  $i_{\max}$  as anodizing time progressed, which indicates that the kinetics of nucleation and growth of anodic film are more remarkable than that under constant potential. An increase in the thickness of anodic film and thereby an increase in resistance caused a further decrease in current density. Finally,



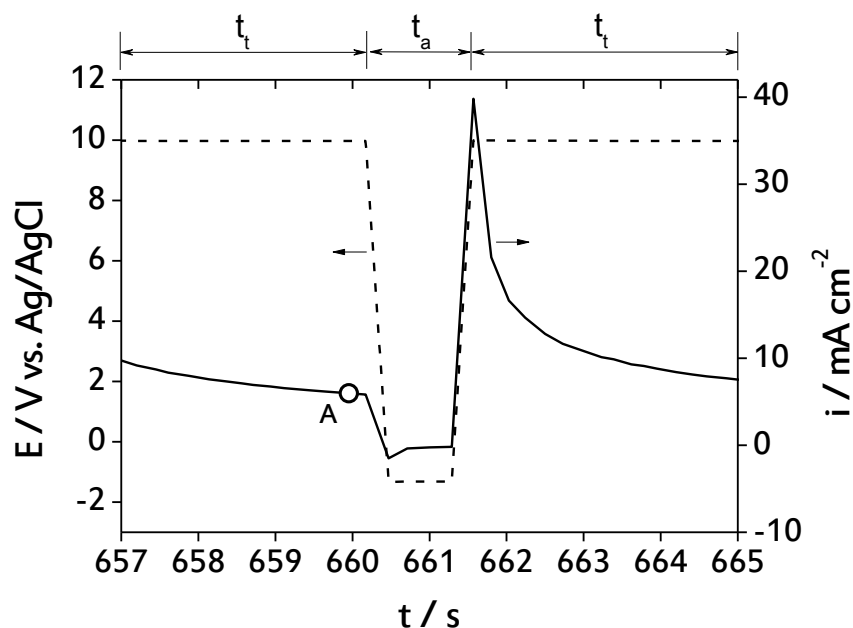


Fig. 4.4. Further detailed waveform view of square pulse potential and its current density response ( $t_t$ : Duration for applying anodic oxidation potential,  $t_a$ : Duration for applying anodic potential).

the current density reached a constant level, where the rate of anodic dissolution and anodic film formation reached a steady state. The average time to reach the steady state current was approximately 2 times lower than that under a constant potential.

The detailed waveform of the square pulse potential and its current density response (Fig. 4.4) showed slight variation with  $\alpha$  and anodizing time, but the general information is almost the same: The main reaction during  $t_a$  is the electrochemical dissolution of the anodic film. This dissolution reaction can remove the weak spots on anodic film layer by the potential edge effect and can increase the concentration of reactant species near the interface. When the applied potential was changed to  $E_t$  again, the electric field across the anodic film increased

drastically to about  $40 \text{ mA cm}^{-2}$  to form anodic film further. This indicates that the mean current density obtained at the electrode surface is higher than that with a constant potential, which confirms the finding of Juhl et al. [11], who reported that pulse anodizing affords a higher mean current density and thereby decreases processing time and total energy consumption.

### ***4.3.3. Effect of pulse parameters on the anodic polarization behavior of AZ31 Mg alloy***

Anodic polarization tests were carried out in order to investigate the effect of a square pulse potential on the corrosion characteristics of AZ31 Mg alloy in deaerated 0.1 M NaCl solution at 303 K (Fig. 4.5). As shown in Fig. 4.6, the corrosion potential  $E_{\text{corr}}$  and current  $i_{\text{corr}}$  of samples clearly followed mixed potential theory, according to which a lower hydrogen generation rate or higher oxidation reaction rate leads to lower  $E_{\text{corr}}$  and  $i_{\text{corr}}$ . The pitting potential  $E_{\text{pit}}$  was defined as the anodic potential at which the current density begins to rise sharply with an increase in overpotential.

It was seen at an anodizing time of 300 s that an  $\alpha$  of 83 afforded the highest  $E_{\text{pit}}$  of -1.41 V<sub>Ag/AgCl</sub> and lowest  $i_{\text{corr}}$  of  $38.4 \mu\text{A cm}^{-2}$ ; further increase in  $\alpha$  led to a decrease in  $E_{\text{pit}}$  and an increase in  $i_{\text{corr}}$ . In addition, the absolute anodizing time seems to become a significant parameter as the anodizing time progressed. With increasing anodizing time, the corrosion resistance at an  $\alpha$  of 83 was deteriorated continually whereas that at  $\alpha$  of 98 and 100 was improved. Finally,  $E_{\text{pit}}$  was increased and  $i_{\text{corr}}$  was decreased with increasing  $\alpha$  at 900 s. These experimental observations are well consistent with those of the current transient test results. The lower current density response represents the higher corrosion resistance of the formed

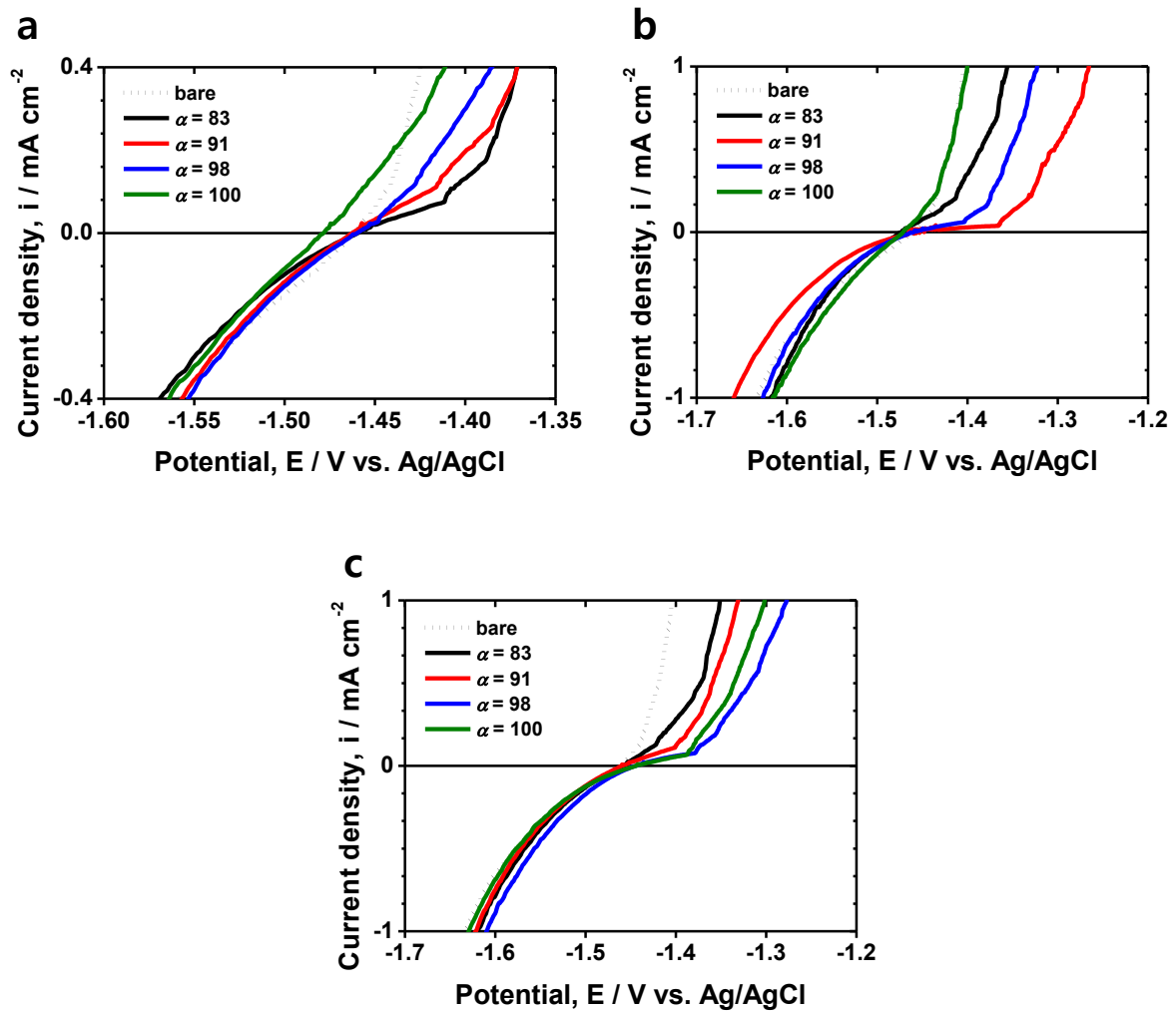


Fig. 4.5. Changes in anodic polarization behavior of anodized AZ31 Mg alloy as a function of duty ratio  $\alpha$  in deaerated 0.1 M NaCl at 303 K. Anodizing time: (a) 300 s, (b) 600 s, and (c) 900 s.

anodic film.

Overall, the specimen anodized with an  $\alpha$  of 91 for 600 s exhibited the highest  $E_{\text{pit}}$  of -1.37 V<sub>Ag/AgCl</sub> and lowest  $i_{\text{corr}}$  of 17.06  $\mu\text{A cm}^{-2}$ , in particular, clearly displayed the highest

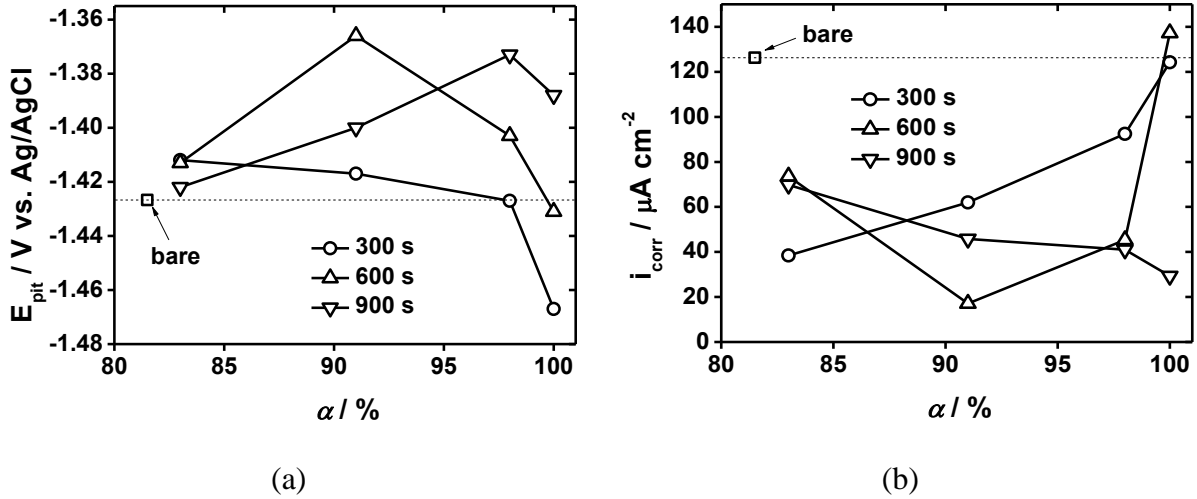


Fig. 4.6. Variation in (a)  $E_{\text{pit}}$  and (b)  $i_{\text{corr}}$  as a function of duty ratio  $\alpha$ .

improvement in corrosion resistance. Moreover, the current density response under these conditions was the lowest value of  $2.15 \text{ mA cm}^{-2}$  as clearly seen in Fig. 4.3, indicating that the corrosion protection effect of the formed anodic film was more remarkable than in the other specimens. This phenomenon arises presumably because the anodic dissolution rate of  $\text{Mg}^{2+}$  during the anodizing process achieved a counter-balance with the formation of the anodic film. In other words, reactant species became depleted near the interface (namely, the electrode surface-OHP distance) during the anodizing process, but it is replenished from the bulk solution when electric source alters the polarity and allows the working electrode to act as a cathode. This indicates that intermittent desorption of reactant species during the anodizing process plays an important role in forming an anodic film on Mg alloy. Desorption of the reactant species occurs when applying  $E_a$  for  $t_a$ , and in this case,  $\alpha$  becomes a significant parameter in addition to  $E_a$ . These indications point to the possibility that anodizing can be conducted at high potential due to the replenishment of the reactant species

during  $t_a$ . This will decrease the total manufacturing time and further decrease production cost [11]. However, we found no positive effects on corrosion resistance at  $E_a$  than  $-1.35 \text{ V}_{\text{Ag}/\text{AgCl}}$ , even though  $E_a$  is in the primary passivity zone. Thus, considering the fact that anodizing time in commercial plants is approximately 5–10 min, anodizing with a low  $\alpha$  value might be a better choice for improved corrosion resistance in Mg alloys.

#### ***4.3.4. Effects of pulse anodizing on the EIS response of AZ31 Mg alloy***

EIS measurements were performed in order to understand the corrosion kinetics across the modified anodic film and substrate interface of AZ31 Mg alloy. Note that measurements at low frequencies (below 1 Hz) are not discussed because some of the specimens involved an inductive loop or useless fraction of noise at these very low frequencies. Several significant studies have ascribed the inductive behavior to corrosion [17] and oxidation of metals [18,19]. Armstrong et al. [20] ascribed the inductive behavior in a multistep reaction to the chemisorption of reactant species during the activation step. It could also be a result of the inhomogeneous distribution of current on the electrode surface. However, it is still difficult to recognize the origin of inductance behavior and there is no clear explanation for it.

Figure 4.7 shows an electrical equivalent circuit model for the anodized Mg alloy used in this study. Impedance plots showed a characteristic depressed semicircle implying the deviation from ideality, as seen in Fig. 4.8. Therefore, a constant phase element (CPE) was utilized to compensate for the deviation. An absolute quantification method for the capacitance from CPE was developed by Hsu et al. [21].

$$C_{dl} = Q^{\circ} (f_{\max})^{n-1} \quad (5)$$

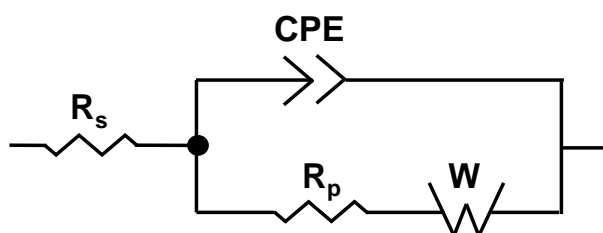


Fig. 4.7. Electrical equivalent circuit model used in this study.

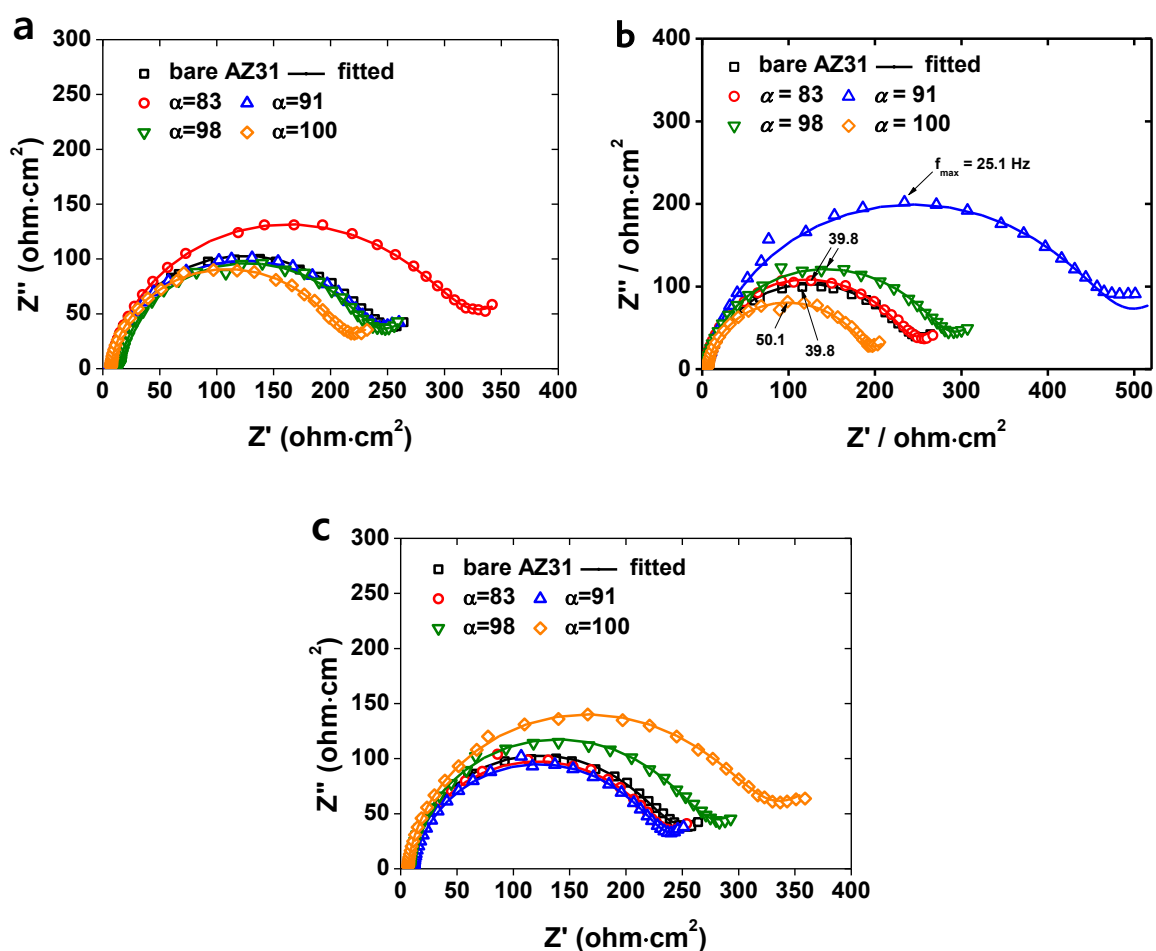


Fig. 4.8. Measured Nyquist plots of anodized AZ31 Mg alloys immediately after immersion in deaerated 0.1 M NaCl at 303 K: anodized for (a) 300 s (b) 600 s, (c) 900 s.

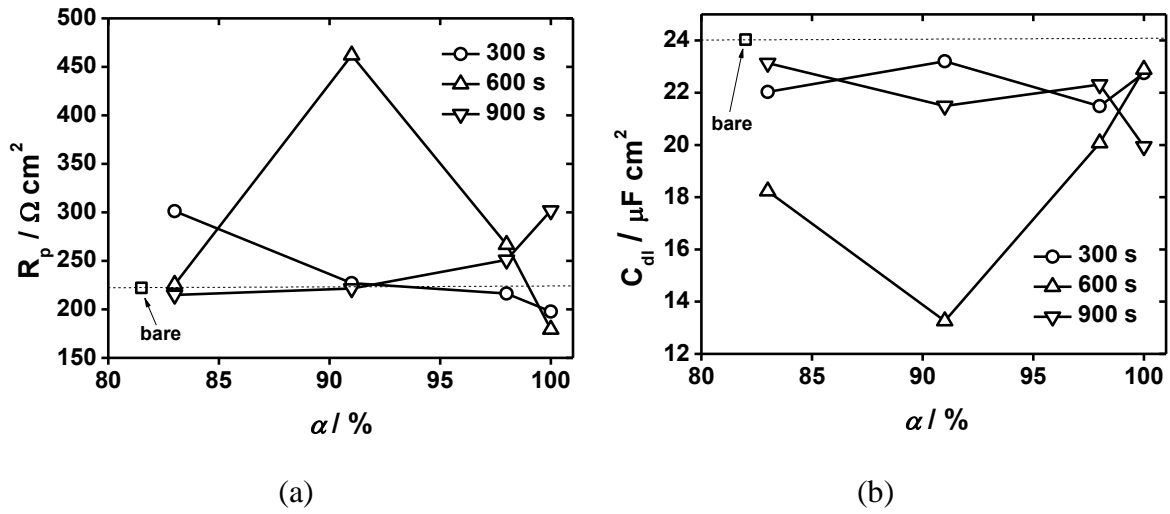


Fig. 4.9. Variation in (a) polarization resistance  $R_p$  and (b) double layer capacitance  $C_{dl}$  of anodized AZ31 Mg alloy as a function of duty ratio  $\alpha$  in deaerated 0.1 M NaCl at 303 K estimated by fitting the measured impedance spectra.

where,  $C_{dl}$  is the double layer capacitance;  $Q^o = S s^n$  ( $S = \text{siemens (1/ohm)}$ ,  $s = \text{second}$ );  $f_{max}$  is the frequency at which the imaginary component reaches a maximum; and  $n$  is an exponent. As shown in Fig. 4.9, an  $\alpha$  value of 83 afforded the highest polarization resistance  $R_p$  of  $0.30 \text{ k}\Omega \text{ cm}^2$  at 300 s;  $R_p$  decreased as  $\alpha$  increased. However, with increasing anodizing time,  $R_p$  decreased gradually at an  $\alpha$  of 83, but increased at an  $\alpha=100$ . Finally, at an anodizing time of 900 s,  $R_p$  increased with  $\alpha$  value. It is clear that an  $\alpha$  of 91 indeed afforded the highest  $R_p$  of  $0.46 \text{ k}\Omega \text{ cm}^2$  and lowest  $C_{dl}$  of  $13.2 \mu\text{F cm}^2$ . These experimental observations are consistent with those of the anodic polarization test.

The corrosion resistance of the Mg alloy beneath the anodic film can be adequately explained by  $R_p$ , which maybe proportional to  $E_{pit}$  and inversely proportional to  $i_{corr}$ , as

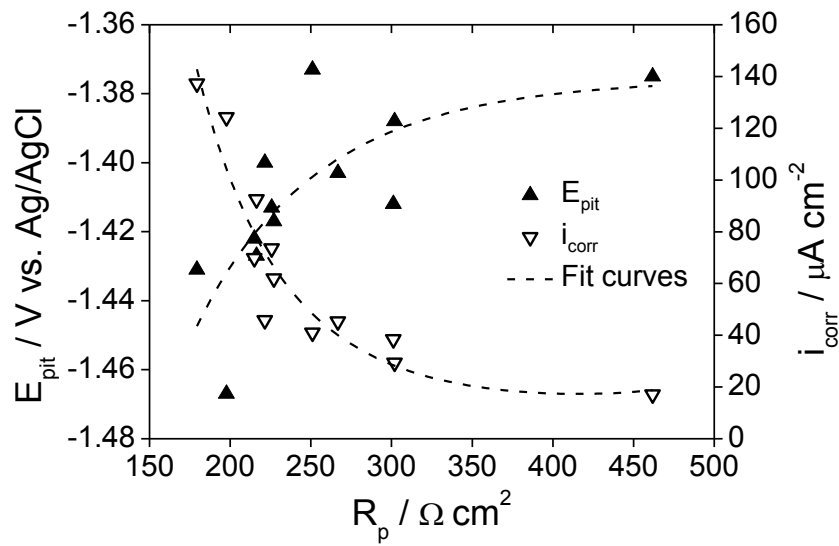


Fig. 4.10. The close interrelationship between the results of the anodic polarization test ( $E_{\text{pit}}$  and  $i_{\text{corr}}$ ) and the EIS test ( $R_p$ ).

clearly seen in Fig. 4.10. Moreover,  $C_{\text{dl}}$  has a close relationship with the adhesion force of the anodic film, which prevents contact of the substrate with the electrolyte. This indicates that the specimen anodized with an  $\alpha$  of 91 for 600 s has an anodic film with relatively low corrosion of the substrate.

In addition, these phenomena can be explained on the basis of the micro-pores formed on the anodic film layer. A relatively high value of  $R_p$  for the specimen anodized at an  $\alpha$  of 91 for 600 s indicates that it is more difficult for  $\text{Cl}^-$  to penetrate because the protective anodic film is denser and more uniform than that of the specimen anodized at an  $\alpha$  of 100. It is well known that micro-pores form during the anodizing process because the  $\text{MgO}$  formed on the  $\text{Mg}$  alloy has a molar volume of  $11.3 \text{ cm}^3 \text{ mol}^{-1}$ , whereas  $\text{Mg}$  metal has a molar volume of



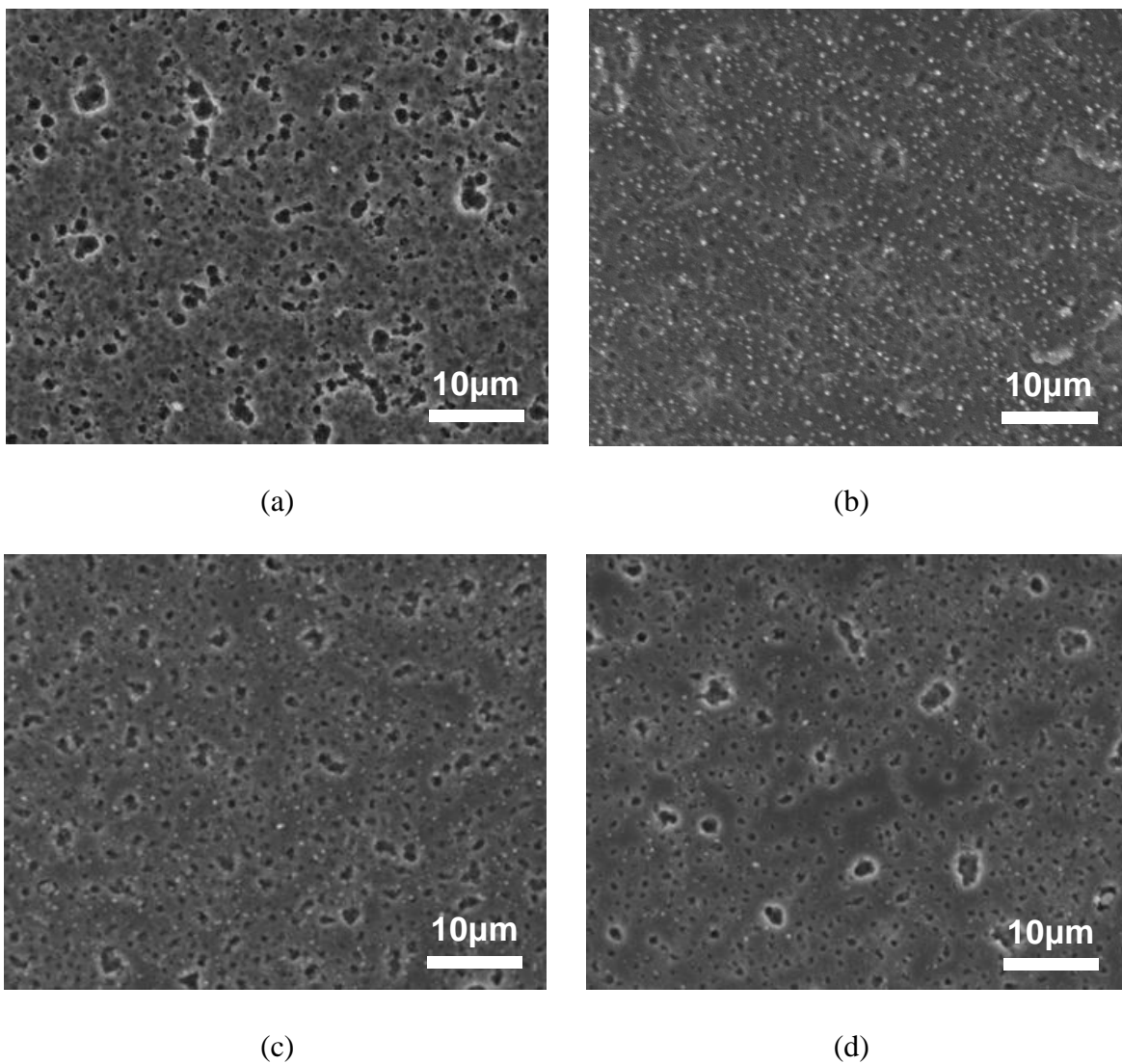


Fig. 4.11. Change in surface morphology of the anodic films formed in 2 M NaOH for 600 s with duty ratios (a)  $\alpha = 83$ , (b)  $\alpha = 91$ , (c)  $\alpha = 98$ , and (d)  $\alpha = 100$  (constant potential). The corresponding thickness of anodic film was about 0.6–1.0  $\mu\text{m}$ .

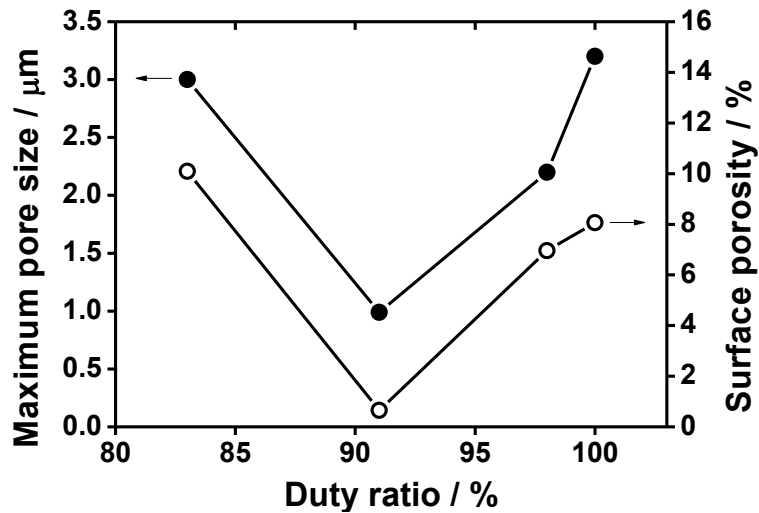


Fig. 4.12. Variation in pore size ( $\mu\text{m}$ ) and surface porosity (%) of the anodic films as a function of duty ratio  $\alpha$ .

$14.0 \text{ cm}^3 \text{ mol}^{-1}$ , which gives a Pilling–Bedworth ratio of 0.81 [22]. Since preventing the creation of micro-pores is impossible, reducing their size and distribution is the natural alternative. As seen in Figs. 4.11 and 4.12, we could decrease the maximum pore diameter to less than  $1 \mu\text{m}$  and, furthermore, reduce the surface porosity 11 fold, from 8.06 % to 0.65 %. The dissolved  $\text{Mg}^{2+}$  during  $t_a$  seems to directly contribute to the formation of anodic film in the formed micro-pores, as seen in the surface morphology of the specimen anodized at an  $\alpha$  of 98: there were no observable differences in the size and distribution of small-diameter pores, but those of large-diameter pores were significantly reduced by the pulse potential (Fig. 4.11c). However, unexpected pits and cavities may remain in the anodic film if the rate of anodic dissolution is intensified ( $\alpha = 83$ ), which will induce an increase in current density response with anodizing time, as seen in Fig. 4.3. Moreover, the thicknesses of anodic films

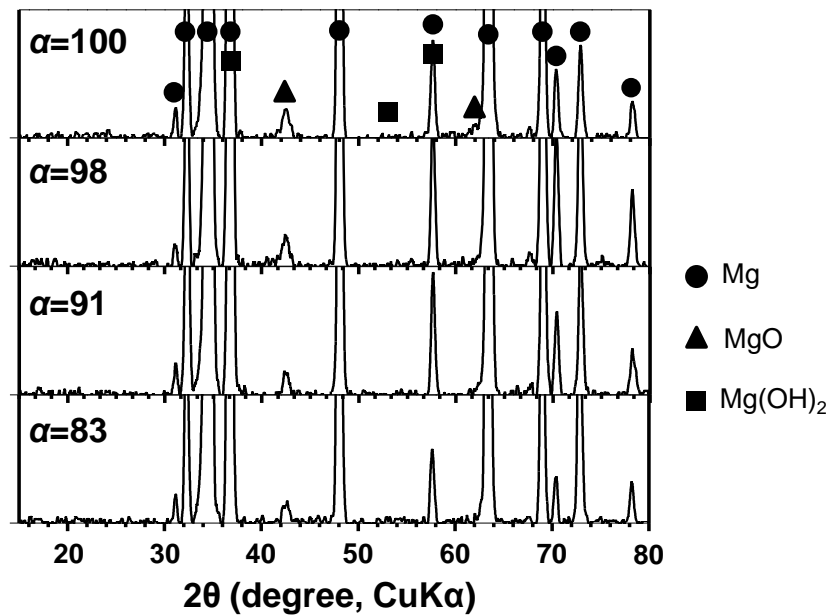


Fig. 4.13. Typical X-ray diffraction pattern of the anodic films ( $\text{MgO}$ ) formed on AZ31 Mg alloy with the different duty ratios  $\alpha$  for 600 s.

were approximately  $0.6\text{--}1.1\ \mu\text{m}$ , and were increased with the decrease in  $\alpha$  because of the increase in mean current density during the whole anodizing process. In general, the maximum pore size of anodic film increased with the film thickening [4]; however, these micro-pores were effectively filled with anodic films by the pulse potential (Fig. 4.11b). As shown in Fig. 4.13, the anodic films were mainly composed of  $\text{MgO}$ . However, there was no direct relationship between the formation of  $\text{MgO}$  and  $\alpha$ .

## 4-4. Conclusions

This chapter examined the effects of square pulse anodizing on the surface morphology and resultant corrosion characteristics of AZ31 Mg alloy. A square pulse potential between the anodic oxidation region ( $10 \text{ V}_{\text{Ag/AgCl}}$ ) and active region ( $-1.35 \text{ V}_{\text{Ag/AgCl}}$ ) was applied on the electrode surface with different duty ratios  $\alpha$  in 2 M NaOH at 303 K. At the initial stages of anodizing, the corrosion resistance increased as  $\alpha$  decreased due to the increase in mean current density. However, the absolute anodizing time became a significant parameter as the anodizing time progressed. Therefore, the corrosion resistance of specimens anodized at low  $\alpha$  deteriorated, whereas that of specimens anodized at high  $\alpha$  improved with the anodizing time. However, it was noticeable that the specimen anodized at an  $\alpha$  of 91 for 600 s exhibited the best corrosion resistance, which was confirmed to be due to the decrease in pore size and surface porosity of the anodic film. The maximum pore diameter was less than  $1 \mu\text{m}$  and the surface porosity was about 11 times lower than that for samples anodized at a constant voltage. This smooth anodic film on the AZ31 Mg alloy arises presumably because the intermittent desorption of  $\text{Mg}^{2+}$  during the anodizing process achieved counter-balance with the formation of the anodic film. In the other words, the artificial formation of  $\text{Mg}^{2+}$  during the anodizing process may remove the weak spots of the formed anodic film layer by potential edge effect and thereby increase the concentration of reactant species near the electrode/electrolyte interface. This dissolved  $\text{Mg}^{2+}$  seems to directly contribute to the formation of anodic films in micro-pores. However, unexpected pits and cavities may be left in the anodic film if the rate of anodic dissolution is intensified.

## REFERENCES

- [1] C. Blawert, W. Dietzel, E. Ghali, and G. Song, *Adv. Eng. Mater.* 8(6) (2006) 511.
- [2] Y. Kojima, *Mater. Sci. Forum* 350(3) (2000) 3.
- [3] Y.S. Jang, Y.K. Kim, I.S. Park, S.J. Lee, M.H. Lee, J.M. Yoon, and T.S. Bae, *Surf. Interface Anal.* 41 (2009) 524.
- [4] D.Y. Hwang, Y.M. Kim, D.Y. Park, B.Y. Yoo, and D.H. Shin, *Electrochim. Acta* 54 (2009) 5479.
- [5] Z. Shi, G. Song, and A. Atrens, *Corros. Sci.* 48 (2006) 1939.
- [6] H. Duan, C. Yan, and F. Wang, *Electrochim. Acta* 52 (2007) 3785.
- [7] X. Guo, M. An, *Corros. Sci.* 52 (2010) 4017.
- [8] L. Chai, X. Yu, Z. Yang, Y. Wang, and M. Okido, *Corros. Sci.* 50 (2008) 3274.
- [9] S. Verdier, M. Boinst, S. Maximovitch, and F. Dalard, *Corros. Sci.* 47 (2005) 1429.
- [10] A. Yabuki, M. Sakai, *Corros. Sci.* 51 (2009) 793.
- [11] A. D. Juhl, Ph.D. thesis, Inst. of Manufacturing Engineering, The Technical University of Denmark (1999).
- [12] J. G. Qian, C. Wang, D. Li, G.L. Guo, and G.L. Song, *Trans. Nonferrous Met. Soc. China* 18 (2008) 19.
- [13] H. Duan, C. Yan, and F. Wang, *Electrochim. Acta* 52 (2007) 3785.
- [14] X. Liu, T. Zhang, Y. Shao, G. Meng, and F. Wang, *Corros. Sci.* 51 (2009) 1772.
- [15] S.A. Salman, R. Ichino, and M. Okido, *Int. J. Corros.* 2010 (2010) 7.
- [16] Z. Cai, D. Lu, W. Li, Y. Liang, and H. Zhou, *Int. J. Hydrogen Energy* 34 (2009) 467.
- [17] M. Keddam, O.R. Mattos, and H. Takenouti, *J. Electrochem. Soc.* 128 (1981) 257.
- [18] D.D. Macdonald, *Electrochim. Acta* 35 (1990) 1509.

- [19] L. Bai, B.E. Conway, *Electrochim. Acta* 38 (1993) 1803.
- [20] R.D. Armstrong and M. Henderson, *J. Electroanal. Chem.* 39 (1972) 81.
- [21] C.H. Hsu, F. Mansfeld, *Corros.* 57 (2001) 747.
- [22] C. Blawert, W. Dietzel, E. Ghali, and G. Song, *Adv. Eng. Mater.* 8 (2006) 511.

**V. Surface Porosity Tuning and Simultaneous  
Formation of Al-enriched Oxide Layer by Pulse-  
Anodizing AZ31 Magnesium Alloy**

## 5-1. Introduction

Anodization is an electrolytic passivation process that produces a thick, chemically stable protective oxide film on valve metals. Anodization mitigates the general and galvanic corrosion of bare Mg alloys, but the formed anodic films are more water soluble than those formed on Al alloys, which are rival traditional materials for weight reduction. Therefore, anodization is often used to produce an undercoating layer to provide better adhesion for various organic finishes [1,2]. In general, the anodic films formed on Mg alloys can be divided into two sub-layers: a very thin but dense inner layer and thick porous outer layer [1]. Of these layers, the porosity of outer layer is strongly influenced by the various anodizing parameters such as the electrolyte, concentration, temperature, electric field applied, and so on. The formation of compact anodic films on Mg alloys is limited, because MgO has a molar volume of  $11.3 \text{ cm}^3 \text{ mol}^{-1}$ , whereas metallic Mg has a molar volume of  $14.0 \text{ cm}^3 \text{ mol}^{-1}$ , and therefore the Pilling-Bedworth ratio is 0.81 [3]. In this context, several researchers have elucidated the mechanism for the corrosion of the anodic film through the two types of pores, i.e., the non-through-pores and through-pores [4,5]. In addition, many researchers have examined the causal relationship between the microstructure (such as the sizes and distribution of pores) and electrochemical characteristics of anodized Mg alloys [6–8]. Thus, the pore characteristics of the anodic film are fundamental consideration in the accurate evaluation of the corrosion performance of anodic films.

The author have previously proposed a novel anodizing technique in which a pulse potential between the anodic oxidation and active regions for the AZ31 alloy is applied in 2 M NaOH alkaline solution [9]. Note that passive metals such as Fe, Cr, Ni with transpassive dissolution are not appropriate for corrosion protection by anodization. Similarly, the



passivity of Mg breaks down at about  $2 V_{\text{Ag/AgCl}}$  with high transpassive dissolution rate of various  $\text{A cm}^{-2}$  in 2 M NaOH. However, the transpassive dissolution stops abruptly at the extended transpassive range which is higher than  $6 V_{\text{Ag/AgCl}}$  up to hundreds of volts. This property was used to develop oxide films of Mg alloys for corrosion protection [9]. The main idea of this pulse anodization is that the active potential may remove the weak spots on the anodic film through the potential edge effect and thereby increase the concentration of reactant species near the electrode/electrolyte interface. In consequence, a specimen anodized with a duty ratio, i.e. the time percentage of the duration of anodic oxidation potential to total anodization period (refer to the experimental section), of 91% for 600 s exhibited the highest corrosion resistance in 0.1 M NaCl solution because of the decrease in the size and the number of pores over the anodic film [9].

In this chapter, we further investigate the effects of the pulse repetition frequency  $f$  under a constant  $\alpha$  of 91 on the microstructure and corrosion characteristics of the anodic film formed on AZ31 Mg alloy. Moreover, the effects of the pulse potentials between the anodic oxidation and active regions on the microstructure of the anodic film layer are studied more systematically.

## 5-2. Experimental

The coupons used were wrought AZ31 alloy with a chemical composition as follows: 3.0 wt% Al, 1.0 wt% Zn, 0.43 wt% Mn, 0.01 wt% Si, < 0.01 wt% Cu, <0.001 wt% Ni, <0.003 wt% Fe, and the balance Mg. The surfaces of the coupons were mechanically ground with emery paper up to 2000 grit, buffed with 0.05- $\mu\text{m}$  alumina powder, cleaned with an ultrasonic cleaning system in ethanol for 5 min, and finally dried under cold air. The working area was bounded with hydrophobic adhesive masking tape to leave an exposed area of  $1\text{ cm}^2$  ( $1\text{ cm} \times 1\text{ cm}$ ). Then, the coupons were anodized in 2 M NaOH aqueous solution with a square pulse potential between the anodic oxidation  $E_t$  and active regions  $E_a$ . They were also anodized at a constant potential of  $E_t$  for comparison. The following process parameters were used: temperature =  $303 \pm 1\text{ K}$ ; duty ratio ( $\alpha = t_t / (t_t + t_a) \times 100$ ) = 91%,  $E_t = 10\text{ V}_{\text{Ag/AgCl}}$  applied for duration  $t_t = 5, 10, 15,$  and  $20\text{ s}$ ;  $E_a = -1.35\text{ V}_{\text{Ag/AgCl}}$  applied for duration  $t_a = 0.5, 1, 1.5,$  and  $2\text{ s}$ ; and, therefore pulse repetition frequencies  $f = 0.18, 0.09, 0.06,$  and  $0.04\text{ Hz}$ , respectively.

The surface morphologies, cross-sectional structures, and chemical element distributions within the anodic films were characterized by scanning electron microscopy (SEM), transmission electron microscopy (TEM), and auger electron spectroscopy (AES), respectively.

The corrosion characteristics of the anodic films were assessed by potentiodynamic and anodic breakdown tests in deaerated 0.1 M NaCl at  $303\text{ K} \pm 1$ . The former was carried out in the potential range from  $-0.2$  to  $+0.3\text{ V}$  vs. the open circuit potential ( $E_{\text{OCP}}$ ) with a scan rate of  $1\text{ mV s}^{-1}$ , and the latter was carried out with a polarizing voltage of  $-1.4\text{ V}_{\text{Ag/AgCl}}$  for  $420\text{ s}$ . The AZ31 alloy of interest was used as the working electrode (WE), platinum wire was used

Table 5.1. Details of cyclic corrosion test (CCT). T and RH represent the operating temperature and relative humidity, respectively.

Operating cycle	Conditions for each step
Salt spray (2 h)	5 wt% NaCl, T = 35°C, RH = 100%
Dry (4 h)	T = 60°C, RH = 25%
Wet (2 h)	T = 50°C, RH = 100%

as the counter electrode (CE), and an Ag/AgCl electrode containing 3.3 M KCl was used as the reference electrode (RE). The cyclic corrosion test (CCT) consisted of a salt-spray step for 2 h, a drying step for 4 h, and a wet step for 2 h was carried out for 3 cycles (24 h). [Table 5.1](#) shows the temperature and relative humidity (RH) in each test step. All the electrochemical experiments were repeated three times and the obtained results were reproducible.

## 5-3. Results and discussion

### 5.3.1. Effects of pulse anodizing on the surface porosity of the anodic film

As seen in Fig. 5.1(a), the specimen anodized at a constant potential (10 V<sub>Ag/AgCl</sub>) contained a number of small- (less than 1 μm) and large-diameter (above 1 μm) pores throughout the surface because of the low Pilling-Bedworth ratio (R<sub>PB</sub>) of Mg (R<sub>PB</sub> = V<sub>oxide</sub> / V<sub>metal</sub> = 0.81). An R<sub>PB</sub> of a valve metal less than 1.00 induces compressive stress at the metal/oxide interface during the anodizing process, and therefore insufficient anodic film is formed to cover the substrate, i.e., the micro-pores are present, even if a sparking do not generated. An effective and continuous resistance to corrosion during immersion requires the maintenance of a compacted protective barrier layer. However, these micro-pores unfortunately act as preferential sites for pitting propagation, and thus the anodic film with its porous structure on the Mg alloy is more susceptible to corrosion than the films on ordinary parts.

However, the conspicuous micro-pores were significantly reduced by the pulse anodization between anodic oxidation and active potentials. Of all the treatments tested, pulse anodization with an  $\alpha$  of 91%,  $f$  of 0.09 Hz, and anodizing time of 600 s was determined to be the most suitable process (Fig. 5.1c). The optimized pulses reduced the pore density by 11 times, from about 7.11% to 0.63%, and decreased maximum pore diameter by 4 times, from about 3.1 to 0.8 μm (Fig. 5.2). The intermittent application of  $E_a$  plays a special role during the pulse anodization, and its significance was already discussed in chapter 4. An active potential,  $E_a$ , applied for duration of  $t_a$  may induce some dissolution of the anodic film

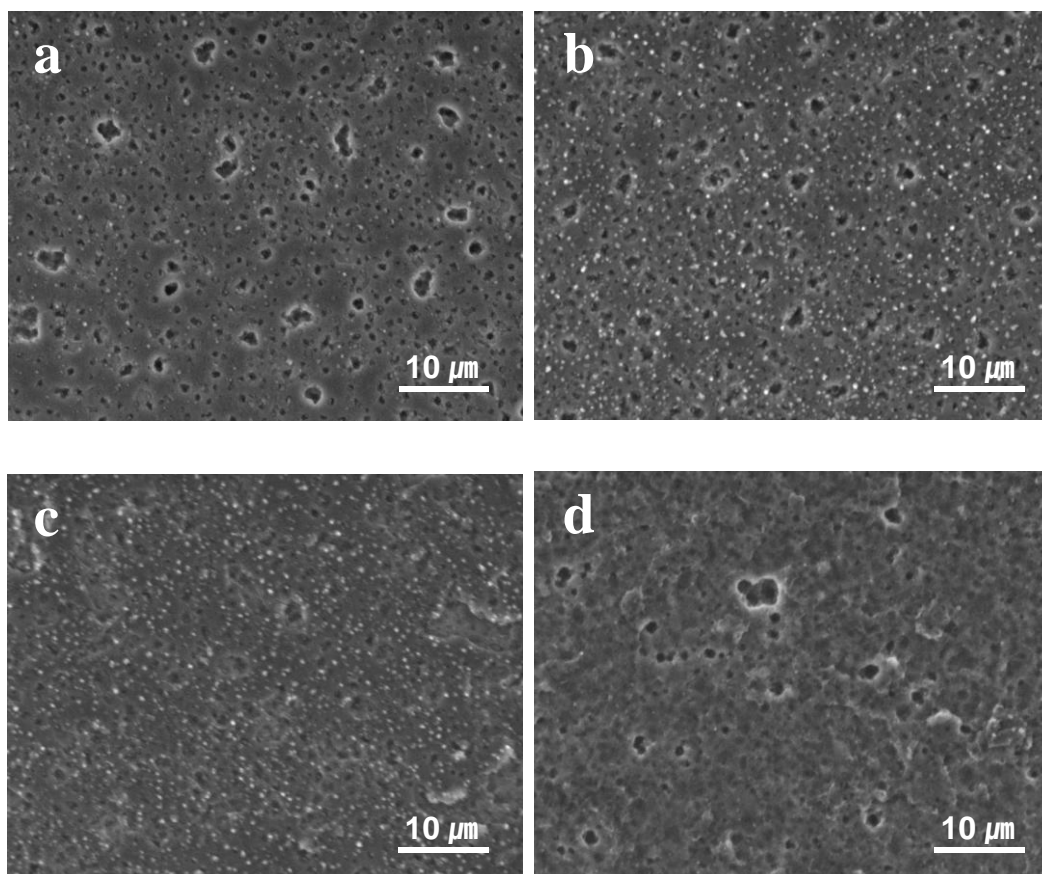


Fig. 5.1. Surface SEM images of the anodic films formed in 2 M NaOH after 600 s of anodization with different conditions: (a) constant potential at 10  $V_{\text{Ag}/\text{AgCl}}$  and (b-d) pulse potential between 10 and  $-1.35 V_{\text{Ag}/\text{AgCl}}$  under constant duty ratio  $\alpha$  of 91% ( $f = 0.04, 0.09,$  and  $0.18$  Hz, respectively). Specimen anodized at an  $f$  of  $0.06$  Hz had a similar surface morphology with that formed at  $0.04$  Hz.

formed on the Mg alloy. In particular, it could remove the weak spots of the anodic film through the edge effect in electricity, i.e. when the flow of potential intercepts an edge or corner, the electricity confines to a smaller volume, and subsequently increase the concentration of  $\text{Mg}^{2+}$  cations near the electrode/electrolyte interface. The dissolved  $\text{Mg}^{2+}$

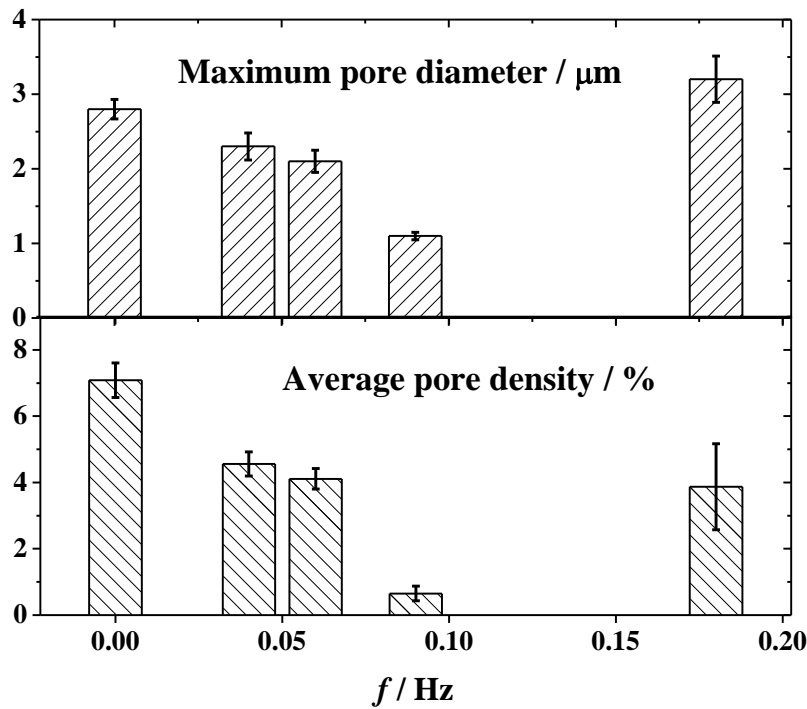


Fig. 5.2. Variation in maximum diameter ( $\mu\text{m}$ ) and average density (%) of the pores formed on the anodic films as a function of pulse repetition frequency  $f$ .

seems to directly contribute to the formation of the anodic film, especially in the micropores, when  $E_t$  is applied for a duration of  $t_t$ . In consequence, the anodic film with the lowest pore diameter and density developed when the rate of the artificial dissolution reaction (under application of  $E_a$  for  $t_a$ ) had achieved a counter-balance with the rate of the anodic film formation reaction (under application of  $E_t$  for  $t_t$ ) over the whole anodizing process.

When the  $\alpha$  and the anodizing period are fixed, the total film formation time (total  $t_t$ ) and anodic dissolution time (total  $t_a$ ) are independent of  $f$ . However, the initial current surge frequency required for adjusting the surface concentration of reactant species to its equilibrium concentration increases with  $f$ , which can increase the film formation kinetics.

The current response during the pulse anodization is made up of two components, i.e., the initial current surge and the subsequent normal diffusion-controlled current (refer to the ref. 11). Moreover, the coincidence of a decrease in Faradic current and an enhancement of non-Faradic current by the increase in  $f$  during the anodization may lead to a less porous anodic film. Hence, the porosity of anodic films and the diameter of micro-pores could be flexibly controlled by altering the  $f$  value. In addition, the lower the film porosity is, the lower the surface roughness is, which might have an additional contribution to the corrosion resistance.

Otherwise, the pore structures present in an oxide film of Mg alloys also can be reduced by adjusting anodizing current applied, i.e., the porosity tends to decrease at a lower current. In this context, Shi et al. suggested the Mg alloys to be anodized at a high current for obtaining a thick anodic film quickly and then at a low current for reducing porosity of the film formed [10]. The concept of the multi-current anodization seems quite similar to the pulse anodization.

Since the formation of an anodic film is the main reaction during the overall anodizing process, the duration  $t_t$  should be much longer than  $t_a$ . Thus, the  $\alpha$  value must be higher than at least 83% ( $t_t/t_a = 5$ ); the higher the value of  $\alpha$ , the higher the value of the  $t_t/t_a$  ratio of the pulses. However, when  $\alpha$  was higher than 98% ( $t_t/t_a = 50$ ), there were no significant differences between the groups of samples anodized under constant and pulse potentials. These results further show that a significant decrease in the surface porosity of anodic film occurs when the number of pulses is about 50–70 in the anodizing process, indicating that  $f$  should be increased with increasing anodizing time.

As shown in Fig. 5.3, depth profile measurements using AES were performed to investigate the effect of the pulse anodization on the changes in element concentrations across

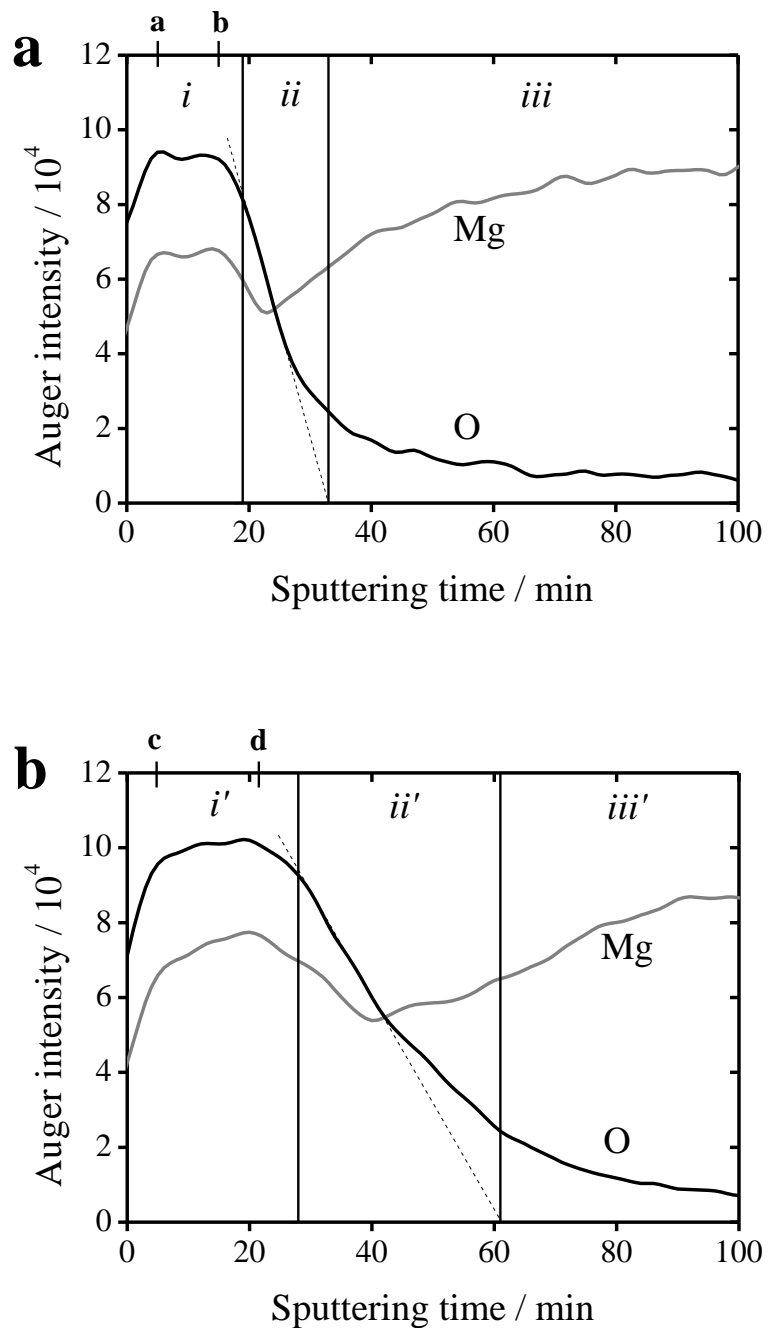


Fig. 5.3. Changes in Auger intensity of elements in the anodic films due to the pulse anodization: (a) constant potential ( $10 \text{ V}_{\text{Ag}/\text{AgCl}}$ ) applied for 10 min and (b) pulse potential applied between 10 and  $-1.35 \text{ V}_{\text{Ag}/\text{AgCl}}$  ( $\alpha = 91\%$ ,  $f = 0.09 \text{ Hz}$ ) for 10 min.



the anodic film. Researchers often use the depth profile measurements to evaluate the absolute thickness of thin film, which depends on the sputtering time and the sputtering rate of the materials, but the real sputtering rate can also be changed by the presence of micropores within the film. Hence, the AES depth profile is not appropriate for estimating the porous anodic film thickness. The obtained depth profiles were divided into three regions for clarity of discussion: (*i, i'*) the anodic film region, (*ii, ii'*) the anodic film/substrate transition region, and (*iii, iii'*) the substrate region. The boundaries of anodic film/substrate transition regions were determined by the intersections of tangent line at the maximum slope with the horizontal line that connects the last peak and the zero level of the O profile (refer to the dotted tangent lines in [Fig. 5.3a and b](#)) [11].

The anodic film formed under the pulse potential shared several features in common with that formed under the constant potential. First, the same initial increases in the Mg and O signals due to the removal of contaminants such as hydrocarbons on the surfaces of the anodic films were found [11–13]. Second, the Mg/O molar ratios in the anodic film region were almost constant with depth and maintained a suitable composition with excess  $\text{Mg}^{2+}$ . Third, Gaussian-shaped distributions of the Mg signal were found in the film/substrate transition region. Thus, the Mg profile exhibited a distinct minimum value in the middle of this region due to the superposition of the substrate and film constituents at the metal/oxide interface [12,13].

However, crucial distinctions were also observed between the two profile patterns, which can be used as indirect evidence in the interpretation of the pore distributions. Several researchers have reported that some complications caused by the topographical effect could be encountered in the analysis of depth profile data [11,14]. For example, Sun et al. reported that the topographical effects of the specimen are likely more prominent for oxides because

of the non-uniform electric charges on oxide surfaces [14]. These experimental results signify that the Auger signal intensities of the anodic film formed on the Mg alloy could be influenced by the surface topography: the higher the intensity of the Auger signals, the lower the porosity of the anodic film. The specimen anodized with the pulse potential afforded a higher Auger signal intensity than the specimen anodized with the constant potential because the anodic film was very tightly bound on the Mg alloy. The profile pattern characteristics in the anodic film regions can also be reasonably explained on the basis of the surface topography effect. For the specimen anodized with the pulse potential, the Auger intensities of the Mg and O signals (c–d) increased with sputtering time in the anodic film region because of the reduced porosity. However, the Auger signal intensities of the specimen anodized with a constant potential (a–b) were invariant with sputtering time, which means that there was no significant morphological change across the anodic film during erosion under  $\text{Ar}^+$  ion bombardment.

As shown in Fig. 5.4(a–b), a number of pores were observed within the anodic film layer at intervals of 1–3  $\mu\text{m}$  for the specimen anodized at a constant potential. However, these pore structures were effectively filled up and disappeared after the pulse anodization between the anodic oxidation and active regions, and the thickness of the anodic film was increased by approximately 60%, from 0.43–0.8 to 0.8–1.2  $\mu\text{m}$  (Fig. 5.4c). In general, the film thickness increased slightly with the number of pulses because of the increase in average current density, but unexpected pits or cavities were also formed on the film surface at 0.18 Hz (Fig. 5.2d). For more detailed discussion, refer to the chapter 4.3.4.

### 5.3.2. Simultaneous formation of the Al enriched oxide layer along with MgO

As is clearly shown in Fig. 5.4(c–e), unusual oxide phase assembly behavior was observed during the growth of anodic film under the pulse potential conditions, which resulted in the formation of an Al-enriched crystalline oxide layer on the outer surface of a MgO layer with a thickness ratio of approximately 1:3. Al is the main alloying element in conventional AZ-type alloys and reduces the surface reactivity of Mg partly by being present in the Mg solid-solution ( $\alpha$ -Mg) and partly by precipitating  $\text{Mg}_{17}\text{Al}_{12}$  ( $\beta$ -phase) along the grain boundaries and/or as a lamellar structure [15]. However, most of the existing Al in the AZ31 alloy forms  $\alpha$ -Mg. Therefore, the formation of the Al-enriched oxide layer could be explained by the simultaneous dissolution of the alloying element of Al in  $\alpha$ -Mg and  $\beta$ -phase when  $E_a$  is applied for duration of  $t_a$  in alkaline solution. Actually, pure Al has approximately four orders of magnitude greater dissolution rate than pure Mg in a certain NaOH solution which indicates that relatively large amount of  $\text{Al}^{3+}$  can be formed and accumulated instantaneously at the electrode/electrolyte interface when  $E_a$  is applied for duration of  $t_a$ . Considering that the anodic film growth occurs mostly on the electrode/electrolyte interface, the dissolved  $\text{Al}^{3+}$  (or both  $\text{Al}^{3+}$  and  $\text{Mg}^{2+}$ ) seems to directly react with  $\text{OH}^-$  to form complex oxide compounds consists of Al and Mg in the outermost part of the anodic film when the applied potential is altered quickly from  $E_a$  to  $E_t$ .

The appearance of the Al enriched superficial oxide layer in the Mg anodic films was of particular interest also in the ref. 16. However, in this case, the aluminate ions are incorporated preferentially in the oxides from the electrolyte additives. Similarly, there have been many previous studies regarding AC modified passivation for various stainless steels which can form superficial chromium (Cr) enriched passive films with high thickness [17,

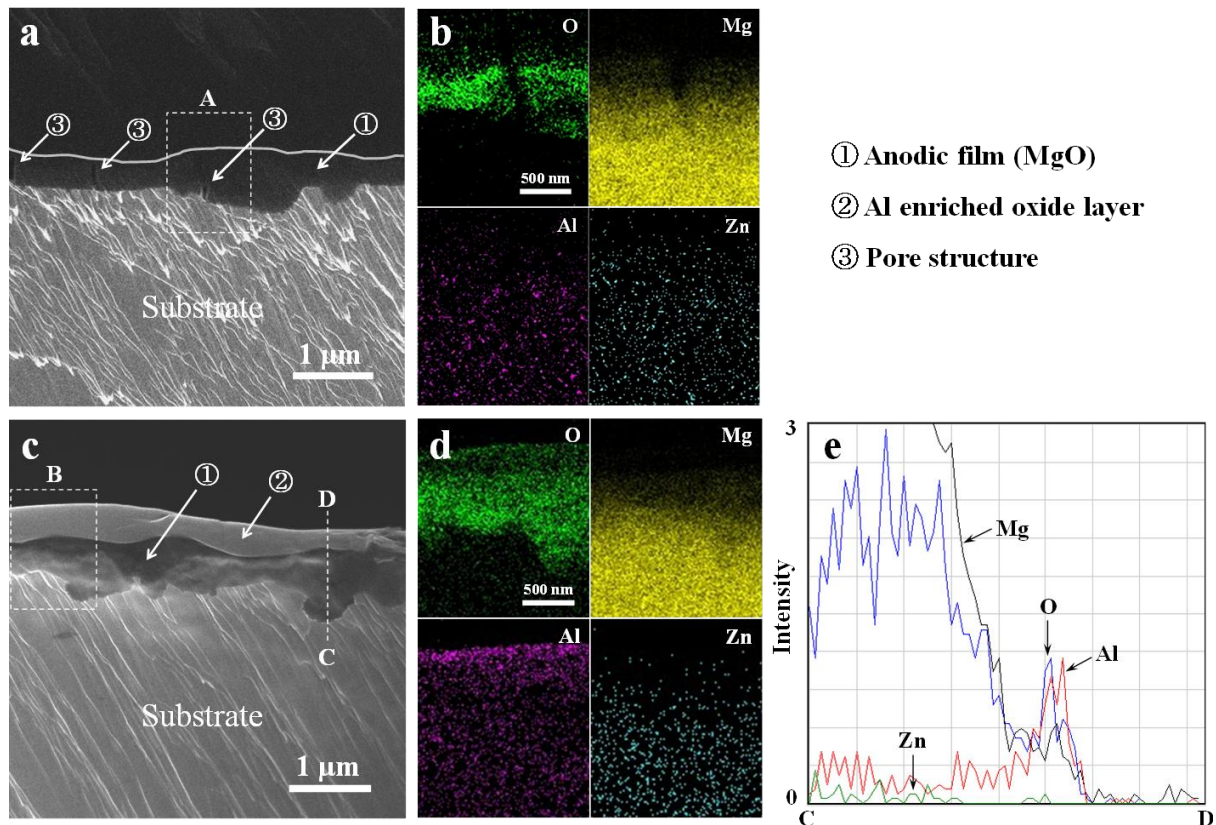


Fig. 5.4. (a) Cross-sectional morphology and (b) X-ray maps of part ‘A’ for the anodic film formed under constant potential ( $10 \text{ V}_{\text{Ag}/\text{AgCl}}$ ) applied for 10 min; and (c) cross-sectional morphology, (d) X-ray maps of part ‘B’, and (e) line-scan profile of part ‘C–D’ for the anodic film formed under pulse potential between 10 and  $-1.35 \text{ V}_{\text{Ag}/\text{AgCl}}$  ( $\alpha = 91\%$ ,  $f = 0.09 \text{ Hz}$ ) for 10 min.

18]. The Cr enriched passive film played a very important role for improving the corrosion resistance of stainless steels after AC modified passivation process.

Several researchers have observed a thick skeletal Al-enriched oxide layer during extended corrosion immersion tests, and this layer can reduce the corrosion susceptibility and further enhance the surface passivation of Mg alloys in chloride-containing neutral

electrolytes [15,19]. However, these Al-enriched oxide layers simply originate from the  $\beta$ -phase that appears along the grain boundaries or as the lamellar structure for the high-Al-content Mg alloys (more than 6%). Although the primary source of the Al-enriched oxide layer formed on the AZ31 alloy during the pulse anodizing is different from that for the layer formed on the high-Al Mg alloys during the corrosion immersion test, this composite anodic film also afforded enhanced corrosion protection for the Mg alloy in a neutral solution [9]. The complete formation mechanism is not fully understood yet. However, the thickness of the Al-enriched oxide layer is expected to increase as the Al content in  $\alpha$ -phase increases and/or the rate of the dissolution reaction increases when  $E_a$  is applied for duration of  $t_a$ .

### ***5.3.3. Effect of pulse anodization on the corrosion characteristics of the anodic film***

As shown in Fig. 5.5, the specimen anodized at an  $f$  of 0.09 Hz had the highest pitting potential  $E_{\text{pit}}$  of  $-1.36 \pm 0.04 \text{ V}_{\text{Ag/AgCl}}$  and lowest corrosion current density  $i_{\text{corr}}$  of  $60 \pm 10 \mu\text{A cm}^{-2}$ . On the other hand, the specimen anodized at constant potential ( $f = 0 \text{ Hz}$ ) had the lowest  $E_{\text{pit}}$  of  $-1.44 \pm 0.03 \text{ V}_{\text{Ag/AgCl}}$  and highest  $i_{\text{corr}}$  of  $190 \pm 20 \mu\text{A cm}^{-2}$ . The pulse anodization enhanced passivation phenomenon and also increased the degree of polarization (DOP) by approximately 3 times. The DOP was defined as the potential change above the open circuit potential required to reach  $1 \text{ mA cm}^{-2}$ . This increase in DOP indicates a highly polarized anodic reaction of the electrode, which means that it is difficult for corrosive ions such as  $\text{Cl}^-$  to penetrate into the micro-pores because of the protective anodic film.

The predominant degradation mechanism of the anodic film directly depends on the initial porosity. Therefore, the seal quality of the anodic films as a function of  $f$  was judged by

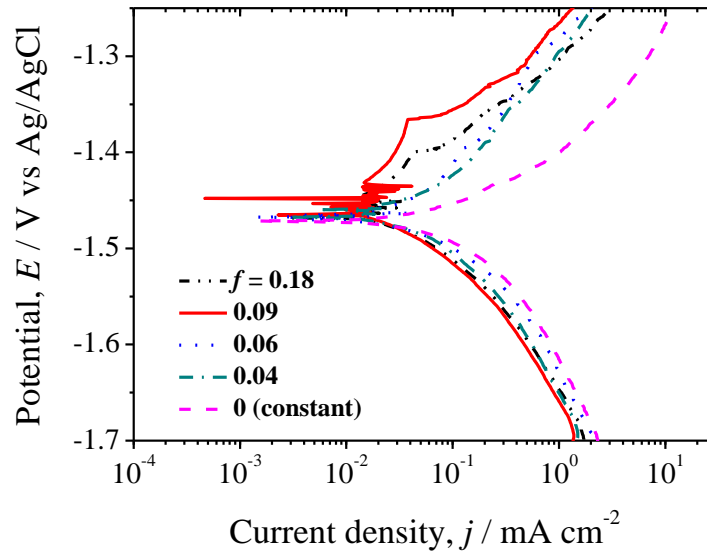


Fig. 5.5. Potentiodynamic polarization curves of the anodic films as a function of pulse repetition frequency  $f$  in 0.1 M NaCl at 303 K. Anodizing time: 600 s.

rapid anodic breakdown tests at 1.4 V<sub>Ag/AgCl</sub> (Fig. 5.6). As shown in Fig. 5.6(a), during the first 10 s, the current density of specimen anodized at  $f$  of 0.09 Hz decreased to approximately 30  $\mu\text{A cm}^{-2}$ , indicating that it still remains in the passive state. However, it increased linearly after 10 s because of the initiation and development of pits within the pores as well as the general corrosion. By contrast, the specimen anodized at a constant potential exhibited the highest current density throughout the whole experiment, especially in the initial step of anodic breakdown ( $\sim 50$  s) since it was in the transpassive state at -1.4 V<sub>Ag/AgCl</sub> (see Fig. 5.5). The decrease in current density due to the pulse anodization was more than an order of magnitude, which means that it is more resistant to pit initiation rather than pit propagation. Therefore, once the pits are initiated, the rate of pit propagation seems to be similar for all specimens. This hypothesis can be demonstrated by the fact that the area of

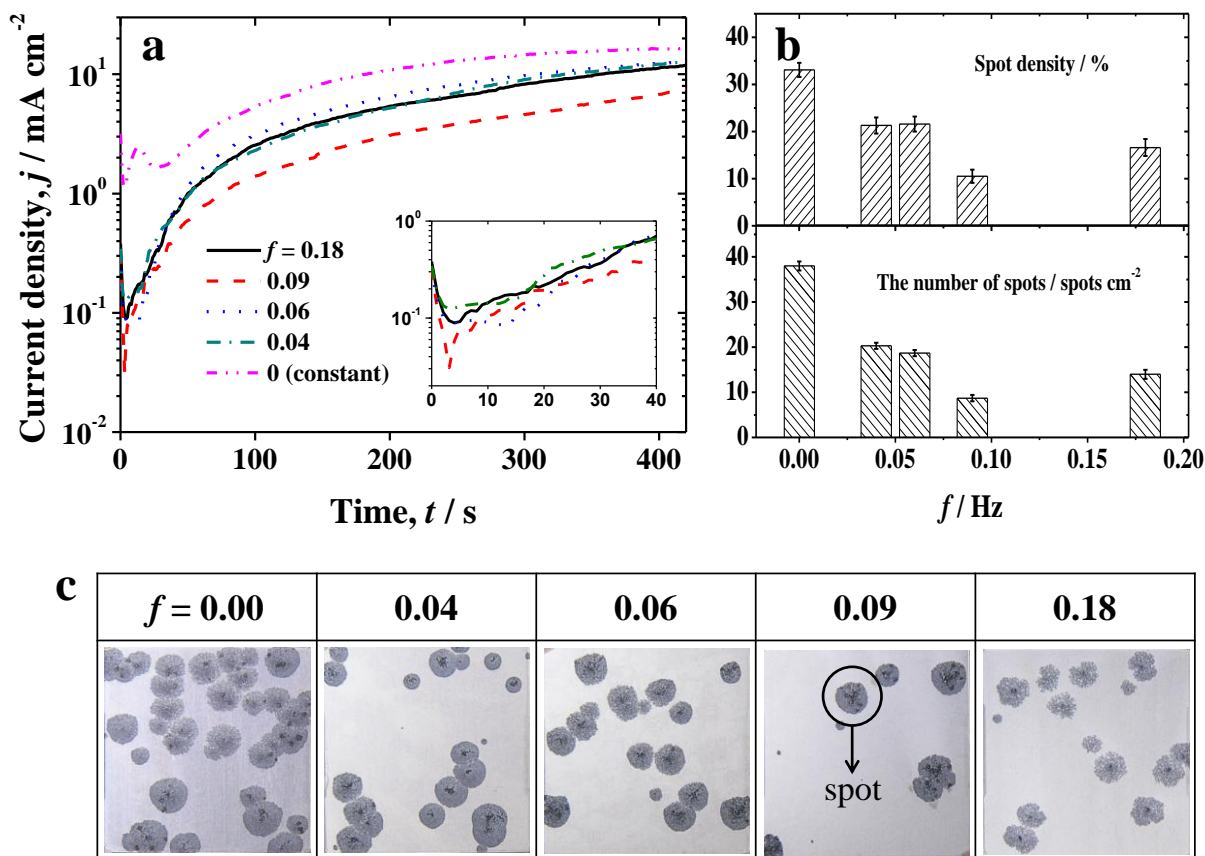


Fig. 5.6. Changes in (a) current density responses, (b) average density and total number of breakdown spots, and (c) surface appearances of the anodic films as a function of the pulse repetition frequency  $f$  during/after the anodic breakdown tests (carried out at  $-1.4 \text{ V}$  vs.  $\text{Ag}/\text{AgCl}$  for 420 s in 0.1 M  $\text{NaCl}$ ).

single breakdown spots was nearly constant for all specimens (Fig. 5.6c). The weak points such as micro-pores in the anodic film have local high currents, which in turn generate a high pH inside the micro-pores. These local areas can be blackened, i.e., they can form breakdown spots, and pitted. The breakdown spot density was decreased approximately 3-fold, and total number of breakdown spots was also decreased approximately 4-fold by the optimized pulse

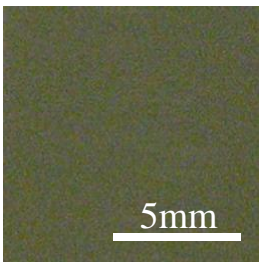




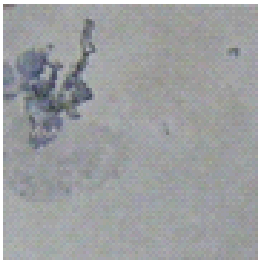
	<b>bare</b> (corroded area = $85.5 \pm 3.2\%$ )	$f = 0.00 \text{ Hz}$ ( $25.8 \pm 4.1\%$ )	$f = 0.09 \text{ Hz}$ ( $6.2 \pm 2.3\%$ )
<b>as -anodized</b>			
<b>after 3 cycles</b>			

Fig. 5.7. Surface appearances of the anodic films after cyclic corrosion tests carried out for 24 h in a 5 wt% NaCl environment. Instead of continuous salt-spray testing, cyclic corrosion testing was performed to ensure comparability within 24 hrs of the tests. In general, only salt-spray setup (100–200 hrs) is used for the corrosion testing of Mg alloys.

anodization ( $f = 0.09 \text{ Hz}$ , Figs. 5.6b, 5.6c).

The cyclic corrosion tests (CCT) results agreed well with the potentiodynamic and anodic breakdown test results (Fig. 5.7). Severe corrosion was observed on the bare AZ31 alloy after 24 h. However, the pulse anodization mitigated the corroded area by more than an order of magnitude, from about  $85.5 \pm 3.2\%$  to  $6.2 \pm 2.3\%$ .

In summary, the optimized pulse anodization process between the anodic oxidation and active region potentials led to both the decrease in film porosity and the formation of Al



enriched superficial oxide layer. Both will decrease the corrosion susceptibility of Mg alloys in chloride containing neutral environments. However, considering that the pitting is still forced to occur preferentially through the film pores even if the Al enriched oxide layer has formed, decreasing the film porosity seems more important for enhancing pitting corrosion resistance.

## 5-4. Conclusions

In this chapter the effect of the pulse anodization repetition frequency  $f$  on the microstructure and corrosion characteristics of AZ31 alloy were examined under a constant duty ratio  $\alpha$  of 91%. An insufficient anodic film containing many micro-pores was formed under a constant potential ( $10 \text{ V}_{\text{Ag}/\text{AgCl}}$ ), but the number of such micro-pores was effectively reduced by the pulse potential between the anodic oxidation ( $10 \text{ V}_{\text{Ag}/\text{AgCl}}$ ) and active regions ( $-1.35 \text{ V}_{\text{Ag}/\text{AgCl}}$ ) of the AZ31 Mg alloy. The significant reduction in surface porosity occurred when the number of pulses is around 50–70 in the anodization process. In particular, the best pulse conditions were an  $\alpha$  of 91%, an  $f$  of 0.09 Hz, and an anodizing time of 600 s. In addition, interestingly, an Al-enriched oxide layer was developed on the outer surface of the anodic film in a thickness ratio of approximately 1:3. This phenomenon may occur when the alloying element Al in the AZ31 alloy is sufficiently dissolved together with Mg when the active potential is applied, thereby forming the Al-enriched oxide layer on the outer surface of anodic film when the potential is altered to the anodic oxidation region. The external Al-rich oxide layer can enhance the corrosion protection of the Mg alloy in a neutral solution. In consequence, the pitting potential increased from  $-1.44 \pm 0.03$  to  $-1.36 \pm 0.04 \text{ V}_{\text{Ag}/\text{AgCl}}$  and the corrosion current density decreased from  $190 \pm 20$  to  $60 \pm 10 \mu\text{A cm}^{-2}$ , resulting in a decrease in the corroded area of approximately 3–4 times after anodic breakdown and salt spray tests.

## REFERENCES

- [1] J. Zhang, C. Wu, *Recent Patents on Corrosion Science* 2 (2010) 55.
- [2] O. Khaselev, D. Weiss, and J. Yahalom, *J. Electrochem. Soc.* 146 (1999) 1757.
- [3] E.A. Carter, T.F. Barton, and G.A. Wright, *Surface Treatment 99: 4<sup>th</sup> International Conference on Computer Methods and Experimental Measurements for Surface Treatment Effects*, Assisi, Italy (1999) p. 169.
- [4] Z. Shi, G. Song, and A. Atrens, *Corros. Sci.* 47 (2005) 2760.
- [5] H. Ardelean, I. Frateur, S. Zanna, A. Atrens, and P. Marcus, *Corros. Sci.* 51 (2009) 3030.
- [6] V. Tchervyakov, G. Gao, J. Bombach, A.P. Pchel'nikov, and G. Cole, *Magnesium Technology 2000*, TMS (2000) p. 143.
- [7] R.F. Zhang, D.Y. Shan, R.S. Chen, and E.H. Han, *Mater. Chem. Phys.* 107 (2008) 356.
- [8] C. Blawert, V. Heitmann, W. Dietzel, H.M. Nykyforchyn, and M.D. Klakiv, *Surf. Coat. Technol.* 200 (2005) 68.
- [9] Y.I. Choi, S. Salman, K. Kuroda, and M. Okido, *Corros. Sci.* 63 (2012) 5.
- [10] Z. Shi, G. Song, and A. Atrens, *Corros. Sci.* 48 (2006) 1939.
- [11] T.S. Sun, D.K. Mcnamara, J.S. Ahearn, J.M. Chen, B. Ditchek, and J.D. Venables, *Appl. Surf. Sci.* 5 (1980) 406.
- [12] X. Wang, X. Zeng, S. Yao, G. Wu, and Y. Lai, *Mater. Charact.* 59 (2008) 618.
- [13] A. Bakkar, V. Neubert, *Corros. Sci.* 47 (2005) 1211.
- [14] P.H. Holloway, *J. Electron Spectrosc. Relat. Phenom.* 7 (1975) 215.
- [15] A. Pardo, M.C. Merino, A.E. Coy, F. Viejo, R. Arrabal, and S. Feliú Jr., *Electrochim. Acta* 53 (2008) 7890.
- [16] O. Khaselev, J. Yahalom, *J. Electrochem. Soc.* 145 (1998) 190.

- [17] G.L. Song, C.N. Cao, and H.C. Lin, *Corros.* 49 (1993) 271.
- [18] H. He, T. Zhang, C. Zhao, K. How, G. Meng, Y. Shao, and F. Wang, *J. Appl. Electrochem.* 39 (2009) 737.
- [19] M.C. Merino, A. Pardo, R. Arrabal, S. Merino, P. Casajús, and M. Mohedano, *Corros. Sci.* 52 (2010) 1696.

**VI. Synergistic Corrosion Protection for AZ31 Mg  
alloy by Anodizing and Stannate Post-sealing  
Treatments**

## 6-1. Introduction

The world has seen rapid growth in demand for magnesium (Mg) and its alloys in diverse lightweight applications (modern automotive, electronics, and aerospace industries, etc) over the last few decades. Among these applications, the use of various Mg alloy components inside a vehicle can lead to an overall weight-savings of around 10%, which in turn leads to a composite (city/highway) fuel-savings of roughly 6% with no major changes to the design [1]. In addition, the Mg alloys have high damping capacities, superior dimensional stability, good recyclability, good electromagnetic interference shielding properties, and good biocompatibility [1–5]. However, their obvious advantages have been, unfortunately, tarnished by the low standard electrode potential ( $-2.37 \text{ V}_{\text{SHE}}$ ) and high corrosion susceptibility of Mg under certain service conditions.

Mg is a highly reactive (active) element in that it tends to readily lose its two valence electrons and further react with chloride ( $\text{Cl}^-$ ) to obtain stable configurations. Chloride ion intrusion and moisture absorption induce a breakdown of the naturally formed Mg oxide/hydroxide and, eventually, an exposed  $\alpha$ -phase will undergo degradation to form hydromagnesite ( $\text{Mg}_5(\text{CO}_3)_4(\text{OH})_2 \cdot 4\text{H}_2\text{O}$ ) and nesquehonite ( $\text{MgCO}_3 \cdot 3\text{H}_2\text{O}$ ) [6–8]. Moreover, the Mg dissolves readily in dilute acids to form aquated Mg ions ( $\text{Mg}^{2+}$ ) along with  $\text{H}_2$  gas. In this context, many different types of anodizing processes have been developed to produce Mg alloys with anti-corrosion abilities and mitigate the various types of corrosion damage. However, the soft and porous anodized coatings obtained on Mg alloys are comprised of water-soluble hydroxide and oxide, which means that it is difficult to achieve effective protection against corrosion for industrial applications using only this process. Furthermore, the pore structures of the anodized coating can act as preferential sites for pitting corrosion.

Thus, the predominant corrosion mechanism for anodized Mg alloys directly depends on the initial surface porosity [9–11].

Thus far, porous anodized coatings have often been used as under-coatings to provide better corrosion resistance and adhesion for various organic finishes [12]. However, the porous and rough surfaces can limit the utilization of spray-type top-coating systems. In this context, we suggested a novel anodizing technique that remarkably limits the formation of micro-pores on the anodized coatings, thereby improving their corrosion resistance [11]. Otherwise, post-treatments (e.g., sealing treatments) must be considered as a critical step for achieving corrosion resistance for porous anodized Mg alloys. These sealing treatments are often carried out in boiling water or solutions containing silicate/phosphate to deposit low-solubility salts in the pore structures after reactions between Mg and the anions [13,14]. Song et al. [14] suggested an irreversible electroless E-coating procedure for anodized ZE41 Mg alloy carried out in a solution containing 71–82 wt% water, 16–26 wt% epoxy resin, and 1.3 wt% titanium dioxide. However, the pH of the electroless E-coating solution was nearly neutral, so the dipping process could only last for 10 s. Hence, the porous structure of the anodized coating was not completely sealed after the dipping process alone. Nevertheless, the post-sealing procedure decreased the corrosion current density and increased polarization resistance by approximately three orders of magnitude compared to the as-anodized coupon. However, it is not clear as to whether this coating will provide long-term corrosion protection. Fujita et al. [15] reported a procedure for liquid-phase deposition (LPD) of a TiO<sub>2</sub> film in which pure Mg is dipped in a base solution containing 0.01 kmol m<sup>-3</sup> (NH<sub>4</sub>)<sub>2</sub>TiF<sub>6</sub> and 0.2 kmol m<sup>-3</sup> H<sub>3</sub>BO<sub>3</sub> at 353 K. However, the LPD process is time consuming, which limits its industrial applications. In particular, it required more than 24 h to deposit a 0.5-μm-thick TiO<sub>2</sub> layer, and the film formed was not sufficient to enhance the corrosion resistance of Mg

alloy because of the formation of micro-cracks. Organic and sol-gel coatings have also been applied to improve the corrosion protection of anodized or micro-arc oxidized Mg alloys [16,17].

The chemical conversion coating system for Mg alloys in a stannate bath have already been examined by many researchers [18,19]. In this study, we investigate the feasibility of sealing the porous structure of an as-anodized AZ31 Mg alloy with a stannate post-treatment and measure the resultant corrosion characteristics.



## 6-2. Experimental

The chemical composition of the commercial AZ31 Mg alloy used as a substrate was 3.0 wt% Al, 1.0 wt% Zn, 0.43 wt% Mn, 0.01 wt% Si, < 0.01 wt% Cu, < 0.001 wt% Ni, 0.003 wt% Fe, and the balance Mg. The Mg sheets were ground with fine-grained emery paper up to 2000 grit, polished with 0.05- $\mu\text{m}$   $\text{Al}_2\text{O}_3$  powder, ultrasonically cleaned in ethanol for 3 min, and quickly dried in cool air. The working area of each specimen ( $1 \text{ cm}^2$ ) was limited with hydrophobic adhesive masking tape. The specimens were then anodized in a 2 M NaOH aqueous solution (200 ml) at 303 K with a constant potential of  $10 V_{\text{Ag}/\text{AgCl}}$  for 10 min [11]. After the anodization, the specimens were immersed for 2–60 min in a post-treatment solution containing 0.4 M sodium stannate 3-hydrate ( $\text{Na}_2\text{SnO}_3 \cdot 3\text{H}_2\text{O}$ ) at 350 K that was stirred. An identical stannate post-treatment was also carried out on bare AZ31 coupons (as-polished, 0.05- $\mu\text{m}$   $\text{Al}_2\text{O}_3$  powder) for the same periods of time. After the specimens were withdrawn from the stannate post-treatment solution, they were immediately rinsed with running de-ionized water, dried in cool air using a handheld dryer, and reserved in a vacuum desiccator until the morphological, chemical, and electrochemical characterizations.

After the stannate post-treatment, the surface and cross-sectional microstructures and corresponding chemical compositions of the specimens were characterized by performing field emission scanning electron microscopy (FE-SEM), energy dispersive X-ray spectroscopy (EDS), and X-ray photoelectron spectroscopy (XPS). An Al  $K\alpha$  (1486.6 eV) X-ray source was used and the obtained binding energies (BEs) were charge-corrected with respect to the signal from the residual carbon (C 1s) present on the stannate post-treated layer, which was set at BE = 284.6 eV.

The electrochemical characteristics of the specimens were assessed by performing

Table 6.1. Details of cyclic corrosion test (CCT). T and RH represent operating temperature and relative humidity, respectively.

Operating cycles	Conditions of each step
Salt spray (2 h)	5 wt% NaCl, T: 35°C, RH: 100%
Dry (4 h)	T: 60°C, RH: 25%
Wet (2 h)	T: 50°C, RH: 100%

electrochemical impedance spectroscopy (EIS) and linear sweep voltammetry (LSV) in an aerated 0.1 M NaCl aqueous solution at  $298 \pm 1$  K with a typical electrochemical cell consisting of three-electrodes. In the cell, the specimens of interest served as the working electrodes (WEs) with a Pt wire as the counter electrode (CE) and a Ag/AgCl electrode (saturated 3.3 M KCl) as the reference electrode (RE). In the EIS measurement, the real and imaginary parts of the impedance of the electrochemical cell were evaluated for 24 h at 1 h intervals, where the applied voltage was the open-circuit potential ( $E_{OCP}$ ) over a nominal frequency range of from  $10^5$  down to  $10^{-1}$  Hz with an amplitude of 10 mV. The LSV was carried out in a potential range from -0.2 to 0.5 V vs.  $E_{OCP}$ , after stabilization of  $E_{OCP}$  for 30 min, and the corresponding currents were recorded at scan rate set to  $1 \text{ mV s}^{-1}$ . A method for determining pitting potential  $E_{pit}$  is described elsewhere [11]. Cyclic corrosion tests (CCT) were performed according to the JASO (Japanese Automobile Standard) M609-91 method [20]. The details of each setup for the CCT were described in Table 6.1. All experiments were

repeated at least five times and were found to be reproducible; thus, only representative data are shown in this chapter.

## 6-3. Results and discussion

### 6.3.1. Effect on surface and cross-sectional structures of as-anodized coating

As shown in Fig. 6.1(a), the as-anodized coating formed on AZ31 contained many cylindrical open pores not exceeding 3  $\mu\text{m}$  in diameter. The formation of this open-pore structure is attributed to the fact that the molar volume of MgO ( $V_{\text{oxide}}$ ) is  $11.3 \text{ cm}^3 \text{ mol}^{-1}$ , whereas that of metallic Mg ( $V_{\text{metal}}$ ) is  $14.0 \text{ cm}^3 \text{ mol}^{-1}$  [11,13]. A molar volume ratio

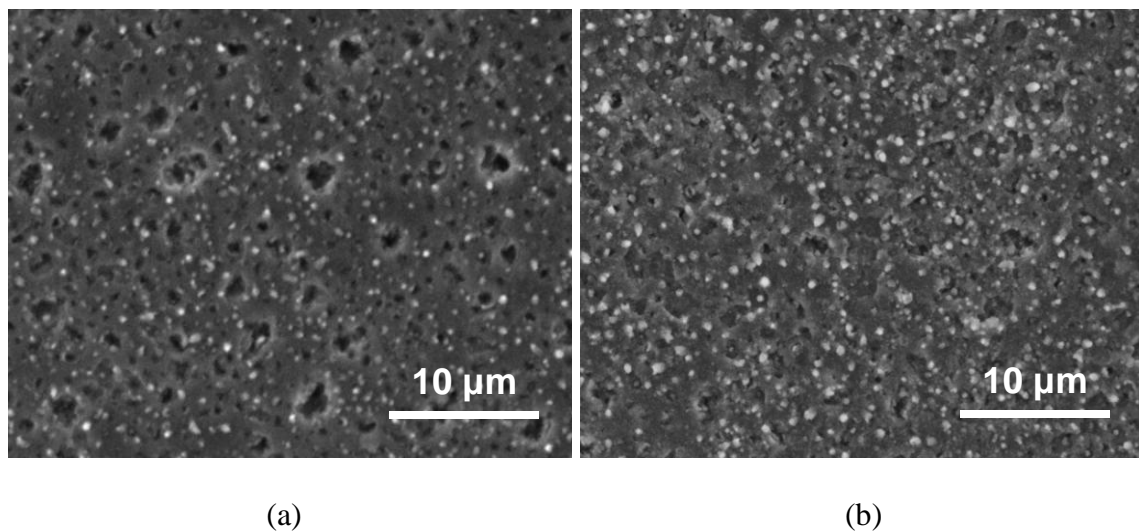
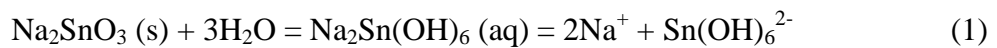


Fig. 6.1. Surface SEM images of the as-anodized coating after stannate post-treatment: (a) as-anodized (at 10  $V_{\text{Ag/AgCl}}$  for 10 min), (b) stannate post-treated for 10 min. The white dots, whether stannate post-treated or not, represent protrusions on the surface of the coating. Pore depth of the as-anodized coating was measured to be approximately 0.3–0.5  $\mu\text{m}$ .

( $V_{\text{oxide}}/V_{\text{metal}}$ ) of valve metals less than 1.00 increases the tensile stress at the metal/oxide interface during anodization, and insufficient oxide film is developed to cover the substrate containing the open pores. These pore structures cannot provide effective resistance against corrosion and act as preferential sites for pitting corrosion [11,21,22].

As shown in Fig. 6.1(b), however, these open pores were effectively filled up after the stannate post-treatment. Thus, the as-anodized coating was smoothed, and the surface porosity was significantly reduced. Although the microstructural features of the as-anodized coating were considerably changed by the post-treatment, there was no significant change in surface color: the surface colors of both coatings were white. When a polished AZ31 alloy was immersed in the same post-treatment solution for several minutes, the surface color also changed to white. It should be noted that the post-treatment solution containing stannate salts itself is changed from colorless to white by the precipitate produced when the temperature is increased to 350 K. In an aqueous solution,  $\text{Na}_2\text{SnO}_3$  (s) exists mostly in the form of  $\text{Na}_2\text{Sn}(\text{OH})_6$  (aq) and dissociates to produce  $\text{Na}^+$  and  $\text{Sn}(\text{OH})_6^{2-}$ . The  $\text{Sn}(\text{OH})_6^{2-}$  anions are instantly formed by reaction (1) because of their high stability at pH values above 8 [23,24]:



However, as shown in Fig. 6.2, the pH value of the stannate solution was decreased from about 12.9 to 10.4 when the temperature increased from 298 K to 350 K, since the water and base dissociation system which is in equilibrium (i.e., a steady-state where association balances dissociation) is subjected to the absorption of heat: the pH value typically decreases with temperature in most solutions [25,26], and the solution temperature compensation

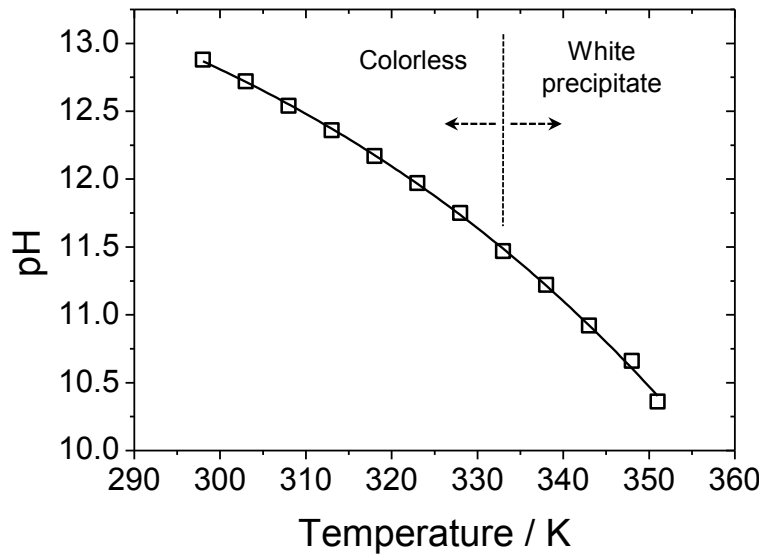
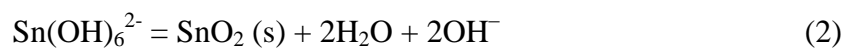


Fig. 6.2. Changes in pH of the stannate post-treatment solution with temperature.

coefficient for the stannate solution was measured to be  $-0.048 \text{ }^{\circ}\text{C}$  (negative slope,  $\Delta\text{pH}/\Delta T$ ). However, the equilibrium solubility of Sn (IV) in aqueous solution tends to decrease as the pH decreases from 11.7 to 9 [24]. Moreover, crystalline  $\text{SnO}_2$  (s) was proved to be the most stable phase at pH values less than 11.7, while a double salt of  $\text{SnO}_2$  and NaOH (i.e.  $\text{Na}_2\text{Sn}(\text{OH})_6$ ) is most stable at pH values greater than 11.7 [24,27]. These facts suggest that the gelatinous  $\text{SnO}_2$  precipitates in the solid-state, which have a white color, can be nucleated and grow in the stannate solution, especially at high temperatures on the surface of the anodized coating, according to the reaction (2).



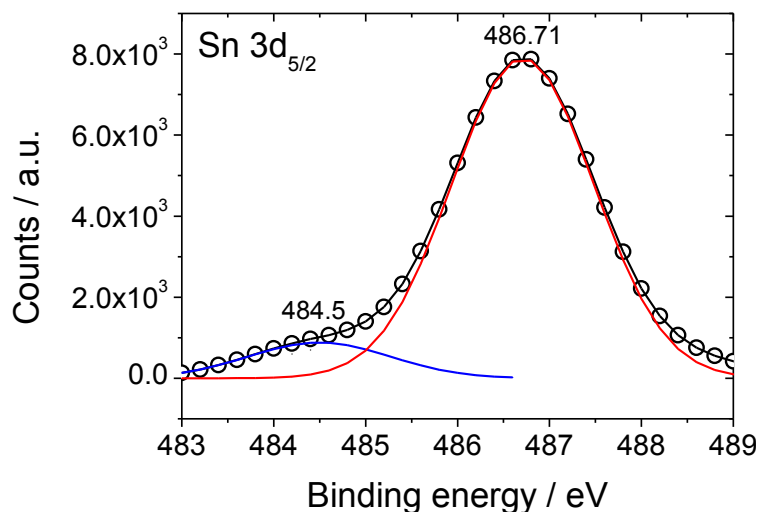


Fig. 6.3. High-resolution Sn  $3d_{5/2}$  XPS spectrum (circles) and decomposed components (solid line) of the stannate post-treated coating.

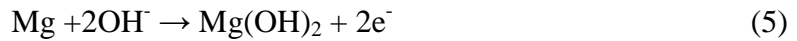
In brief, the supersaturated state is attributed to the changes in the solubility of  $\text{SnO}_2$  with the solution temperature, and the colorless and transparent stannate solution started to change to white at around 330 K (pH 11.5, see Fig. 6.2). These considerations fully explain why the crystalline  $\text{SnO}_2$  from the stannate solution supersaturated with oxides is deposited on the as-anodized coating during the post-treatment. The  $\text{SnO}_2$  might easily bond with anodic films through ligand-surface OH reactions and redox reactions [28].

XPS measurements were then performed to accurately investigate the effect of the stannate post-treatment on the chemical composition of the superficial layer covering the open-pore structure of the as-anodized coating. As shown in Fig. 6.3, the Sn  $3d_{5/2}$  spectra were composed of two peaks. The main peak centered at higher binding energy (BE, 486.71 eV) was solely attributed to the presence of  $\text{SnO}_2$  [29], whereas the minor peak at a lower BE (484.5 eV) was caused by the presence of metallic Sn [30]. This result suggests that  $\text{SnO}_2$  is

the main species present on the surface of the as-anodized coating after the stannate post-treatment. In addition, the presence of a small amount of metallic Sn could be attributed to the potential gradient between the Mg and SnO<sub>2</sub>. Therefore, there may be a local electrochemical system on the as-anodized coating, especially inside the pore structures, during the stannate post-treatment. Under given experimental conditions, the following redox reaction can describe the metallic Sn deposition: a cathodic reaction



and an anodic reaction



The Mg dissolution process (anodic) may result in the accumulation of Mg<sup>2+</sup> in the electrolyte, whereas the Sn deposition process (cathodic) may reduce Sn(OH)<sub>6</sub><sup>2-</sup> to Sn<sup>0</sup> on the specimen surface.

This outer compact layer of SnO<sub>2</sub> made up approximately 30% of the total thickness of the stannate post-treated coating (Fig. 6.4). In our previous work, the thickness of the as-anodized coating was about 0.8 μm and many pores were observed at intervals of 1–3 μm [11]. However, this pore structure was effectively filled up and covered by the SnO<sub>2</sub>, increasing the total coating thickness to about 1.2 μm. Furthermore, the uniform thickness of the final post-treated coating indicates successful leveling of any irregularities such as the initial pore structure of the as-anodized coating. The variation of the Sn/O ratio with depth



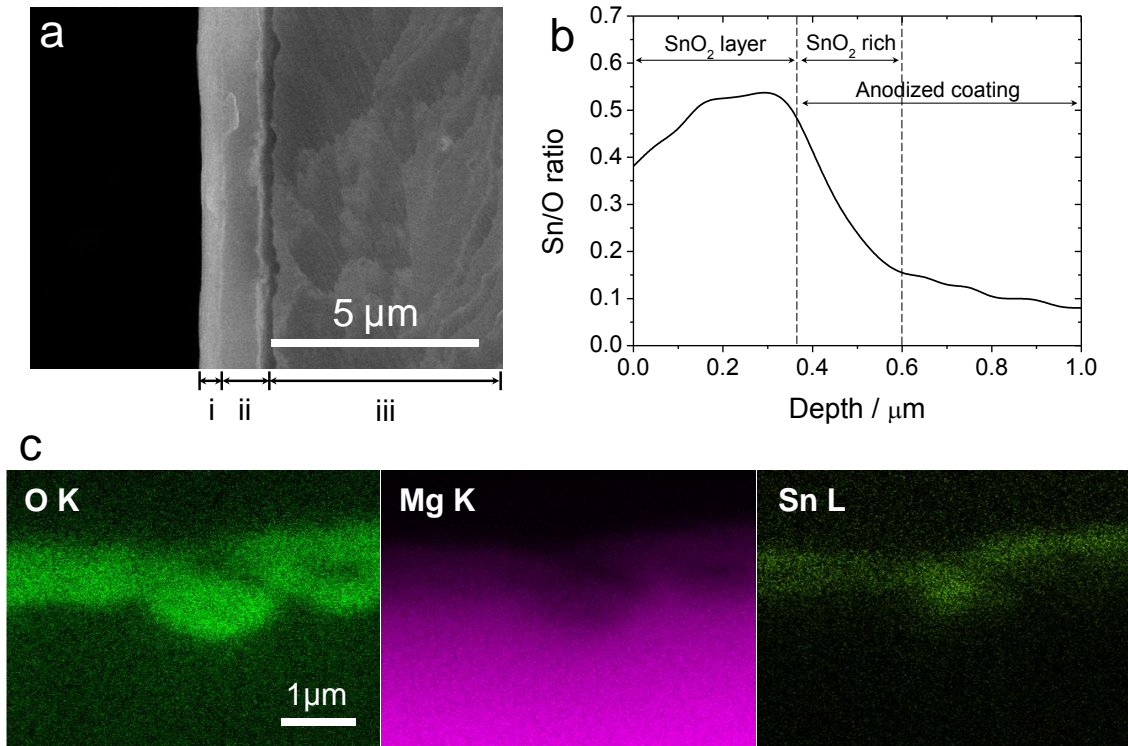


Fig. 6.4. (a) Cross-sectional morphology (i, SnO<sub>2</sub> layer; ii, anodized coating; and iii, AZ31 substrate), (b) Changes in Sn/O ratio with depth, and (c) EDS elemental mapping of the coupon stannate post-treated for 10 min.

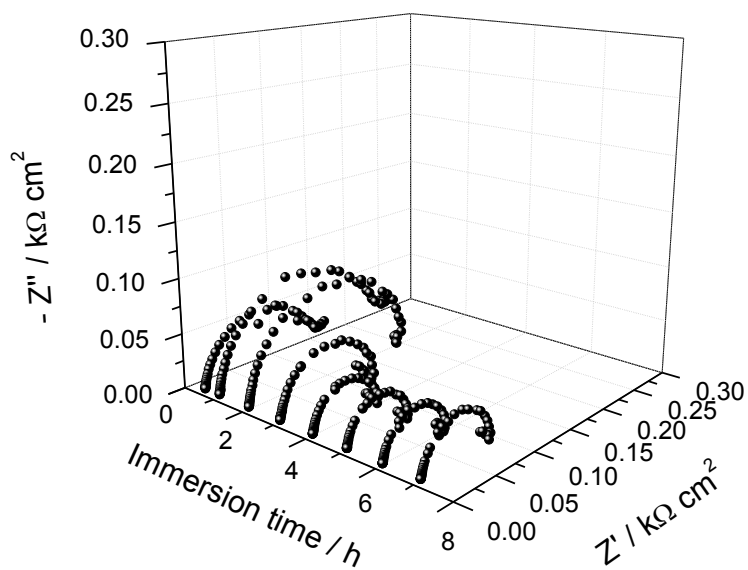
clearly revealed that the thickness of the SnO<sub>2</sub> layer is approximately 0.4 μm; the Sn/O ratio of this layer is almost constant (0.4–0.5) with depth. However, the ratio decreased sharply between 0.4 and 0.6 μm (SnO<sub>2</sub>-rich layer) and then became saturated (anodized coating). This observation implies that the SnO<sub>2</sub> not only forms the superficial layer of the as-anodized coating but also nucleates and grows inside of the pore structures. The direct crystallization of SnO<sub>2</sub> within the pores may enhance the strength of the adhesion of the SnO<sub>2</sub> layer to the as-anodized coating. The adhesion strength of the SnO<sub>2</sub> layer was qualitatively determined by

the amount of coating that was removed by cellophane tape peel tests. No SnO<sub>2</sub> residues were visible on the tapes after these tests.

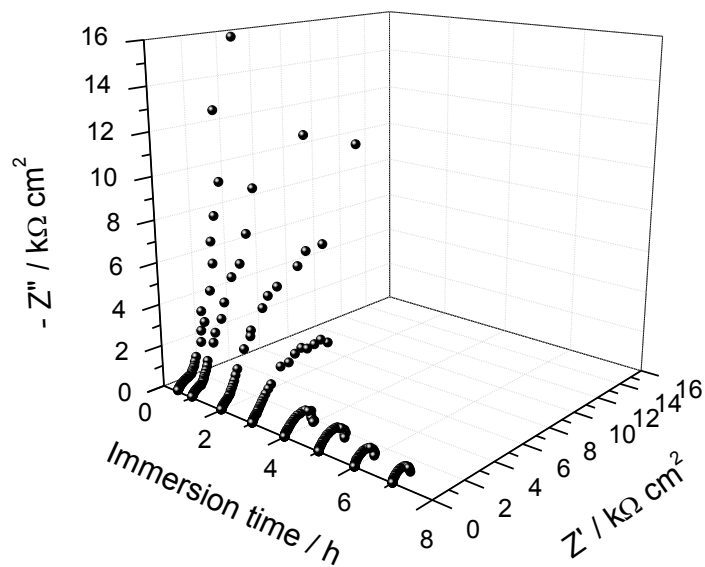
### ***6.3.2. Effect on electrochemical characteristics of anodized coating***

EIS measurement was carried out in order to investigate the effect of the stannate post-treated layer on the corrosion kinetics across the anodized coating and the substrate interface with the AZ31 Mg alloy. As shown in Fig. 6.5(a), the complex impedance plots of the as-anodized sample showed ordinary distributions based on a simple equivalent circuit typically appearing in as-anodized Mg alloys [11]. Moreover, an inductive loop emerged at low frequencies (below 3 Hz) after 2 h of immersion, which did not appear for the sample with the stannate post-treated coating. This inductive behavior is known to arise in most cases from a non-steady-state response of continuously corroding metals [31–34].

By contrast, as shown in Fig. 6.5(b), mass transport impedance corresponding to an impermeable boundary condition (restricted linear diffusion) was found for the sample with the stannate post-treated coating upon initial immersion. This gives rise to an almost vertical line in the complex plane as the frequency decreases, which corresponds to an ideal capacitance dispersion. The appearance of this ideal capacitor is responsible for the extremely small charge leakage at the coating/electrolyte interface, which means that slow corrosion kinetics was achieved in this exposure environment [35,36]. Only a small steady-state dc current flows in this ideal capacitor system because of the approximately constant ratio of redox sites and lack of a detectable electrochemical potential gradient [37]. However, the potential drop accelerates the motion of the counterions, so that an electrochemically active layer is developed. In this context, the complex impedance plots gradually develop tilted lines



(a)



(b)

Fig. 6.5. Measured Nyquist plots of (a) the as-anodized coating and (b) the coating after stannate post-treatment for 10 min for different immersion times in 0.1 M NaCl solution at 298 K.

instead of the vertical line as a result of the slow permeation of corrosive ions through the coating layer. Hence, the mass transport impedance was gradually moved to a low-frequency domain with immersion time, which is a departure from the ideal capacitor behavior. The blocked linear diffusion behavior completely disappeared after 4 h of immersion, presumably because the permeation of the corrosive ions into the coating/substrate interface of the stannate post-treated sample had been completed.

Understanding the mass transport impedance of this electrolyte/coating/substrate cell is quite important, since the ionic diffusion through the coating layer is the rate-determining process at low frequencies. This mass transport reaction within the coating obeys the linearized Fick's law when the effect of migration is neglected. The linear form of Fick's equation is (Fig. 6.6),

$$J_p(x) = -D \frac{\partial^2 \Delta c(x)}{\partial x^2} \quad (8)$$

where  $J_p$  is the flux of the corrosive species at  $0 \leq x \leq L$ ,  $c$  is the concentration of corrosive species at  $x$ , and  $D$  is the pseudo diffusion coefficient.

Therefore, the expressions for  $\Delta J_p$  at  $x = 0$  and  $L$  are as follows [36],

$$J_p[x = 0] = -D \frac{\partial \Delta c[x = 0]}{\partial x} = k_1 \Delta \Gamma - k_2 \Delta c[x = 0] \quad (9)$$

$$J_p[x = L] = -D \frac{\partial \Delta c[x = L]}{\partial x} = k_3 \Delta c[x = L] + k_4 \Delta E \quad (10)$$

where  $\Gamma$  is the concentration of corrosive species adjacent to the metal substrate,  $E$  is the

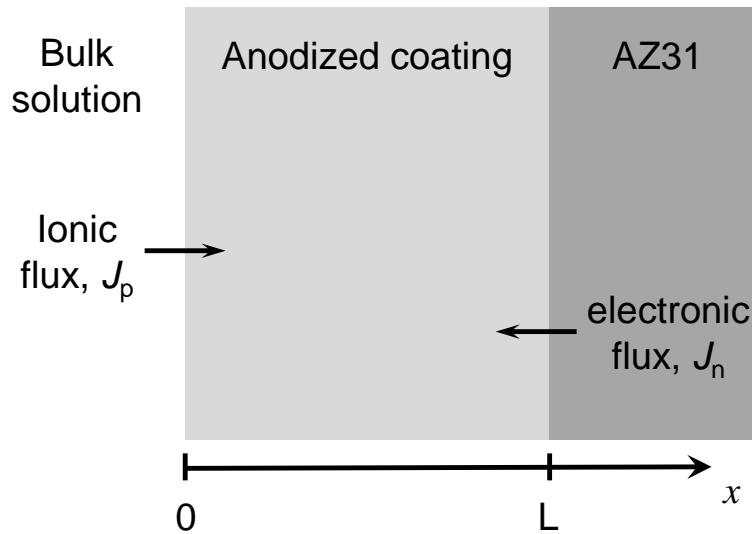


Fig. 6.6. Schematic of the solution/coating/substrate cell system [31].

potential drop at the anodized coating/electrolyte interface, and each  $k$  value ( $k_1-k_4$ ) is a rate constant.

Equations (9) and (10) give the generalized boundary conditions for Fick's equation (8), and the permeation of corrosive ions through a coating layer is effectively blocked when  $k_3 = k_4 = 0$  [36]. Furthermore, the restricted diffusion impedance dominates the low frequencies of the complex plane when the  $k$  values are close to zero [36,37]. This suggests that the ideal capacitor system of the post-treated coating allows a slow steady-state dc current flow that is caused by the extremely small charge leakage upon initial exposures. Therefore, the coating initially acted as an effective corrosion barrier. However, the corrosion protection afforded by this barrier formed on as-anodized coating was minimal at long immersion times, i.e., more than approximately 10 h.

Curve fitting of the Nyquist plot with an appropriate equivalent electric circuit is the most common method for analyzing the specimens' impedance. However, the observed

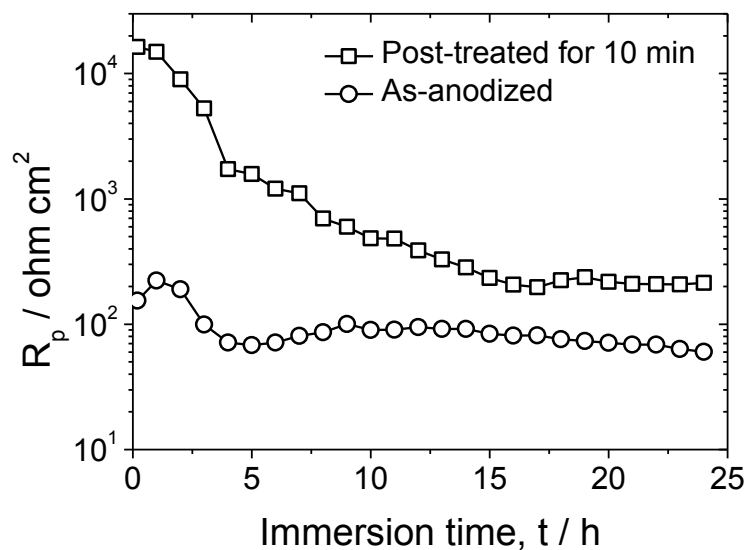
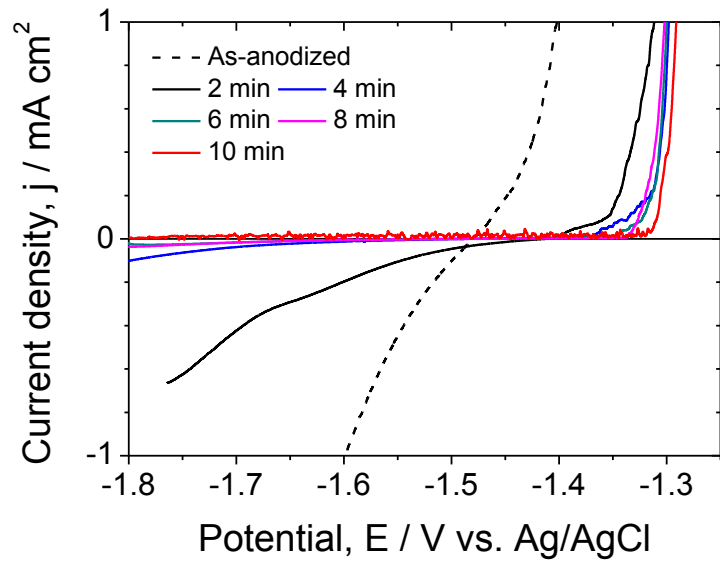
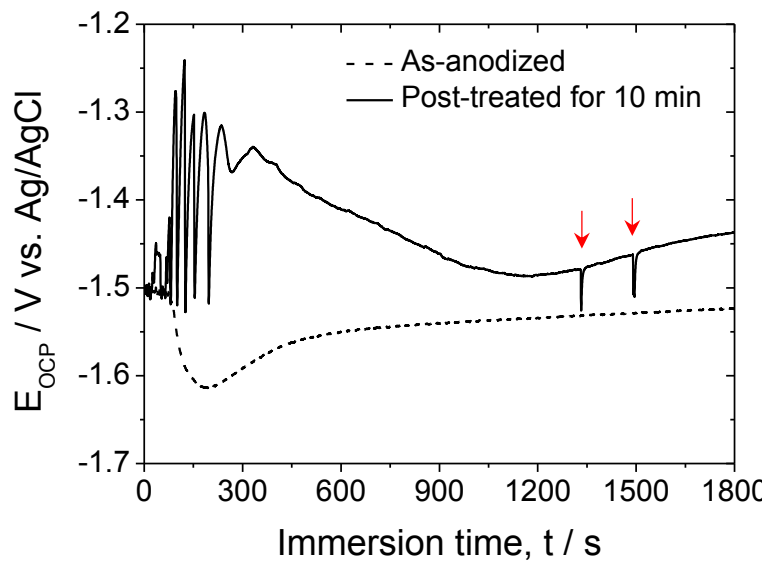


Fig. 6.7. Changes in polarization resistance  $R_p$  (i.e. the sum of all resistances) of the as-anodized and stannate post-treated (10 min) coatings with the immersion time in 0.1 M NaCl solution at 298 K.

Nyquist plot for each specimen revealed different time constants and different Warburg elements for different immersion times. Therefore, a Bode plot was considered in order to directly contrast the polarization resistance  $R_p$ , i.e., the sum of all resistances, of the stannate post-treated coating with that of the as-anodized coating. As shown in Fig. 6.7, a fluctuation of  $R_p$  (0–12 h) at the coating/electrolyte interface of the as-anodized coating was found. This fluctuation is presumably due to the series of corrosion, absorption of corrosion products, and removal of corrosion products in the pore structures. It was then gradually decreased with the immersion time. By contrast, the stannate post-treated coating afforded a much higher  $R_p$  (10–100 fold) during the initial immersion (0–4 h) because of the effective blockage of linear



(a)



(b)

Fig. 6.8. Change (a) in anodic and cathodic polarization behaviors of the as-anodized coating with the stannate post-treatment time and (b) in  $E_{\text{OCP}}$  with the immersion time in 0.1 M NaCl solution at 298 K. There was no repeatability to the behaviors marked by red arrows.

diffusion at low frequencies, which results in the retardation of mass transport into the coating. The  $R_p$  then gradually decreased with immersion time but maintained its critical value after 15 h of immersion and afforded a value about threefold higher than that of the as-anodized coating even after 24 h of immersion.

Linear sweep voltammetry was then conducted in order to investigate the effect of the stannate post-treatment on the overall corrosion characteristics of the as-anodized coating. As shown in Fig. 6.8(a), the stannate post-treatment gradually allowed highly polarizable cathodic behavior to occur, so that the Tafel slope increased with post-treatment time. This means that smaller currents were observed for larger cathodic overpotentials as the post-treatment time increased. The possible cathodic reaction in neutral aqueous solutions is the hydrogen reduction reaction, i.e.,  $2\text{H}_2\text{O} + 2\text{e}^- \rightarrow \text{H}_2 + 2\text{OH}^-$ . Finally, the hydrogen reduction reaction of a sample that was stannate post-treated for 10 min behaved almost ideally in the potential range between -1.8 and -1.32  $\text{V}_{\text{Ag}/\text{AgCl}}$  ( $\text{SnO}_2$  has a large hydrogen overpotential). Thus, the currents remained constant (almost zero) and were independent of the cathodic potential. The cathodic reaction is very important for sustaining pitting since both the anodic and cathodic reactions take place on the metal surface in a practical situation. Without the cathodic reaction, no further growth of pits can occur. This phenomenon can be explained by the compensation of electric double-layer charging current with the potential change in the cell, which results in infinite charge-transfer resistance at  $E_{\text{OCP}}$  ( $R_{\text{ct}} \rightarrow \infty$ ). This result is consistent with the EIS data (see Fig. 6.5b).

Beyond the cathodic part of the sweep (at approximately -1.32  $\text{V}_{\text{Ag}/\text{AgCl}}$ ), polarization arose on the electrode surface, causing the current density to depart from the ideal straight line. In particular, lower currents were obtained at higher anodic overpotentials. Thus, the sample stannate post-treated for 10 min exhibited a higher  $E_{\text{corr}}$  (-1.32  $\text{V}_{\text{Ag}/\text{AgCl}}$ ) and  $E_{\text{pit}}$  (-1.30



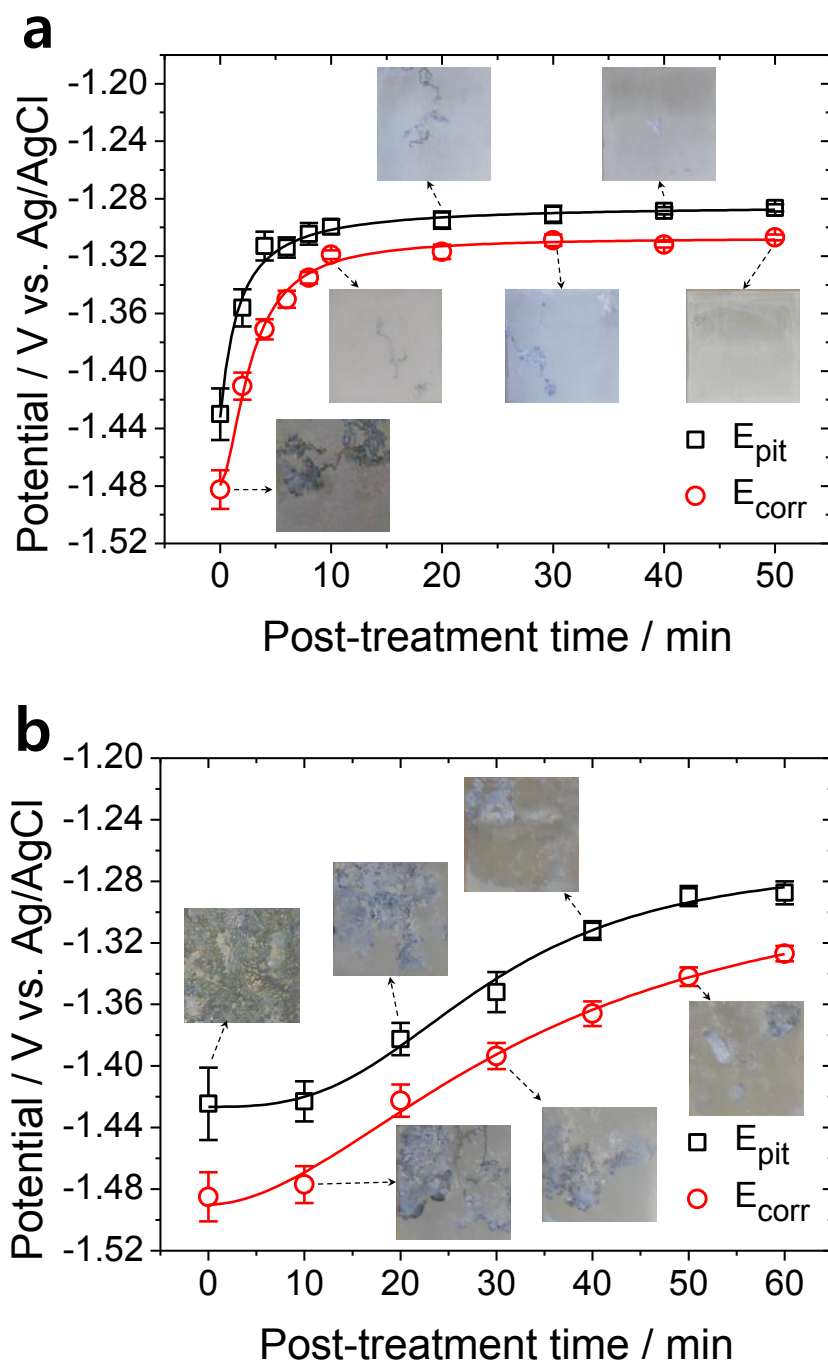


Fig. 6.9. Change in pitting potential  $E_{pit}$  and corrosion potential  $E_{corr}$  with the stannate post-treatment time on the (a) as-anodized coating (at 10 V<sub>Ag/AgCl</sub> for 10 min) and (b) polished surface (0.05- $\mu$ m Al<sub>2</sub>O<sub>3</sub> powder). Optical microscopy images of the specimens (1  $\times$  1 cm) after cyclic corrosion tests for 24 h are included.

$V_{\text{Ag/AgCl}}$ ) than the as-anodized sample ( $E_{\text{corr}} = -1.48 V_{\text{Ag/AgCl}}$ ,  $E_{\text{pit}} = -1.43 V_{\text{Ag/AgCl}}$ ). This is attributed to the presence of the 0.3–0.4  $\mu\text{m}$  thick  $\text{SnO}_2$  layer, which is a highly corrosion-resistant material over a neutral pH range electrolyte that covers up the open-pore structure of the as-anodized coating. However, both the  $E_{\text{corr}}$  and  $E_{\text{pit}}$  values measured for the stannate post-treated samples were far from what one might expect from a  $\text{SnO}_2$  coating [38,39]. This result reveals that the filling effect by the  $\text{SnO}_2$  is far from perfect so that the  $\text{SnO}_2$  coating obtained is actually quite porous. Hence, as shown in Fig. 6.8(b), the  $E_{\text{OCP}}$  of the post-treated coating was increased with the intermittent potential drops (fast wave potentials) occurring upon initial immersion ( $\sim 300$  s), while the  $E_{\text{OCP}}$  of the as-anodized coating decreased with time. These fast wave potentials occurring upon initial immersion arise from the competing influence of two electrochemical reactions occurring simultaneously on the stannate post-treated coating, i.e., the rapid oxidation reaction of the as-anodized coating and the corrosion protection effect of the  $\text{SnO}_2$  superficial layer. This result signifies that the  $\text{SnO}_2$  layer did not fully cover the as-anodized coating after 10 min of stannate post-treatment, so that a small area of the as-anodized coating was still exposed to the NaCl solution. Nevertheless, the stannate post-treated coating afforded a higher steady-state  $E_{\text{OCP}}$  than the as-anodized coating upon immersion. When in the steady-state, the potential difference across the working and reference electrodes was constant ( $\Delta E_{\text{OCP}}$  vs.  $t \approx 0$ ). In contrast, the decrease in  $E_{\text{OCP}}$  of the as-anodized coating upon initial immersion ( $\sim 200$  s) results from the continuous degradation of the MgO. However, the  $E_{\text{OCP}}$  increased after 200 s because of the precipitation of corrosion by-products over the as-anodized coating, especially within the open-pore structures. Finally, the  $E_{\text{OCP}}$  reached a steady-state level after 1000 s.

The  $E_{\text{corr}}$  and  $E_{\text{pit}}$  values of stannate post-treated coating improved with treatment time up to 10 min to nearly their maximum values, but no further improvement (or only small

improvements) occurred afterward (Fig. 6.9a). This experimental result indicates that longer post-treatments did not allow the SnO<sub>2</sub> particles to nucleate further even in the small areas where the SnO<sub>2</sub> coverage was insufficient, i.e., unfilled pore spaces, with stannate post-treatment times beyond 10 min. The results of the cyclic corrosion test agree well with the linear sweep voltammetry results: there was no significant difference between the specimens subjected to stannate post-treatments for 10 and 50 min after 3 cycles. The corrosion protection effect of the stannate post-treatment in NaCl solution was also observed for bare AZ31 Mg alloys (as-polished, Fig. 6.9b). However, approximately 50 additional minutes were required to reach similar  $E_{\text{corr}}$  and  $E_{\text{pit}}$  values to those of the as-anodized specimen subjected to stannate post-treatment. These results imply that selective reactions such as the ligand-OH reaction and redox reaction can accelerate the deposition of SnO<sub>2</sub> on the anodized Mg coating layer. Therefore, the pre-anodizing procedure is highly necessary for the stannate post-treatment of Mg alloys. Hence, the thickness of the SnO<sub>2</sub> layer and the resultant corrosion behavior of the coupons seem to have improved no further after the anodized coating was covered by the SnO<sub>2</sub> layer.

## 6-4. Conclusions

In this chapter, the effects of stannate post-treatment on the surface sealing and corrosion characteristics of as-anodized AZ31 Mg alloy were examined. AZ31 coupons were anodized at  $10 \text{ V}_{\text{Ag}/\text{AgCl}}$  for 10 min in a 2 M NaOH aqueous solution at 298 K and subsequently immersed in a 0.4 M sodium stannate 3-hydrate ( $\text{Na}_2\text{SnO}_3 \cdot 3\text{H}_2\text{O}$ ) solution at 350 K under stirring. After 10 min of the stannate post-treatment, the open-pore structures commonly found on the as-anodized Mg alloy were mostly covered and leveled by the  $\text{SnO}_2$  layer. The stannate post-treatment solution supersaturated with oxide at high temperature seems to contribute to the nucleation and growth of  $\text{SnO}_2$  layer on the as-anodized Mg alloy. This  $\text{SnO}_2$  superficial layer made up approximately 30 % ( $\approx 0.4 \mu\text{m}$ ) of the total coating thickness and effectively occupied the voids within the porous as-anodized coating. After the surface sealing, the stannate post-treated coating exhibited mass transport impedance with impermeable boundary condition (restricted linear diffusion) during the initial immersion for 4 h. Thus, the electrode showed ideal capacitance dispersion at low frequencies. This phenomenon is attributed to the extremely small charge leakage at the coating/electrolyte interface. Thus, slow corrosion kinetics was achieved in this exposure environment. In particular, the stannate post-treated coating afforded 10–100 fold higher  $R_p$  values during the initial immersion, and the  $R_p$  values were still higher even after 24 h. Interestingly, the cathodic currents remained almost zero during the linear potential sweep measurement and were independent of the cathodic overpotential. This phenomenon can be explained by the compensation of electric double-layer charging current with the potential change in the cell, which results in infinite charge-transfer resistance at  $E_{\text{OCP}}$ . As a consequence, the stannate post-treated coupons exhibited a higher corrosion potential  $E_{\text{CORR}}$  ( $-1.32 \text{ V}_{\text{Ag}/\text{AgCl}}$ ) and pitting

potential  $E_{\text{pit}}$  ( $-1.30 \text{ V}_{\text{Ag/AgCl}}$ ) than the as-anodized coupons ( $E_{\text{corr}} = -1.48 \text{ V}_{\text{Ag/AgCl}}$ ,  $E_{\text{pit}} = -1.43 \text{ V}_{\text{Ag/AgCl}}$ ).

## REFERENCES

- [1] U.S. Congress, Office of Technology Assessment (OTA), DIANE Publishing, Washington, DC: GPO, 1995.
- [2] H.K. Lim, D.H. Kim, J.Y. Lee, W.T. Kim, D.H. Kim, *J. Alloys Compd.* 468 (2009) 308.
- [3] T. Lei, C. Ouyang, W. Tang, L. Li, L. Zhou, *Surf. Coat. Technol.* 204 (2010) 3798.
- [4] C.H. Anja, G. Petra, S. Michael, J.U. Peter, *Acta Biomaterialia* 5 (2009) 162.
- [5] L. Zhao, C. Cui, Q. Wang, S. Bu, *Corros. Sci.* 52 (2010) 2228.
- [6] H.P. Godard, W.B. Jepson, M.R. Bothwell, R.L. Lane, Wiley and Sons, New York, 1967.
- [7] R. Lindstrom, J.-E. Svensson, L.-G. Johansson, *J. Electrochem. Soc.* 149 (2002) B103.
- [8] M. Jönsson, D. Persson, D. Thierry, *Corros. Sci.* 49 (2007) 1540.
- [9] V. Tchervyakov, G. Gao, J. Bombach, A.P. Pchel'nikov, G. Cole, *Magnesium Technology 2000*, TMS (2000) 143.
- [10] R.F. Zhang, D.Y. Shan, R.S. Chen, E.H. Han, *Mater. Chem. Phys.* 107 (2008) 356.
- [11] Y.I. Choi, S. Salman, K. Kuroda, M. Okido, *Corros. Sci.* 63 (2012) 5.
- [12] O. Khaselev, D. Weiss, J. Yahalom, *J. Electrochem. Soc.* 146 (1999) 1757.
- [13] C. Blawert, W. Dietzel, E. Ghali, G. Song, *Adv. Eng. Mater.* 8(6) (2006) 511.
- [14] G. Song, *Surf. Coat. Technol.* 203 (2009) 3618.
- [15] R. Fujita, M. Sakairi, T. Kikuchi, S. Nagata, *Electrochim. Acta* 56 (2011) 7180.
- [16] H. Duan, K. Du, C. Yan, F. Wang, *Electrochim. Acta* 51 (2006) 2898.
- [17] A.L.K. Tan, A.M. Soutar, I.F. Annergren, Y.N. Liu, *Surf. Coat. Technol.* 198 (2005) 478.
- [18] M.A. Gonzalez-Nunez, C.A. Nunez-Lopez, P. Skeldon, G.E. Thompson, H. Karimzadeh, P. Lyon, and T.E. Wilks, *Corros. Sci.* 37(11) (1995) 1763.
- [19] C.S. Lin, H.C. Lin, K.M. Lin, W.C. Lai, *Corros. Sci.* 48 (2006) 93.

- [20] JASO M 609-91, The Society of Automotive Engineers of Japan, Inc., 1991.
- [21] Z. Shi, G. Song, A. Atrens, *Corros. Sci.* 47 (2005) 2760.
- [22] H. Ardelean, I. Frateur, S. Zanna, A. Atrens, P. Marcus, *Corros. Sci.* 51 (2009) 3030.
- [23] L. Duro, M. Grivé, E. Cera, C. Doménech, J. Bruno, SKB-TR-06-17, Svensk Kärnbränslehantering AB, 2006.
- [24] D. Rai, M. Yui, T. Schaef, A. Kitamura, *J. Solution Chem.* 40 (2011) 1155.
- [25] “pH temperature compensation.” yokogawa.com. May 13, 2009 (October 1, 2012) <<http://www.yokogawa.com/us/is/downloads/pdf/analytical/TECHNOTES/TNA0924.pdf>>.
- [26] “Temperature and pH measurement.” all-about-ph.com. n.p. 2012 (October 1, 2012) <<http://www.all-about-ph.com/ph-measurement.html>>.
- [27] B. Lothenbach, M. Ochs, D. Hager, *Radiochim. Acta* 88 (2000) 521.
- [28] A. Suzuki, M. Tada, T. Sasaki, T. Shido, Y. Iwasawa, *J. Mol. Catal. A: Chem.* 182–183 (2002) 125.
- [29] P.A. Grutsch, M.V. Zeller, T.P. Fehlner, *Inorg. Chem.* 12(6) (1973) 1431.
- [30] Tery L. Barr, *J. Vac. Sci. Technol. A* 9(3) (1991) 1793.
- [31] M. Keddam, O.R. Mattos, H. Takenouti, *J. Electrochem. Soc.* 128 (1981) 257.
- [32] D.D. Macdonald, *Electrochim. Acta* 35 (1990) 1509.
- [33] L. Bai, B.E. Conway, *Electrochim. Acta* 38(14) (1993) 1803.
- [34] R.D. Armstrong, M. Henderson, *J. Electroanal. Chem.* 39 (1972) 81.
- [35] J. Bisquert, G.G. Belmonte, F.F. Santiago, P.R. Bueno, *J. Electroanal. Chem.* 475 (1999) 152.
- [36] G. Láng, J. Bácskai, G. Inzelt, *Electrochim. Acta* 38 (6) (1993) 773.
- [37] J.P. Diard, B. Le Gorrec, C. Montella, *J. Electroanal. Chem.* 471 (1999) 126.

- [38] R. Díaz, I. Díez-Pérez, P. Gorostiza, F. Sanz, and Joan R. Morante, *J. Braz. Chem. Soc.* 14(4) (2003) 523.
- [39] M. Jayalakshmi, N. Venugopal, K. Phani Raja, M. Mohan Rao, *J. Power Sources* 158 (2006) 1538.



## **VII. Summary and Future work**

## 7-1. Summary

1. In chapter 3, the effect of electrolyte temperature on the corrosion characteristics of wrought AZ31B, AZ61, and as-cast AZ91 Mg alloys in 0.1 M NaCl was examined. At high temperatures of around 328 K (55 °C), AZ61 showed the highest corrosion potential, lowest corrosion current density, highest polarization resistance, and slowest pitting propagation kinetics. These results can be attributed to the microstructure of AZ61 which contains nano-scale  $\beta$ -phase particles effectively dispersed within the grains.
2. In chapter 4, anodizing was carried out for the AZ31 Mg alloy which exhibits the lowest corrosion resistance with square pulses of different duty ratios between the anodic oxidation (10 V<sub>Ag/AgCl</sub>) and active regions (-1.35 V<sub>Ag/AgCl</sub>). A duty ratio of 91 for 600 s afforded the highest  $E_{\text{pit}}$  of -1.366 V<sub>Ag/AgCl</sub>, lowest  $i_{\text{corr}}$  of 17.06  $\mu\text{A cm}^{-2}$ , and highest  $R_p$  of 0.46 k $\Omega \text{ cm}^2$  in 0.1 M NaCl. Furthermore, the micro-pores were effectively filled with anodic films by the pulse potentials, thus the surface porosity was decreased approximately 11 times than that obtained with a constant potential.
3. In chapter 5, optimal conditions for the pulse anodizing were found to be a duty ratio of 91%, a frequency of 0.09 Hz, and an anodizing time of 600 s. The pulse anodizing caused a remarkable 11-fold decrease in the surface porosity and a 1.6-fold increase in the film thickness from those obtained under a constant potential. Furthermore, a complex oxide compound consisting of Al and Mg was formed on the outer surface of MgO, which improves the corrosion resistance of the Mg alloy in a neutral solution.

4. In chapter 6, stannate post-treatment was conducted on the as-anodized AZ31 Mg alloy in 0.4 M sodium stannate 3-hydrate ( $\text{Na}_2\text{SnO}_3 \cdot 3\text{H}_2\text{O}$ ) at 350 K. It effectively leveled the porous anodized coating by depositing a  $\text{SnO}_2$  superficial layer with a thickness of 0.4  $\mu\text{m}$ . As a consequence, the stannate post-treatment afforded higher  $R_p$ ,  $E_{\text{corr}}$ , and  $E_{\text{pit}}$  values throughout the immersion in 0.1 M NaCl.

## 7-2. Future Work

This study demonstrated the possibility of enhancing corrosion resistance of magnesium alloys by means of the novel pulse anodizing technique controlled between the anodic oxidation and active regime potentials. This anodizing, however, is a highly sensitive process for adjusting those potentials, i.e. the potential values must be altered with the alloy and electrolyte types, etc. Moreover, the thickness of anodic films formed is too thin (around 2  $\mu\text{m}$ ) to achieve desired corrosion resistance in a neutral solution. Therefore, it is obvious that this anodizing is not capable of industrial applications. However, I would like to note that the transpassive region (around 3 V vs. Ag/AgCl) of magnesium alloys develops porous, but thick corrosion products on its surface along with the vigorous hydrogen evolution which unfortunately do not have proper corrosion resistance. With this, I expect a dense and thick anodic film if the pulse anodizing is conducted between the potential high enough to generate sparks (near 150 V) and the transpassive regime potential. It is predictable because the sparks preferentially concentrate on the sites where the anodic film is insufficiently formed during the anodizing. Further, the composition of the anodic film formed while applying transpassive potential could be modified by the spark generation.

Concerning the stannate post-sealing treatment, I believe it is very advantageous post-treatment method because it can seal almost all the pores within the anodic films. In this study, the stannate post-sealing treatment was carried out just for the anodic film under the pulse potential condition which has the low thickness. However, this post-treatment might be fully capable even if the film thickness is higher than 10–20  $\mu\text{m}$  and the porous structure could be sufficiently sealed by the  $\text{SnO}_2$  which has a high overvoltage for the hydrogen generation reaction in a neutral solution.

## **VIII. Acknowledgements**

Firstly, I am cordially grateful to my academic supervisor, Prof. Dr. Masazumi Okido, and my second academic supervisor, Prof. Dr. Kensuke Kuroda, for giving me the opportunity to study at the Surface & Interface Engineering Laboratory, introducing in the magnesium world, and for their appreciated supervision, valuable guidance, and supports to follow the right path for my research works. Special thanks go to 1. Prof. Dr. Masazumi Okido, 2. Kazuhiko Noda, 3. Yasutoshi Iriyama, 4. Ryoichi Ichino, and 5. Kensuke Kuroda for being judges of my thesis committee.

My deep gratitude to Dr. Sung-Pyo Cho who is now belongs to Seoul National University for his valuable expertise and help in bringing TEM analysis to its completion.

Many thanks to Dr. Dai Yamamoto and Mr. Takuhiro Eguchi for their help to adapt quickly to my new life in Japan as an international student.

Sincere appreciation to my academic mentor, Prof. Dr. Chan-Jin Park, just for his presence itself. Special Thanks to Prof. Dr. Seong-Jong Kim for referring me to Prof. Dr. Masazumi Okido and offering unstinting supports to fulfill my dream of studying abroad.

The financial support from the Japanese Government (Monbukagakusho: MEXT) and Hori Science and Arts Foundation are acknowledged for helping my focus on the research.

Finally, my personal thanks to dear parents and my little darling Ji-Hye Lim, for their wait, understanding, and absolute love.

# Curriculum Vitae

<b>Name</b>	Yun-II Choi
<b>Date of Birth</b>	Nov. 25, 1982
<b>Place of Birth</b>	Mokpo, Korea
<b>Permanent Domicile</b>	Mokpo, Korea

---

## Education

---

Apr. 2011 – Mar. 2014	Ph.D., Materials Science & Engineering, Nagoya University
Sep. 2008 – Oct. 2010	M.S., Materials Science & Engineering, Chonnam National University
Mar. 2001 – Feb. 2008	B.S., B.Ed., Metal Engineering Education, Chungnam National University
Mar. 1998 – Feb. 2001	Mokpo High School

---

## Membership

---

Member of the Electrochemical Society

Member of the International Society of Electrochemistry

---

## Publications

---

### *Related papers*

1. **Y.I. Choi**, S. Salman, K. Kuroda, M. Okido, "Temperature Dependent Degradation Phenomenon of Calcium-Containing Magnesium Alloys in NaCl", *will be submitted to Corros. Sci.* (2014).
2. **Y.I. Choi**, S. Salman, K. Kuroda, M. Okido, "Temperature Dependence of Passivity Breakdown on Mg-Al Alloys in NaCl Solution ", *will be submitted to Corros. Sci.* (2014).
3. **Y.I. Choi**, S. Salman, K. Kuroda, M. Okido, "Enhanced Corrosion Resistance of AZ31 Magnesium Alloy by Pulse Anodization", *J. Electrochem. Soc.* 160(8) (2013) C364–C368.
4. **Y.I. Choi**, S. Salman, K. Kuroda, M. Okido, "Synergistic Corrosion Protection for AZ31 Mg alloy by Anodizing and Stannate Post-sealing Treatments", *Electrochim. Acta* 97 (2013) 313-319.
5. **Y.I. Choi**, S. Salman, K. Kuroda, M. Okido, "Improvement in Corrosion Characteristics of AZ31 Mg Alloy by Square Pulse Anodizing between Transpassive and Active Regions", *Corros. Sci.* 63 (2012) 5-11.

### *Other papers*

1. **Y.I. Choi**, T. Eguchi, S. Salman, K. Kuroda, M. Okido, "Formation mechanism of black Cr-Co electrodeposits from Cr<sup>3+</sup> solution containing oxalic acid", *will be submitted to Cryst. Growth Des.* (2014).
2. **Y.I. Choi**, D.J. Paik, M. Okido, K. Kuroda, C.J. Park, "Improvement in Coating Quality and Corrosion Characteristics of Galvanized Steels by Pre-electrodeposition of Cu", *J. Electrochem. Soc.* 159(11) (2012) C441-C446.

3. **Y.I. Choi**, D.J. Paik, C.J. Park, "Micro-electrochemical Investigation on a Single Coating Defect of Galvanized Steel with the Capillary-based Droplet Cell", *Electrochem. Solid-State Lett.* 1(2) (2012) C5-C7.
4. **Y.I. Choi**, E.S. Shin, K. Kuroda, M. Okido, C.J. Park, "Improved surface morphology and corrosion resistance for galvanized coatings by pre-electroplating iron", *Corros. Sci.* 58 (2012) 152-158.
5. **Y.I. Choi**, R.S. Kalubarme, H.J. Jang, C.J. Park, "Effects of alloying elements on the electrochemical characteristics of an Al alloy electrode for Al-air batteries in 4M NaOH solution", *Kor. J. Met. Mater.* 49(11) (2011) 839-844.
6. **Y.I. Choi**, W.J. Beom, C.J. Park, D.J. Paik, M.H. Hong, "Surface Oxidation of the High-Strength Steels Electrodeposited with Cu or Fe and the Resultant Defect Formation in Their Coating during the Following Galvanizing and Galvannealing Processes", *Metall. Mater. Trans. A*, 41 (13) (2010) 3380-3385.
7. D.R. Kim, K.W. Cho, **Y.I. Choi**, C.J. Pak, "Fabrication of porous Co-Ni-P catalysts by electrodeposition and their catalytic characteristics for the generation of hydrogen from an alkaline NaBH<sub>4</sub> solution", *Int. J. Hydrogen Energ.* 34 (2009) 2622-2630.